

Recrystallization Behavior of Oxide Dispersion
Strengthened Ferritic Steels

HA YOOSUNG

Recrystallization Behavior of Oxide Dispersion Strengthened Ferritic Steels

- Contents -

Chapter 1. Introduction	1
1.1. Backgrounds	2
1.2. Advanced nuclear energy systems	3
1.2.1. Generation IV fission reactor systems	3
1.2.2. Fusion reactor systems	6
1.3. Structural materials for advanced nuclear energy systems	8
1.3.1. Conventional structural steels	8
1.3.2. Oxide dispersion strengthened (ODS) ferritic steels	10
1.3.2.1. ODS steel fabrication of history	10
1.3.2.2. Application for nuclear power systems	11
1.3.2.3. Strengthening mechanisms of ODS steel	16
1.4. Recrystallization processing of ODS steels	18
1.4.1. Anisotropy of mechanical properties in ODS steels	18
1.4.2. Recrystallization processing issues in ODS steels	21
1.5. Radiation effects	25
1.5.1. Radiation damage structures	25
1.5.2. Radiation effects on materials	27
1.5.3. Radiation effects on ODS steels	28
1.6. Objectives of this research	29
References	
Chapter 2. Microstructure and Mechanical Property of Annealing Processed ODS Ferritic Steels	37
2.1. Introduction	38
2.2. Experimental procedure	39
2.2.1. Materials	39
2.2.1.1. ODS steels	39

2.2.1.2. SUS 430 steels	39
2.2.2. Recrystallization treatment	42
2.2.3. Microstructure observation	43
2.2.4. Measurement of mechanical properties	44
2.2.4.1. Micro Vickers Hardness test	44
2.2.4.2. Miniaturized tensile test	44
2.3. Results and discussions	46
2.3.1. Annealing behavior of SUS 430	46
2.3.1.1. Microstructure change	46
2.3.1.2. Hardness change	49
2.3.2. Annealing behavior of ODS ferritic steels	50
2.3.2.1. Microstructure change	50
2.3.2.2. Mechanical property change	53
2.3.2.3. Specimen size effect in tensile properties	62
2.3.3. Distribution morphologies of dispersed oxide particles	65
2.4. Summary	67
References	
Chapter 3. Effect of Cold Rolling on Recrystallization Behavior	71
3.1. Introduction	72
3.2. Experimental Procedure	73
3.2.1. Hot isostatic processing	73
3.2.2. Cold rolling processing	74
3.2.3. Micro Vickers hardness test.....	74
3.2.4. Microstructure observation	75
3.3. Results and discussions	76
3.3.1. Annealing effect on HIPed 15Cr ODS ferritic steel	76
3.3.1.1. Hardness change by annealing	76
3.3.1.2. Microstructure change by annealing	77
3.3.2. Annealing effect on extruded 15Cr ODS ferritic steel	80
3.3.2.1. The hardness change by annealing	80
3.3.2.2. Grain morphology change by annealing	81
3.3.2.3. Distribution change of dispersed oxide particles by annealing	85

3.3.3. Effect of cold rolling direction on grain morphology	86
3.3.4. Grain morphology on cyclic cold rolling processing in ODS steels	90
3.3.4.1. The hardness change with cyclic pass cold rolling processing	90
3.3.4.2. Grain morphology change by annealing processing	91
3.4. Summary	94
References	
Chapter 4. Factors Controlling Hardness of ODS Ferritic Steel Before and After	
Recrystallization	97
4.1. Introduction	98
4.2. Experimental Procedure	98
4.3. Results and discussions.....	99
4.3.1. Grain size effect on mechanical properties	99
4.3.1.1. Grain boundary strengthening mechanism	99
4.3.1.2. Anisotropy in the grain shape before and after annealing	99
4.3.1.3. Hall-Petch relationship in ODS steels	99
4.3.2. Dispersion strengthening	104
4.3.3. Work hardening	107
4.3.4. Factors controlling strengthening in ODS steels	110
4.4. Summary	115
References	
Chapter 5. Ion-irradiation Effects on ODS Ferritic Steels	119
5.1. Introduction	120
5.2. Experimental procedure	121
5.2.1. The preparation of irradiated material	121
5.2.2. Ion irradiation experimental method	122
5.2.2.1. Ion-irradiation accelerator	122
5.2.2.2. Ion irradiation area	124
5.2.3. Hardness measurement by Nano-indentation	125
5.2.3.1. Nano-indentation hardness	125
5.2.3.2. Nix-Gao Model analysis of hardness by nano-indenter	127
5.2.4. Microstructure observation	129

5.3. Results and discussions	130
5.3.1. Irradiation effect at 300 °C to 10 dpa	130
5.3.1.1. Al-added ODS steel	130
5.3.1.2. Al-free ODS steel	133
5.3.2. Irradiation effect at 470 °C to 30 dpa	136
5.3.2.1. Al-added ODS steel	136
5.3.2.2. Effect of recrystallization on irradiation hardening	141
5.4. Summary	143
References	
Chapter 6. Summary and Conclusions	147
List of Publications	152
List of Presentations	153
Acknowledgement.....	154

Chapter 1

Introduction

1.1 Backgrounds

In the IEO (International Energy Outlook) 2013 reports [1], world-wide energy consumption will continue to increase by 2 % per year. The world-wide energy consumption is predicted to be twice as high in the year 2040 compared to today as shown Fig. 1-1 (a). However, the world-wide energy currently depends on consumable fossil fuels about 80 % of total energy.

With respect to global warming and energy depletion, each country has to make efforts to reduce the consumption of fossil fuels [2]. The dramatic increase in world-wide demand for energy and its environmental problems are expected in nowadays and the future society will stimulate international cooperation to consider how to meet future energy demands while reserving and improving the environment.

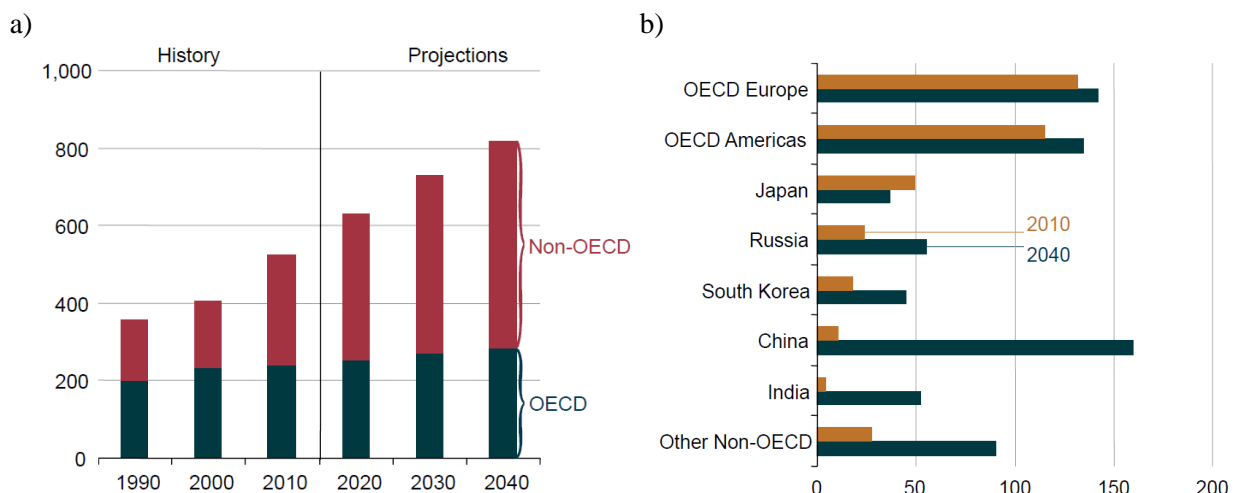


Figure 1-1 (a) World energy consumption, in 1999-2040 and (b) world operating nuclear power generation capacity [1]

This has led to nuclear energy for these decades, because large amounts of energy can be produced with nuclear reactors without the anti-environmental effects accompanied by the use of fossil fuel products (Fig. 1-1 (b)). Although renewable energy sources (solar photovoltaic, biomass, wind power etc.) may offer similar beneficial effects, concerns exist on economic efficiency and reliability when they are used for base-load power generation. The technology and economic reliability of nuclear energy have been demonstrated by the practical reactor operation throughout the world today.

1.2 Advanced nuclear energy systems

1.2.1 Generation IV fission reactor systems [3, 4]

Since the first artificial nuclear reactor, Chicago Pile-1, was constructed at the University of Chicago in 1942, many types of nuclear reactors have been developed and operated. The principal components of a nuclear reactor are the nuclear fuel, the moderator, the control rods and the control rods and the coolant. There are many possible nuclear reactor sizes and configurations, with different fuel compositions, moderators, coolants and control mechanisms, all capable of allowing a nuclear chain reaction to be sustained and controlled. In classified by generation, they could be classified into Generation I, Generation II, Generation III and Generation IV as shown Fig. 1-2 [5].

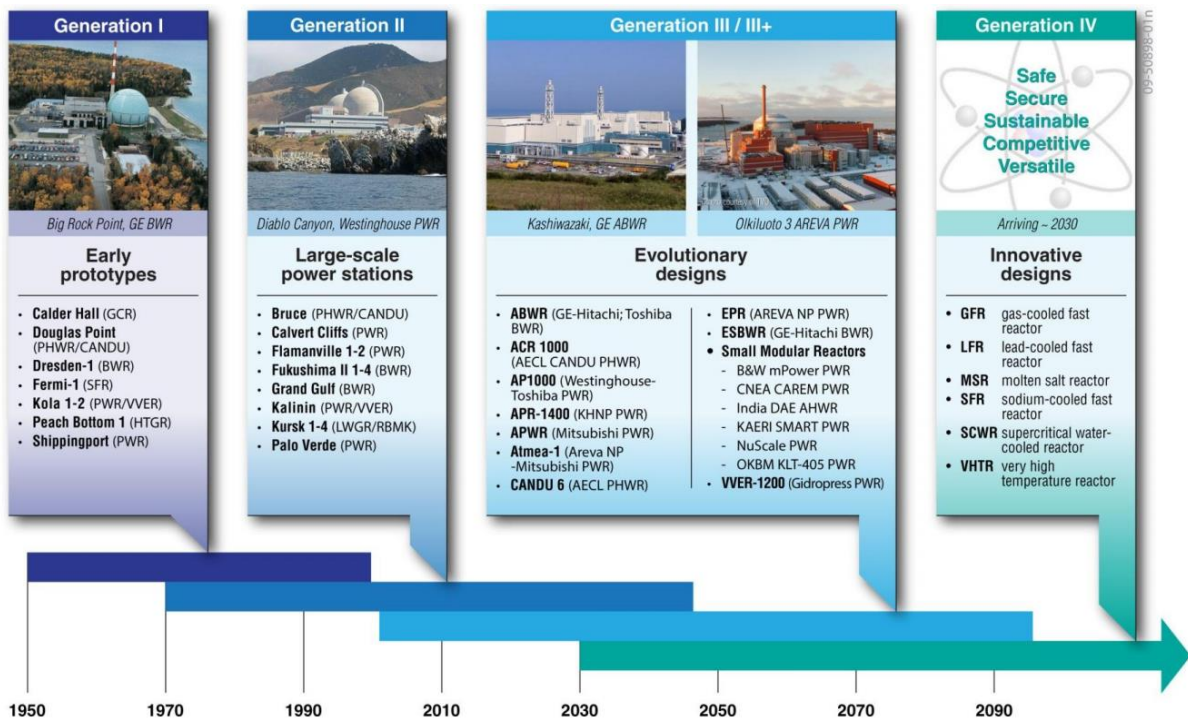


Figure 1-2 Generation system of nuclear energy [5]

Current reactors in operation around the world are generally considered to be Generation II or III systems, while the Generation I systems retired some years ago. The most feasible nuclear reactor in the world is the light water reactor (LWR) included in Generation II and III, which uses the water as its coolant and neutron moderator. The most common LWR is pressurized water reactor and boiling water reactor and it can be operated for a period more than 30 years. However, it is necessary for the nuclear reactors to increase operation temperature higher than 350 °C, towards high thermal efficiency.

For the greater improvement and innovative advances in nuclear technologies beyond Generation III systems, the research on some advanced reactor types was officially started by the Generation IV International Forum (GIF) with nine countries; Argentina, Brazil, Canada, France, Japan, Korea, South Africa, United Kingdom and United States. Finally, Switzerland, Euratom, China and Russia have joined. The primary goals for GIF are; 1. Generate energy sustainably and promote long-term availability of nuclear fuel, 2. Minimize nuclear waste and reduce the long term stewardship burden, 3. Excel in safety and reliability, 4. Have a very low degree of reactor core damage, 5. Eliminate the need for offsite emergency response, 6. Have a life cycle cost advantage over other energy sources, 7. Have a level of financial risk comparable to other energy projects, 8. Be a very unattractive route for diversion or theft of weapons. Many reactor types were considered initially, however, the most promising nuclear systems were selected; Gas Cooled Fast Reactor (GFR), Lead Cooled Fast Reactor (LFR), Molten Salt Reactor (MSR), Sodium Cooled Fast Reactor (SFR), Supercritical Water Reactor (SCWR), Very High Temperature Reactor (VHTR).

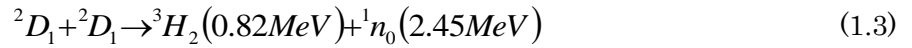
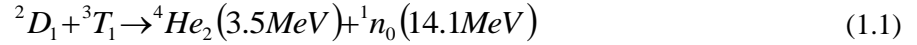
For the service conditions in Generation IV (Gen-IV) systems, the proposed structural materials must meet design objectives in the areas of (i) dimensional stability including void swelling, thermal creep, irradiation creep, stress relaxation and growth, (ii) strength, ductility and toughness, (iii) resistance to fatigue cracking and helium embrittlement, (iv) neutronic properties for core internals, (v) physical and chemical compatibility with the coolant, (vi) thermal properties during anticipated and off-normal operations, and (vii) interactions with other materials in the systems. The structural materials that are being considered for use in Gen-IV systems are listed in Table 1-1 [6].

Table 1-1 Summary of materials considered for the different GEN-IV systems [6]

Example concept	GFR	LFR	MSR	SFR	SCWR	VHTR
Spectrum	Fast	Fast	Thermal	Fast	Thermal	Thermal
Cladding	Ceramics	F/M steels, Ceramics or refractory alloys	Not applicable	F/M steel, ODSS	FM, Incoloy800, Inconel690, 625&718	ZrC coating
Core structures	SiC _f /SiC	F/M steels, ODSS	Hastelloy	F/M steels F/M ODSS	Ni alloys & F/M steels ODSS	C/C SiC _f /SiC
Reactor power(MW)	600	-	1000	-	1700	600
Net plant efficiency (%)	48	-	44-50	-	44	>50
Coolant	He	Lead alloy	Molten salt	Liquid Na	Water	He
Coolant T _{inlet} (°C)	490	-	565	-	280	640
Coolant T _{outlet} (°C)	850	550-800	700-800	520	510	1000

1.2.2 Fusion reactor systems

Fusion power is the energy generated by nuclear fusion processes. In fusion reactions, two light atomic nuclei collide and fuse to form a heavier nucleus such as process in sun and all other stars. Among the fusion reactions (1.1-3 and so on), the (1.1) reaction has been considered to be most adequate for near-future realization of fusion energy. This fusion reaction occurs between the nuclei of the two heavy isotopes of hydrogen – deuterium (D) and tritium (T) – to form a helium nucleus and the release of a neutron and high energy;



Because the reaction heating is very high temperatures (100 million degrees Celsius), the magnetic storage configuration is needed to control the thermo-nuclear plasma sustained by this reaction. Although many fusion reactor concepts have been developed, the most typical one will probably be Tokamak type [7]. For its advance and development, international cooperation was established to organize the international thermo-nuclear reactor (ITER) taken by China, the European Union, India, Japan, Korea, Russia and the United States.

ITER project was focused on plasma science and technology and the mission did not include a complete set up of blankets for energy generation. A part of blankets will be assembled as a test blanket module (TBM). In broad approach program, welding and joining technologies were acknowledged as a prime technology of fabrication of TBM. In future reactors, two components are particularly important; the tritium-breeding blankets (TBB) and divertor. The TBB takes a role in extraction the fusion energy. And it has to produce tritium for a self-sufficient operation. The divertor purifies the plasma by locally creating a magnetic configuration to evacuate the α -particles and impurities and also extracts fusion energy. A summary of structural materials for fusion blanket and divertor is given in Table 1-2 [8].

Advanced nuclear systems, such as fast breeder reactor and fusion reactor, have been developed to increase the thermal efficiency. For the development of advanced nuclear systems,

an essential issue is the performance of the structural materials. Key technologies for the structural materials include high temperature strength and long life time with the resistance under high corrosive and neutron dose environment. Many advanced materials with high performances, such as reduced activation ferritic/martensitic (RAFM) steel, vanadium alloy, SiC_f/SiC composite, have been researched and developed as structural materials, blanket for fusion. Structural materials, RAFM steels are considered to the final candidate of the international thermo-nuclear reactor (ITER) that blanket module and materials R&D to evaluate the performance under irradiation have been conducted as an international collaboration research of the broader approach (BA). In this activity, it was shown that the most critical issue for RAFM steel fabrication of ITER-TBM is welding and joining technology because the total fusion lines of welding is estimated to the 500m per a body of fusion blanket of DEMO reactor.

Table 1-2 Main candidate materials for plasma facing and breeding blanket components [8]

Function	First wall	Breeding blanket	Divertor
Plasma facing material	W-base alloy, W-coated ODS steel, flowing liquid metal: Li	-	W-base alloy, W-coated SiC _f /SiC flowing liquid metal: Li, Ga, Sn, Sn-Li
Neutron multiplier material	-	Be, Be ₁₂ Ti, Be ₁₂ V, Pb	-
Tritium breeding material	-	Li, eutectic Pb-Li, Li-base ceramic material (Li ₂ O, Li ₄ SiO ₄ , Li ₄ SiO ₄ + 2.5 wt.%SiO ₂ , Li ₂ TiO ₃ , Li ₂ ZrO ₃ , LiAlO ₂)	-
Structural material	RAFM steel, ODS steel, Vanadium alloy, SiC _f /SiC	RAFM steel, ODS steel, Vanadium alloy, SiC _f /SiC	ODS steel, W-base alloy
Coolant	-	Water, helium, eutectic Pb-Li, Li	Water, helium

1.3 Structural materials for advanced nuclear energy systems

1.3.1 Conventional structural steels [3]

The main requirement for the materials to be used in advanced reactor systems are the following: 1) high resistance to irradiation embrittlement and swelling, 2) corrosion resistance in the relevant environment and 3) high strength at elevated temperatures and so on. Fig. 1-3 shows the operation temperature in each reactor.

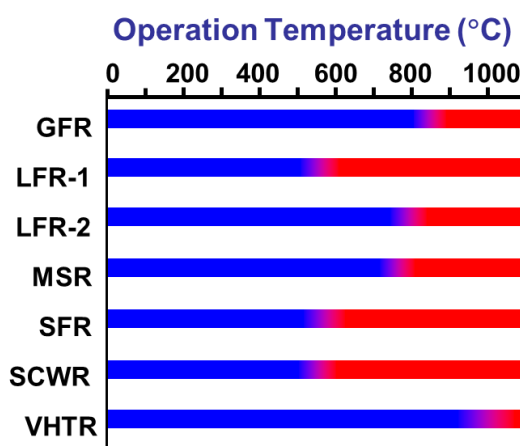


Figure 1-3 The required operation temperature in each next generation reactor

At first, austenitic stainless steels were considered as the first structural material for applications to both fast reactor and fusion reactor, also important candidates for the SCWR fuel assemblies and core internals, and there is some overlap with the ITER operating temperature regime for 316LN at 280-300 °C. In this regime, austenitic stainless steels experienced strong irradiation hardening with a reduction in uniform strain and in fracture toughness. Irradiation-assisted stress corrosion cracking is of significant concern at temperatures below 350 °C. For operating temperature above 350 °C in the SCWR core internals, other radiation effects such as void swelling, grain boundary segregation and helium generation on ductility and rupture life become critical in the stainless steels. In the temperature regime, stainless steels with addition of small amount of Ti, B and P for swelling resistance and higher creep strengths are required; examples include Japanese PNC 316, the French 15-15Ti alloy, and the US HT-UPS alloy.

However, austenitic stainless steels have been considered to be not suitable to fusion systems operated at high temperatures and to high dose because of high swelling rate, high creep rate, high thermal expansion, high thermal stress caused by low thermal conductivity and high susceptibility to helium embrittlement. For the problems of austenitic stainless steels mentioned above, the high Cr ferritic/martensitic steels have been become of interest because of high swelling resistance compared to them. Since the mid-1980s, the fusion materials programs in Japan, the European Union and the United States have been developing ferritic/martensitic steels that would lessen the environmental impact of the irradiated and activated steel after service lifetime of a fusion reactor. These conventional ferritic/martensitic steels contain 9~12Cr with about 1 % Mo, 0.1~0.2 % C and combinations of small amount of V, W, Nb etc, and have strength at elevated temperatures and good thermal properties such as conductivity and expansion coefficient. Their creep strength is also adequate in the temperature range from 550 to 600 °C. However, in the consideration of low or reduced radiological activation of the material for the safety, maintenance and protection of environment during and after the service, the fusion reactor materials programs in Japan, the European Union, the United states and Russia included the development of ferritic/ martensitic steels with replacement of the radiologically undesirable elements, Mo, Nb, and Ni, by elements such as W, V, Mn, Ta, and Ti. For these efforts, some reduced activation ferritic/martensitic (RAFM) steels have been developed for use of fusion reactors as summarized in Table 1-3 [3, 9].

Table 1-3 Typical compositions (wt%) of reduced activation martensitic steels with favorable combination of properties [3, 9]

Program	Designation	C	Si	Mn	Cr	W	V	Ta	N	B
Japan	F82H	0.10	0.2	0.5	8.0	2.0	0.20	0.04	<0.01	0.003
	JLF-1	0.10	0.08	0.45	9.0	2.0	0.20	0.07	0.05	-
US	9Cr-2WVTa	0.1	0.3	0.4	9.0	2.0	0.25	0.07	-	-
CEA	EUROFER	0.1-0.12	<0.05	0.4	8.0	1.2	0.2	0.08	0.03	0.004
China	CLAM	0.12	0.06	0.35	8.9	1.44	0.2	0.15	0.008	-

Since the 1950s, zirconium alloy (or zircaloy) is prompted the selection for cladding material of fission reactors and development having low neutron absorption cross-section, high strength and good corrosion performance in hot water. They provide an adequate measure of corrosion behavior under pressurized (PWR) or boiling water reactor (BWR) conditions. However, increased burn-up level is required that are very sensitive to the input from the fuel costs. To reach higher burn-ups, the enrichment of the fuel must increase and therefore, the fuel rod power over its lifetime will increase [8]. This situation tends to increase the fuel clad temperature that for PWRs will increase the corrosion rate (since the corrosion rate is much less dependent on temperature in BWRs, similar effect will not be seen in BWRs). Zircaloy is limited at irradiation growth and creep properties in required burn-up levels next generation systems. Also, nickel based super alloys are weak corrosion resistance of intense environment. It should be considered to development of the new materials, which can be accommodated in intense environment with corrosion resistance and irradiation properties in high temperature operating condition for both fission and fusion reactors.

1.3.2 Oxide dispersion strengthened (ODS) ferritic steels

1.3.2.1. ODS steel fabrication of history [3, 4]

Oxide dispersion strengthened (ODS) alloys have been developed for fission and fusion nuclear power systems to apply for high operation temperatures.

In 1916, the tungsten filament dispersed with thorium oxide (ThO_2) was produced in Germany. In 1946, sintered aluminum powders were developed to increase heat resistance of Al alloy. And ODS-Ni alloy with ThO_2 (TD-Ni) was developed for application to turbine in 1962. J. Benjamin et al. of International Nickel Company (INCO) firstly developed mechanical alloying (MA) process in mid-1960, that fabrication of ODS alloy started. This technique was the result of a long search to produce a nickel-based super alloy for gas turbine applications, that was expected to combine the high temperature strength of oxide dispersion and intermediate temperature strength of γ' -precipitates [3, 10]. The MA process starts with mixing of the powders of the target alloy compositions and loading the powder mixture into the pot along with the grinding medium (generally steel balls) and that can produce homogeneous alloyed powder particles. This mixture

is then milled for a desired period until homogeneous distribution of elements obtained. The milled powder is consolidated into the bulk ODS alloy by hot extrusion or hot isostatic pressing.

The technique has been developed to produce a variety of materials, which consists of a high temperature metal matrix, such as iron aluminide, iron chromium, iron-chromium-aluminum, nickel chromium or nickel aluminide, with small (5~50 nm) oxide particles of alumina (Al_2O_3) or yttria (Y_2O_3) dispersed within matrix [4]. Since the obstacles like compounds are distributed in the fine grains, the matrix of the alloys can be significantly improved in the strength and hardness, which may be accompanied by a slight loss of plasticity and toughness. And there have been many works on optimal composition based on physical metallurgy, thermal stability, coolant compatibility, the effect of hydrogen and irradiation damage, helium embrittlement [4, 11-13]. Generally, the particles become smaller and higher in the size and number density, respectively, the performance of the ODS alloys become better.

1.3.2.2. Application for nuclear power systems [14, 15]

The higher operating temperatures are required for improved efficiency and safety in fusion and fission reactors. Partially, cladding materials development is crucial to realize to achieve higher operating temperatures, operating over 100 GWd/t of supercritical water-cooled reactors (SCWR) and lead-cooled fast reactor (LFR) with high efficiency [15]. The corrosion resistance has been certainly required for practical long term operation of the advanced fission reactors [16]. Also, the candidate cladding materials and first wall structural materials must have a high resistance to neutron irradiation embrittlement and void swelling as well as a good performance of mechanical properties. Consequently, the development of ODS steels possessing higher strengths at elevated temperature for fuel cladding and other applications has been pursued in Japan, Europe, the United States and Russia.

Ukai et al. developed 9Cr-ODS martensitic steel as a cladding material for SFR [17, 18]. ODS ferritic/martensitic steels containing 9–12 wt.% chromium have been developed as the fuel cladding material of sodium-cooled fast reactor (SFR) because of their high creep strength at elevated temperatures and enough resistance to neutron irradiation embrittlement. Recent irradiation experiments clearly showed that the ferritic/martensitic ODS steels were rather highly resistant to neutron irradiation embrittlement at temperatures between 300 °C and 500 °C up to 15

dpa [19, 20]. They never showed irradiation induced loss of elongation that was generally observed in metallic materials. That is, the ODS steels showed irradiation hardening accompanied by no-loss-of-ductility. However, the application of ferritic/martensitic ODS steels to the cladding of SCWR and LFR is limited because of insufficient corrosion resistance of the steel. It is well known that the corrosion resistance in high temperature water is reduced significantly by decreasing chromium concentration below 12 %. Thus, for high Cr ODS ferritic steels, the most critical issue for the application to SCWR and LFR is to improve their corrosion resistance. Corrosion resistance of iron based alloys is influenced by chromium (Cr) and aluminum (Al). It is expected that an adequate combination of the contents will be available for Cr and Al in the steels for each blanket system.

An increase in the Cr content increased tensile stress as shown in Fig. 1-4 [14]. This can be explained by solid solution hardening by Cr. The tensile stress was larger than 9Cr- ODS about 100 MPa at temperatures between room temperature and 400 °C, and about 50 MPa at 800 °C. Since the potential hardening by oxide dispersion is much larger than that by solid solution of Cr, the difference in the tensile stress by increasing Cr is rather smaller than the difference in the

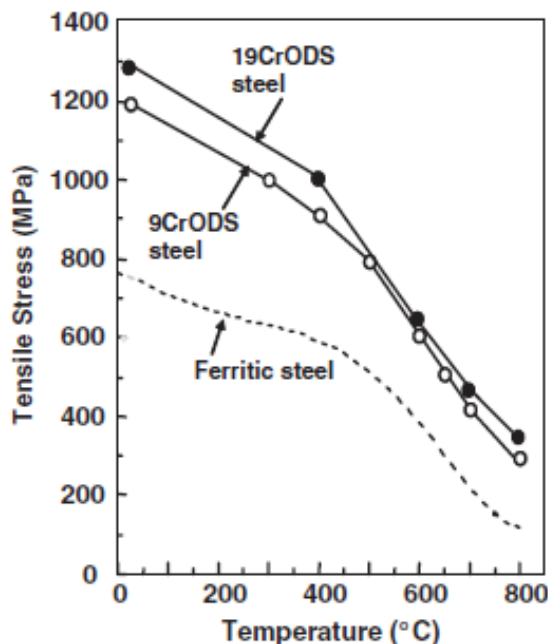


Figure 1-4 The dependence of tensile stress on test temperature in ferritic steel, 9Cr-ODS steel and 19Cr-ODS steel [14]

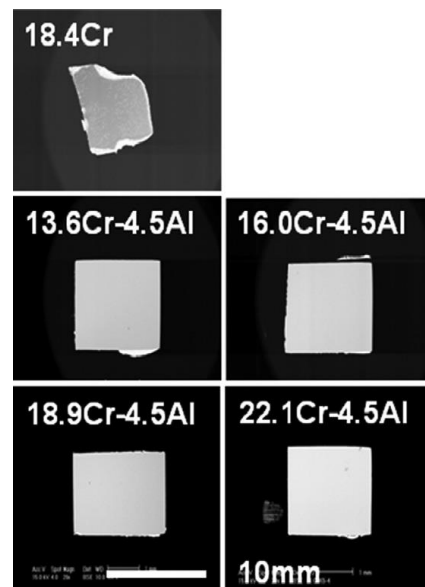


Figure 1-5 The appearance of ODS steel specimens after corrosion test in LBE [15]

tensile stress between ferritic steel and 9Cr-ODS steel in which only the difference is the existence of nano-sized (less than 4 nm in diameter) oxide particles in high density in 9Cr-ODS steel.

Corrosion test results in SCW and lead–bismuth eutectics (LBE) were referred to determine Cr and Al content. LBE has high solubility of nickel, iron and chromium, which are most important alloy elements in austenitic stainless steels, which is the reason of the difficulty to use nickel super alloys and iron-based austenitic stainless steels as the structural materials for LBE cooled systems, especially at temperatures higher than 500 °C [15]. Ferritic steels that contain only a small amount of nickel have been considered to be more adequate for LBE application. Above 600 °C, however, the solubility of iron and chromium in LBE also becomes significantly larger. In order to prevent material from dissolving into LBE, alumina coating was often conceived. Without alumina coating, however, it is also considered that alumina film, which is spontaneously formed on the surface of the steel containing Al in solution, may suppress dissolution. Fig. 1-5 [15] shows the appearance of ODS steel specimens after corrosion test in LBE with 10^{-6} wt. % O₂ in solution for 10k h at 650 °C. The Al free 19 wt. % Cr ODS steel dissolved into LBE markedly, while those of ODS specimens containing 4 wt. % Al almost completely kept the specimen shape, indicating much higher resistance to LBE corrosion. It is worth to noting that the corrosion resistance in LBE is independent of Cr concentration from 13 to 19 wt. % in Al-added ODS steels. The addition of Al is considered to be inevitable for structural materials to apply to LBE nuclear systems especially above 500 °C. It should be noted that the weight gain is much larger in SUS430 (16 Cr) than in 16Cr ODS steel as shown Fig. 1-6 [15]. This clearly indicates that the oxide particles dispersion plays an effective role in the high corrosion resistance of ODS steels, since the corrosion resistance in water environment is mainly controlled by Cr concentration.

The corrosion resistance of ODS steels increases with chromium concentration. The effect of Al on corrosion resistance depends on Cr concentration. The Cr content can be balanced between a merit of corrosion resistance and a demerit of aging embrittlement with maintaining strength at elevated temperatures. In 19-Cr ODS steel, the addition of 4 wt.% Al did not remarkably influence the corrosion resistance. However, in 16Cr-ODS steel, the addition of Al improved corrosion resistance. The suppression of corrosion by Al addition in 16Cr-ODS steel is

due to formation of very thin alumina film on the surface. In 19Cr-ODS steel, rather dense chromia film was observed on the specimen surface [21]. It is considered that 16 wt.% Cr is not large enough to form homogeneous and stable chromia on the whole specimen surface, while very thin alumina film covers the whole specimen surface of the ODS steel added with 4 wt.% Al. Thus, an addition of Al is effective to improve corrosion resistance of 16Cr-ODS steel but not in 19Cr-ODS steel.

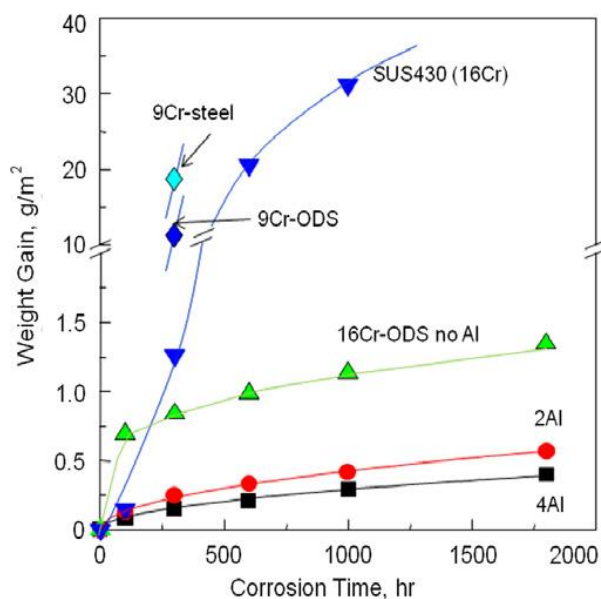


Figure 1-6 The weight gain after corrosion tests in SCPW (510 °C, 25 MPa) up to 1800 h [15]

For the application of the ODS steels to nuclear power plant as a structural material, the phase stability of the oxide particles under irradiation is essential. In our previous research [14], the ion irradiation experiments were performed at temperatures 300, 500 and 700 °C up to 20 dpa (56 h) for the 19Cr-4.5Al ODS steel as a reference of high-Cr ODS steels. Microstructure observations revealed that a number of small dislocation loops were observed after the irradiation at 300 °C, although no significant change was observed for the other structures such as voids and precipitates. Furthermore, at 500 °C, any significant effects such as formation of dislocation loops and voids, and precipitation of secondary phases were not observed. Fine precipitates in grains did not grow up significantly during ion irradiation. At 700 °C, however, the irradiation caused a change in the precipitation behavior, showing that carbides precipitated both in grains and along grain boundaries. The size of larger precipitates reached to several hundreds nm, and the

precipitation occurred in both the irradiated and un-irradiated region. The TEM-EDX analysis of matrix, grain boundaries and precipitates in grains were performed. The normalized atomic ratio of chromium on grain boundaries was higher than the others, the carbides were considered to be chromium-rich phase. In contrast, the normalized atomic ratio of aluminum was almost uniform in the matrix and along grain boundaries. It is expected that the segregation of aluminum at grain boundaries would not occur under the irradiation at 700 °C. Irradiation hardening was measured for the specimens irradiated at 300 and 500 °C up to 10 dpa. The normalized irradiation hardening of H_{ir}/H_{unir} was measured using nano-indenter, and the results are shown in Fig. 1-7 [14]. H_{ir} and H_{unir} was the hardness of 19Cr-4.5Al ODS steel before and after ion irradiation, respectively. The irradiation hardening increased with increasing the irradiation dose at 300 °C. On the other hand, no hardening was observed at 500 °C for 19Cr-ODS steel. This trend is similar to the 9 Cr ferritic steels. It was reported that high-Cr ODS steels often suffer irradiation embrittlement caused by the phase decomposition of Fe/Cr. In the previous work, the Cr-rich α' phases were observed in the 12 Cr ferritic steel after the neutron irradiation at 380 °C to 15 dpa (about one year) being accompanied by a large irradiation hardening. The ion irradiation hardening at 573K is considered to be due to the dislocation loops but not the Cr-rich α' phases, since no such a phase was observed after the irradiation. It should be noticed that even at 300 °C the Cr-rich α' phases were not formed up to 10 dpa in 19Cr-4.5Al ODS steel.

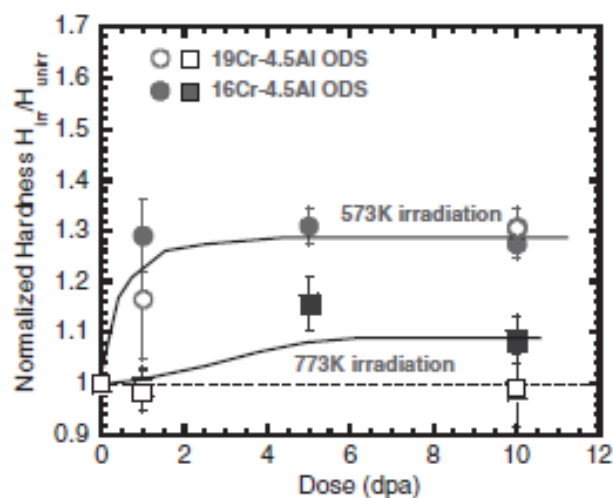


Figure 1-7 The dependence of the irradiation hardening on the ion dose in the 16, 19Cr-4.5Al-ODS steel irradiated at 300 and 500 °C [14]

From a viewpoint of reduced activation, Al is not an adequate element for application to fusion blanket. The advantage of Al addition is significant in corrosion resistance as mentioned above. The corrosion rate of Al-free 16Cr-ODS steel in SCPW at 600 °C is about 3.5 times higher than that of Al-added 16Cr-ODS steel. Although the effect of flow rate of SCPW on the corrosion rate is necessary to assess the feasibility for fusion application, it can be concluded that the Al addition is not inevitable for 16Cr-ODS steel for the application to SCPW cooled blanket system for DEMO or beyond. As for the corrosion resistance in LBE, it is considerably improved by Al addition that causes the formation of thin alumina on the specimen surface. In the case of Al free ODS steels, the dissolution of Fe and Cr increases considerably at elevated temperatures higher than 500 °C, which may limit the operation window of the LBE cooled system.

Based on the surveillance test for the high-Cr ODS steels so far, it is considered that the ODS steels are most promising as high burn-up fuel cladding material. They have rather high-resistance to neutron irradiation at temperatures between 300 and 500 °C up to 15 dpa, and the investigation of irradiation effects beyond the above conditions is now under way. A high-tensile stress was achieved for the 9 to 19 Cr- ODS steel, which was ranging from 300 to 350MPa at 800 °C. The most promising materials performance of the ODS steels is considered to be due to dispersion of very fine yttria oxides of which the diameter is ranging from 1 to 5 nm.

1.3.2.3. Strengthening mechanisms of ODS steel

Strengthening ODS steels is achieved by dispersion particles which play a role as barriers to dislocation moving during the deformation. In most binary systems, alloying above a concentration given by the phase diagram will cause the formation of a second phase. A second phase can also be created by mechanical or thermal treatments. The particles that compose the second phase precipitates act as pinning points in a similar manner to solutes, though the particles are not necessarily single atoms. This is a schematic illustrating how the dislocations can interact with a particle.

According to the Orowan by-passing mechanism [3, 22], hard incoherent dispersoids such as Y_2O_3 are bypassed through the formation of Orowan loops at low temperatures (as shown Fig. 1-8). The bypassing stress, that is Orowan stress, is given by,

$$\sigma_{OR} = 3.06 \times \frac{0.8\mu b}{L} \quad (1.4)$$

where, $M = 3.06$ is the Taylor factor, μ is elastic modulus of matrix, b is the magnitude of the Burgers vector and L is the inter-particle spacing distance, respectively. L can be expressed approximately by square-shaped array area as,

$$L = (Nd)^{-1/2} \quad (1.5)$$

Generally, the following requirements have been imposed for dispersion strengthened particles: particle size should be as small as possible (less than 10 nm), particle spacing to achieve enough performance is in the range of several tens nm. In addition, the particles should be stable under high temperatures keeping the size be small by suppressing mutual agglomeration of the small particles. Phase stability of oxide particles is a critical for nuclear structural materials, because under irradiation, non-equilibrium condition is often generated to accelerate phase change [4].

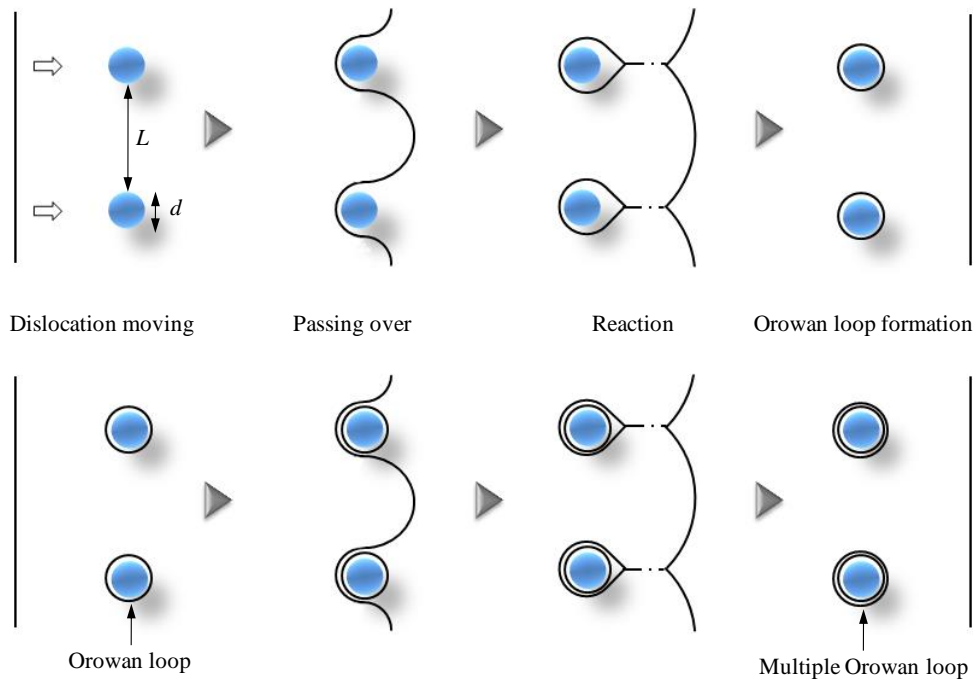


Figure 1-8 The schematic diagram of the Orowan mechanism [3]

1.4 Recrystallization processing of ODS steels

1.4.1 Anisotropy of mechanical properties in ODS steels

In fabrication processing, the mixed MA powders are milled for desired period until homogeneous distribution of elements obtained. Then, the milled powders are consolidated into the bulk ODS steel by hot extrusion or hot isostatic processing. In case of hot extrusion processing, the high pressure and elevated temperature are required for dense material with homogeneous dispersion of oxide particles. After extrusion processing, the elongated grains are formed along with extrusion direction and the orientation texture is following typical extrusion processing steps. Elongated grains often cause the anisotropy in mechanical properties such as tensile strength, creep properties, ductile-brittle transition temperature (DBTT) and fracture toughness. The grain morphologies are also major factors giving influences on the strength depending on the direction of applied force. Therefore, grain structure is very important and must be optimized for good materials performance [11, 23].

P. Olier et al. [24] observed the elongated grains with using TEM of the extruded bars in longitudinal (parallel to the extrusion direction) and transverse (perpendicular to the direction of extrusion) directions. The microstructure consists of fine grains elongated along the extrusion direction, the grain size determined by image analysis is slightly above 500 nm widthwise and around 1200 nm lengthwise which means an average shape anisotropy factor of 2.5. In the transverse direction, grains are fine and equiaxed being about 600 nm of mean diameter.

Fig. 1-9 shows the tensile stress-strain behavior of high Cr ODS ferritic steels, which have anisotropic behavior. The fracture strain in L-R orientation can be longer than the others because the ODS steels have elongated grains in parallel to the loading direction, which is induced by MA and hot extrusion process in parallel to the loading direction [25]. M. Serrano et al. [26] also reported that the anisotropy of an extruded 14Cr ODS steel bar, which includes the microstructural characterization and tensile tests of specimens obtained in the longitudinal and transverse orientations. The elongated grains along the extrusion direction and small areas with equiaxed grains were observed in the longitudinal direction. Nevertheless, the grains were more equiaxed and with a smaller mean size in the transverse orientation. The observed microstructural

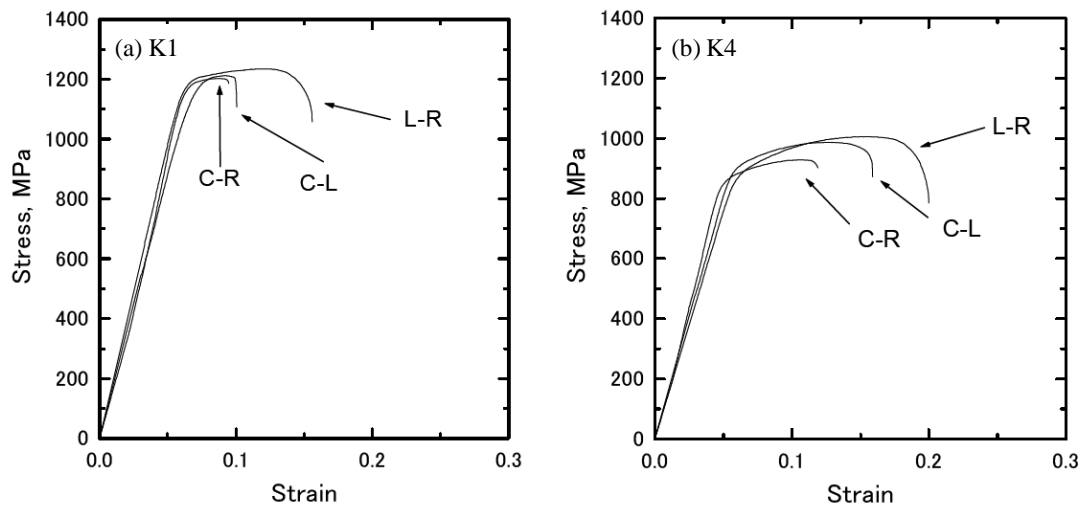


Figure 1-9 Typical stress-strain curves obtained from the longitudinal axis with radial direction plane (L-R), circumferential axis with longitudinal plane (C-L) and circumferential axis with radial direction (C-R) specimens of (a) the K1 and (b) K4 ODS steels [25]

anisotropy seems to exhibit a direct effect on the ductility of the ODS material studied. It was found that the transverse orientation was around 50 % less ductile than the extruded direction, while yield stress and ultimate tensile strength were almost unaffected by anisotropy. The differences in the grain morphology of each orientation also appear to affect the fracture mode. The fracture surface of transverse specimens presented an elongated structure, while in the longitudinal specimens a more uniform an equiaxed grains with dimple formation were observed. In the creep properties [27] the alloy exhibits strong anisotropy in creep resistance at 725 °C. The material has substantially lower creep performance in the direction normal to the extrusion axis. The anisotropy was found to become more prominent with increasing rupture times.

Anisotropic behavior was observed for the small punch ductile–brittle transition temperature [28, 29]. Size of dimple and existence of flat fracture area in ODS ferritic steels (SOC-1) observed in fracture surfaces can explain the lower tensile strain for the transverse direction than for the longitudinal direction. Charpy impact properties for the L-R direction is better than for the C-R and C-L directions.

S. K. Karak et al. studied the anisotropy for the specimens produced by a modified fabrication processing, which is hydrostatic extrusion method [30, 31]. The anisotropy is still acquired in ODS ferritic steels in spite of improving higher strength than that fabricated by high

pressure sintering, hot isostatic pressing and pulse plasma sintering.

These anisotropy is not only for ODS ferritic steels but also for austenitic and martensitic or RAFS ODS steels. It was reported that there is an effect of grain morphology on hydrogen embrittlement where significant embrittlement occurred in the transverse direction of ODS steels [11, 32]. The anisotropy affects welding properties of ODS steel. S. Noh et al. [33] reported that friction stir processing of ODS steel likely improve the anisotropy effectively. The base material exhibits an anisotropic microstructure of finely elongated grains in the extrusion direction. In contrast, friction stir processing produced uniformly equiaxed and coarsened grains in stirred zone. This can be attributed to frictional heat and plastic flow induced by rotating tool during friction stir processing. Following this results, the tensile elongation of stirred zone shows no anisotropy between longitudinal and transverse direction, although yield strength is lower than that of base material. This indicates that equiaxed grains are induced by frictional heat and plastic flow through dynamic recrystallization process so as to suppress anisotropy in the microstructure of ODS steels.

Fig. 1-10 shows a typical microstructure in the ODS steel which is as-extruded (ODSE) and recrystallized (ODSR) [34]. The microstructure of the ODSE has high dislocation density introduced during MA and uniformly distributed particles. The grains are elongated along with the hot extrusion direction. Conversely, in recrystallized ODS steel, the dislocation density is reduced and the grain size is increased. It appears that the strength anisotropy is suppressed by the recrystallization.

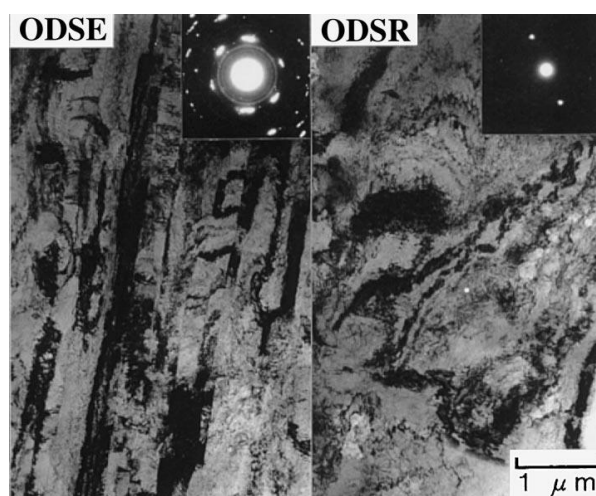


Figure 1-10 Microstructures in as-extruded ODS steel and recrystallized ODS steel [34]

1.4.2 Recrystallization processing issues in ODS steels

As mentioned earlier, the anisotropy by elongated grains formed during the fabrication processing with hot extrusion has effects on several mechanical properties of ODS steels. The strength of longitudinal direction with extrusion direction is superior, but it is significantly decreased in radial direction. Therefore, reducing the anisotropy is necessary to improve the stability and formability in the mechanical properties of ODS steels.

Recrystallization often results in the modification of grain morphology into equiaxed grains, which makes materials be formable such as result of friction stirred processing. Thus, recrystallization behavior is a key issue in the fabrication processing of ODS ferritic steel, especially cladding tube manufacturing.

Recrystallization behavior of metals is commonly understood as follows [35];

(1) Recovery: The free energy of a crystalline material is increased by deformation through the generation of dislocations, and the material containing these defects is thermo-dynamically unstable. Although thermo-dynamics would suggest that the defects should spontaneously disappear, the stable defect structures are retained after deformation in practice (Fig. 1-11 (a)). If the material is subsequently annealed to an enough high temperature, thermally activation processes such as solid state diffusion provide that the defects may be removed or arranged in a configuration of lower energy state. The annealing processing of cold rolled metal at an elevated temperature changes the microstructure and also properties of the material, which may be partially recovered to their original values by the annihilation and rearrangement of the dislocations. However, these microstructural changes during recovery are relatively homogeneous and do not usually affect the grain boundaries between the deformed grains as shown in Fig. 1-11 (b). Recovery generally involves only a partial restoration of properties because the dislocation structure is not completely removed and may reach to a metastable state.

(2) Nucleation and recrystallization: A further restoration process called recrystallization may occur in which new dislocation-free grains are formed within the deformed or recovered structure (Fig. 1-11 (c)). These then grow and consume the old grains, resulting in a new grain structure with a low dislocation density, (Fig. 1-11 (d)).

(3) Grain growth: Although recrystallization removes the dislocations, the material still contains

many grain boundaries, which are thermo-dynamically unstable. So annealing may result in grain growth, where the smaller grains are eliminated, the larger grains grow and grain boundaries tend to be a lower energy configuration (Fig. 1-11 (e)). Sometimes, the selective growth of a few large grains (Fig. 1-11 (f)), a process known as abnormal grain growth or secondary recrystallization can be shown.

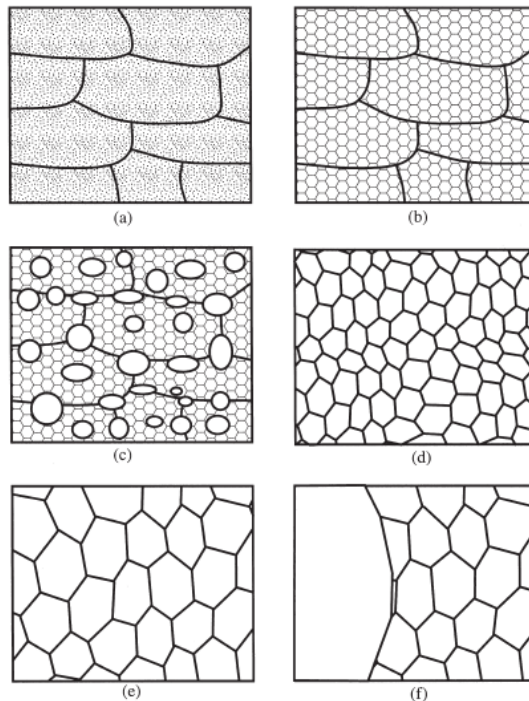


Figure 1-11 The schematic diagram of the main annealing processes [35]

Although recrystallization behavior is surely occurred under annealing processing, there is no clear standard to distinguish each above step during continuous heat processing, and the microstructures evolve gradually with no identifiable nucleation and growth stages in this case. On the other case, it can be formally described in terms of nucleation and growth stages as discontinuous processes. Thus, the ‘continuous’ phenomena include recovery by sub-grain growth, continuous recrystallization and normal grain growth and the ‘discontinuous’ phenomena include discontinuous sub-grain growth, primary recrystallization and abnormal grain growth.

In ODS steels, the ultra-fine oxide particles are strengthening in matrix, where the strengthening mechanism of ODS steels is considered to be achieved by dispersion particles which play a role as barriers to dislocation motion during the deformation, which is related to the

Orowan mechanism in previous part (Chap. 1.3). On the other hand, the dispersed particles also inhibit the migration of grain boundaries. The small grain sizes of ODS steel is due to the oxide particles, the migration force of grain boundary, which exceeded a drag force of oxide particles, can be estimated by Zener equation. The relationship of oxide particle, grain boundaries and dislocation distribution will be investigated in Chapter 4.

The recrystallization of ODS steels is often suppressed by these fine and high density oxide particles [15]. Furthermore, the strengthening and annealing mechanisms are influenced by multiple factors, which are chemical compositions, cold rolled level, heat treatment conditions as well as starting powder condition: pre-mixed or pre-alloyed [28, 37-41].

Chou et al. [42] measured the recrystallization temperature of MA956 (20Cr-4.5Al-0.5Y₂O₃) and MA957 (14Cr-1Ti-0.27Y₂O₃) by differential scanning calorimetry (DSC), and concluded that the higher recrystallization temperature of MA957 was due to a strong texture elongated into the γ -fiber or [111] direction. Sandim et al. [43] reported that the yttrium based oxide particles with the diameter of about 10 nm was effective to retard recrystallization of 9Cr-ODS Eurofer steel. Chen et al. [44] investigated the effect of cold rolling level on the annealing behavior of an ODS steel (PM2000) and showed that recrystallization was initiated at lower temperatures in the specimens with greater cold rolling direction. As for recovery behavior, Renzetti et al. [45, 46] measured the dislocation density in ODS-Eurofer steel by means of XRD based on the modified Williamson-Hall plot and reported that the dislocation density of 80 % cold rolled samples was $8.0 \times 10^{15} \text{ m}^{-2}$ and that of annealed sample at 800 °C for 1 hour was $2.0 \times 10^{15} \text{ m}^{-2}$.

Several researchers have investigated recrystallization behavior of ODS steels in terms of crystallography. Most of the literatures concerning the recrystallization of ODS alloys refer to primary recrystallization after heavy deformation, which is usually as-milled and/or as-extruded powders after hot consolidation. Further secondary recrystallization to obtain a coarse elongated grain structure is usually performed under a high temperature gradient (directional recrystallization) to promote the formation of a high grain aspect ratio [47, 48].

In our previous study on high resolution transmission electron microscopy of nano-scaled oxide particles, the coherency between the particles and matrix was examined in detail and it was shown that the coherency changed with the size and composition of the particle [12, 49].

Kasada et al. [28] investigated the oxide morphology of high Cr ODS ferritic steels in

different chemical compositions of Ti and Al. The STEM-EDX and XRD analysis indicated that mechanically-alloyed Y_2O_3 reacted with dissolved Ti and Al in the ODS steels and formed Y_xTi_yO and Y_xAl_yO . It is concluded that the fine oxide particle in K1 (Fe-19Cr-0.3Ti) ODS steel can be associated with the formation of fine Y-Ti oxide, such as $Y_2Ti_2O_7$ complex oxide which can also be observed in the experimental 9Cr-ODS steel. On the other hand, some coarsening of the oxide particle in the Al added K4 (Fe-19Cr-4Al) ODS steel was observed, and they were identified as Y-Al oxide. Researchers observed some types of complex oxide in Al-added high Cr ODS ferritic steels, such as the tetragonal $Y_3Al_5O_{12}$ (YAT), the monoclinic $Y_4Al_2O_9$ (YAM) and the garnet $Y_3Al_5O_{12}$ (YAG).

The anisotropy of mechanical properties was thought to be explained by the combined effect of bundle-like structure of elongated grains with aggregates of small-size grains and segregation/precipitation along ED [23]. It was reported that there was an anisotropic behavior in the fracture toughness of the hot-extruded MA957 ODS ferritic steels, and that the low toughness could be improved by the elimination of stringer-like alumina inclusion which was due to impurities in the source powder. The existence of elongated $M_{23}C_6$ in the two types of hot-extruded ODS ferritic steel (Fe-19Cr-4Al-2W-0.3Ti-0.3 Y_2O_3 and Fe-19Cr-0.3W-0.3Ti-0.3 Y_2O_3) suggested contamination of relatively high concentration (0.05–0.09 wt.%) of impurity carbon [50]. The coarser precipitates were identified to be mainly titanium oxides but Cr-rich precipitates of $M_{23}C_6$ type were also observed. These (Fe, Cr, W) $M_{23}C_6$ carbides were mainly observed at grain boundaries [24]. Presumably, general properties of the ODS ferritic steels depend on multiple factors including chemical compositions, fabrication process, impurity level and conditions of raw powders (pre-mixed or pre-alloyed) [28].

Strengthening mechanisms and deformation processes of ODS steels have been studied actively [37]. Schneibel et al. [51] introduced particle hardening, grain boundary hardening, and thermally activated absorption of dislocations at grain boundaries to explain the temperature dependence of strength. However, the effect of grain structures on mechanical properties through annealing processing and each role of the alloy microstructures have not been well understood.

1.5 Radiation effects

Understanding radiation effects on materials is necessary to apply the materials to in-core structural materials where atoms comprising the structural components are displaced numerous times over the course of their engineering lifetime.

1.5.1 Radiation damage structures

During irradiation, a neutron collision with an atom of the matrix may result in the displacement of the atom from their original positions and may cause property changes of the materials. Displacement cascades include several vacancy clusters and interstitial dislocation loops. Types of defects are as follows;

(1) Interstitials and vacancies: An interstitial is the atom that is not located at a regular lattice site in crystal lattice. Some impurity atoms in metals are efficient traps for self-interstitial atoms (SIAs) although the efficiency depends on impurity atoms [52]. The vacancy, or missing lattice atom, is the simplest point defect in metal lattices. Vacancies can generally be trapped at an oversized solute or impurity atoms in order to lower the overall free energy of the solid. Hence, these solutes can act as efficient traps for vacancies in the lattice. Diffusion of vacancies occurs by the jump of an atom from its lattice site to a vacant site. For an atom to move by this mechanism, a vacancy is required to exist at a neighboring lattice site. Since movement of the vacancy is opposite that of the atom, vacancy-type diffusion is regarded as either a movement of the atom or the equivalent movement of the vacancy. In case of metal, the potential energy of interstitial atoms for migration is far lower than that of vacancies. For example, in Cu, the potential energy difference between stable and unstable state is 1 eV and 0.05 eV in the case of vacancy and interstitial atom, respectively. Accordingly, the interstitial atoms migrate at around 10 K, while vacancies move at around 300 K [53]. When the same defects are combined each other, they convert into a cluster such as voids or dislocation loops. When a vacancy and an interstitial atom meet, they annihilate each other.

(2) Dislocation loops: Prismatic dislocation loops are examples of interstitial and vacancy clusters (Fig. 1-12). In BCC, the prismatic interstitial-type loops have a perfect Burger's vector.

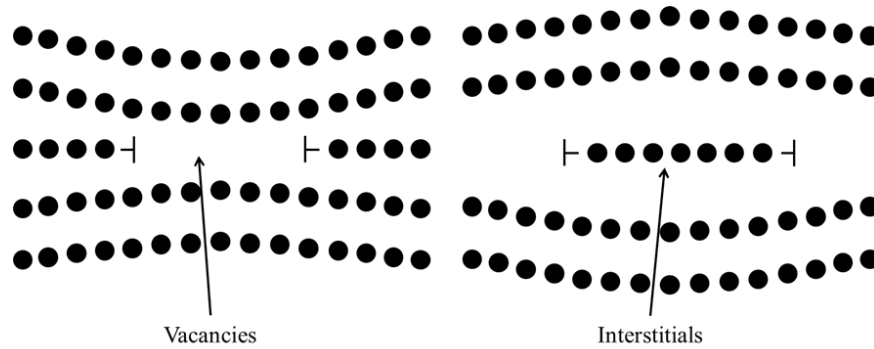


Figure 1-12 Vacancies and interstitial-type dislocation loops

Two types of vacancy clusters are possible; vacancy-type dislocation loop as well as void configurations [52]. The types of vacancy clusters formed during irradiation depend on the relative formation energies and the kinetics of vacancy cluster evolutions. Commonly, the vacancy more tends to form the void (sphere defects) than forming dislocation loops. The size and the number density of dislocations loops depend on irradiation temperature and material.

(3) Voids: When dislocations preferentially absorb interstitial atoms, the residual vacancies increase to form vacancy clusters. At a high temperature or high irradiation dose, the vacancy cluster can be formed in matrix except in the case that materials have nature of low stacking fault energy, which may influence on void swelling of the material. The voids are polyhedral and it can be annealed out by heat treatment after irradiation. On the other hand, the helium bubbles are formed by (n, p) or (n, α) nuclear reactions at a high temperature. These bubbles are almost sphere shapes and rather stable.

(4) Precipitation: Since a number of vacancies are formed by irradiation, the diffusion of solute atom is accelerated and precipitation and/or resolution are also accelerated.

The formation of above radiation damage structures depends on irradiation conditions, such as, temperature, dose, flux and energy spectrum, which results in the changes in the radiation effects depending on the irradiation environment.

1.5.2 Radiation effects on materials

Exposure of metals to irradiation results in an increase in the yield strength over a wide temperature range, and is most pronounced at $T_{\text{irr}} < 0.3T_m$. In BCC metals tested at low temperature, the irradiation up to a high fluence may result in the disappearance of necking deformation accompanied by a brittle fracture in the elastic deformation region. Irradiation induced hardening is caused by the production of the various defects; i) microvoids, ii) impurity-defect cluster complexes, iii) dislocation loops (both vacancy and interstitial type), iv) dislocation lines (dislocation loops and dislocation network of the original microstructure), v) bubbles and vi) precipitates.

Notice that the effect of voids on irradiation hardening is imperceptible as a result of experiments that show irradiation hardening is not remarkably different before and after void annihilation by annealing treatment. It has been considered that dislocation loops are the main factor controlling irradiation hardening because of the adequate correlation between microstructural evolution and irradiation hardening. These defects cause not only irradiation hardening but also irradiation embrittlement, which lead to a limit of lifetime of material.

The experimental results on helium effect performed by ion-implantation or neutron irradiation have shown that even small concentrations in the range of some tens of appm can lead to ductility loss or dynamic fracture toughness degradation [54]. In addition, annealing experiments of irradiation induced He-bubbles beyond the α - γ transition temperature lead to bubble migration and coalescence with relatively large and stable He gas filled cavities as end product that certainly cause problems for any subsequent joining treatments.

The solutes segregation in the vicinity of the grain boundaries and dislocations is caused by the site exchange between solute atoms and point defects [55]. The formation of point defect clusters is the simplest interaction of point defects, whereby point defects gather and form clusters such as dislocation loops and voids. Radiation-induced precipitation and formation of point defect clusters are known to potentially cause hardening-embrittlement. The behavior of self-interstitial defects in Fe specifically attracted much interests because of their industrial importance. Self-interstitial atoms have a unique behavior in Fe when compared to the other BCC metals. This is that the $\langle 110 \rangle$ self-interstitial is more stable than the $\langle 111 \rangle$ self-interstitial. In the case of

industrial steels, Cr is essential for the corrosion resistance of the steels. Further, the interaction between point defects and Cr atoms has been investigated in many studies. A firm understanding of the effect of radiation on materials is required to design and improve more radiation-tolerant materials.

1.5.3 Radiation effects on ODS steels

For the application of the ODS steels to nuclear power plant as a structural material, the phase stability of the oxide particles under irradiation is essential. Since the dispersed fine oxide particles play a role as trapping site for radiation-induced point defects, ODS steels have extremely higher resistance than the other conventional steels. .

Kimura et. al [14] researched that a number of small dislocation loops were observed in 19Cr-4.5Al ODS steel after the ion-irradiation at 300 °C up to 20 dpa, although no significant change was observed for the other structures such as voids and precipitates. Furthermore, at 300 °C, any significant effects such as formation of dislocation loops and voids, and precipitation of secondary phases were not observed. At 700 °C, however, the irradiation caused a change in the precipitation behavior, showing that carbides precipitated both in grains and along grain boundaries. The irradiation hardening of 19Cr- 4.5Al ODS steel increased with increasing the irradiation dose at 300 °C. On the other hand, no hardening was observed at 500 °C for 19Cr- ODS steel. The ion irradiation hardening at 300 °C is considered to be due to the formation of dislocation loops but not the Cr-rich phases, since no such a phase was observed after the irradiation. It should be noticed that even at 300 °C the Cr-rich phases were not formed up to 10 dpa in 19Cr-4.5Al ODS steel.

1.6 Objectives of this research

As described above, high Cr ODS ferritic steels are a promising candidate for structural material of advanced nuclear power systems, GEN-IV fission and fusion reactors. The ODS steels have high advantages such as excellent resistance to irradiation embrittlement, high strength at elevated temperature and corrosion resistance. Recrystallization process is a critical issue for better formability in the fabrication process of cladding tube of ODS steel, which can reduce anisotropy in the mechanical properties caused by elongated grains. Mechanical properties are closely related with microstructural features like grain size and their morphology. These parameters are affected by recrystallization treatment that may simultaneously change both the grain size and oxide particle morphology [56, 57]. Detailed information concerning the change in the grain and oxide particle morphology of the ODS steels, its orientation with respect to the alloy matrix, and the individual elementary composition by recrystallization treatment and their effects in the mechanical properties are still unclear. In this research, therefore, recrystallization behavior of ODS ferritic steel is investigated to understand the effects of recrystallization on materials performance of ODS ferritic steels with focusing on the hardness and microstructural changes as well as irradiation response.

References

1. International energy outlook 2013, Energy information administration, Office of integrated analysis and forecasting, U.S. Department of energy, Washington. DC, 20585 (2013)
2. IEA, Outlook for world energy (2009)
3. S. Noh, Doctor's thesis, *Kyoto University* (2011)
4. H. Je, Doctor's thesis, *Kyoto University* (2013)
5. Generation IV international forum web site, <http://www.gen-4.org/Technology>
6. P. Yvon, F. Carré, "Structural materials challenges for advanced reactor systems", *J. Nucl. Mater.*, **385** (2009) 217-222
7. Prachai Norajitra, Leo Bühler, Ulrich Fischer, Serguei Gordeev, Siegfried Malang, Gunter Reimann, "Conceptual design of the dual-coolant blanket in the frame of the EU power plant conceptual study", *Fusion Eng. Des.*, **69** (2003) 669-673
8. N. Baluc, K. Abe, J.L. Boutard, V.M. Chernov, E. Diegele, S. Jitsukawa, A. Kimura, R.L. Klueh, A. Kohyama, R.J. Kurtz, R. Lässer, H. Matsui, A. Möslang, T. Muroga, G.R. Odette, M.Q. Tran, B. van der Schaaf, Y. Wu, J. Yu, S.J. Zinkle, "Status of R&D Activities on Materials for Fusion Power Reactors", *Nucl. Fusion*, **47** (2007) 696-717
9. A. Kohyama, A. Hishinuma, D.S. Gelles, R.L. Klueh, W. Dietz, K. Ehrlich, "Low-activation ferritic and martensitic steels for fusion application", *J. Nucl. Mater.*, **233-237** (1996) 138-147
10. JOHN S. BENJAMIN, "Dispersion Strengthened Superalloys by Mechanical Alloying", *Metall. Transactions*, **1** (1970) 2943-2951
11. J.S. Lee, A. Kimura, S. Ukai, M. Fujiwara, "Effects of hydrogen on the mechanical properties of oxide dispersion strengthening steels", *J. Nucl. Mater.*, **329-333** (2004) 1122-1126
12. Peng Dou, Akihiko Kimura, Takanari Okuda, Masaki Inoue, Shigeharu Ukai, Somei Ohnuki, Toshiharu Fujisawa, Fujio Abe, "Effects of extrusion temperature on the nano-mesoscopic structure and mechanical properties of an Al-alloyed high-Cr ODS ferritic steel", *J. Nucl. Mater.*, **417** (2011) 166-170
13. M.R James, S.A Maloy, F.D Gac, W.F Sommer, J Chen, H Ullmaier, "The mechanical properties of an Alloy 718 window after irradiation in a spallation environment", *J. Nucl. Mater.*, **296** (2001) 139-144

14. Akihiko KIMURA, Han-Sik CHO, Naoki TODA, Ryuta KASADA, Kentaro YUTANI, Hirotatsu KISHIMOTO, Noriyuki IWATA, Shigeharu UKAI, Masayuki FUJIWARA, "High Burnup Fuel Cladding Materials R&D for Advanced Nuclear Systems: Nano-sized oxide dispersion strengthening steels", *J. Nucl. Sci. and Tech.*, **44** (2007) 323-328
15. A. Kimura, R. Kasada, N. Iwata, H. Kishimoto, C.H. Zhang, J. Isselin, P. Dou, J.H. Lee, N. Muthukumar, T. Okuda, M. Inoue, S. Ukai, S. Ohnuki, T. Fujisawa, T.F. Abe, "Development of Al added high-Cr ODS steels for fuel cladding of next generation nuclear systems", *J. Nucl. Mater.*, **417** (2011) 176-179
16. Hwanil Je, Akihiko Kimura, "Stress corrosion cracking susceptibility of oxide dispersion strengthened ferritic steel in supercritical pressurized water dissolved with different hydrogen and oxygen contents", *Corrosion Sci.*, **78** (2014) 193-199
17. Shigeharu UKAI, Toshio NISHIDA, Hirokazu OKADA, "Development of Oxide Dispersion Strengthened Ferritic Steels for FBR Core Application, (I) Improvement of Mechanical Properties by Recrystallization Processing", *J. Nucl. Sci. Technol.*, **34** (1997) 256-263
18. Shigeharu UKAI, Toshio NISHIDA, Takanari OKUDA, Tunemitsu YOSHITAKE, "Development of Oxide Dispersion Strengthened Steels for FBR Core Application, (II) Morphology Improvement by Martensite Transformation", *J. Nucl. Sci. Technol.*, **35** (1998) 294-300
19. T. Yoshitake, T. Ohmori, S. Miyakawa, "Burst properties of irradiated oxide dispersionstrengthened ferritic steel claddings", *J. Nucl. Mater.*, **307-311** (2002) 788-792
20. A. Kimura, S. Ukai, M. Fujiwara, "R&D of oxide dispersion strengthening steels for high burn-up fuel claddings", *Proc. Int. Cong. Advances in Nuclear Power Plants, (ICAPP-2004) ISBN: 0-89448-680-2, CD-ROM file, (2004) 2070-2076*
21. H.S. Cho, A. Kimura, S. Ukai, M. Fujiwara, "Corrosion properties of oxide dispersion strengthened steels in super-critical water environment", *J. Nucl. Mater.*, 329-333 (2004) 387-391
22. A.J. Foreman, M.J. Markin, "Dislocation movement through random arrays of obstacles", *Philosophical Magazine*, **14** (1966) 911-924

23. M.J. Alinger, G.R. Odette, G.E. Lucas, "Tensile and fracture toughness properties of MA957: implications to the development of nano composited ferritic alloys", *J. Nucl. Mater.*, **307-311** (2002) 484-489
24. P. Olier, J. Malaplate, M. H. Mathon, D. Nunes, D. Hamon, L. Toualbi, Y. de Carlan, L. Chaffron, "Chemical and microstructural evolution on ODS Fe-14CrWTi steel during manufacturing stages", *J. Nucl. Mater.*, **428**, (2012) 40-46
25. 31. R. Kasada, N. Toda, H.S. Cho, A. Kimura, "Tensile Deformation Behavior of Oxide-Dispersion Strengthened Ferritic Steels", *Proc. Int. Cong. Advances in Nuclear Power Plants* (2005) 5328
26. Marta Serrano, Mercedes Hernández-Mayoral, Andrea García-Junceda, "Microstructural anisotropy effect on the mechanical properties of a 14Cr ODS steel", *J. Nucl. Mater.*, **428** (2012) 103-109
27. K. Turba, R.C. Hurst, P. Hähner, "Anisotropic mechanical properties of the MA956 ODS steel characterized by the small punch testing technique", *J. Nucl. Mater.*, **428** (2012) 76-81
28. R. Kasada, S.G. Lee, J. Isselin, J.H. Lee, T. Omura, A. Kimura, T. Okuda, M. Inoue, S. Ukai, S. Ohnuki, T. Fujisawa, F. Abe, "Anisotropy in tensile and ductile–brittle transition behavior of ODS ferritic steels", *J. Nucl. Mater.*, **417** (2011) 180-184
29. Ch. Eiselt, M. Klimenkov, R. Lindau, A. Möslang, G.R. Odette, T. Yamamoto, D. Gragg, "Tensile and fracture toughness properties of the nanostructured oxide dispersion strengthened ferritic alloy 13Cr–1W–0.3Ti–0.3Y₂O₃", *J. Nucl. Mater.*, **417** (2011) 193-196
30. S.K. Karak, J.DuttaMajumdar, Z.Witczak, W.Lojkowski, I.Manna, "Microstructure and mechanical properties of nano-Y₂O₃ dispersed ferritic alloys synthesized by mechanical alloying and consolidated by hydrostatic extrusion", *Mater. Sci. Eng. A*, **580** (2013) 231-241
31. Z. Oksiuta, M. Lewandowska, K.J. Kurzydowski, N. Baluc, "Influence of hot rolling and high speed hydrostatic extrusion on the microstructure and mechanical properties of an ODS RAF steel", *J. Nucl. Mater.*, **409** (2011) 86-93
32. Tae Kyu Kim, Chang Soo Bae, Do Hyang Kim, Jin Sung Jang, Sung Ho Kim, Chan Bock Lee, Do Hee Hahn, "Microstructural observation and tensile isotropy of an austenitic ODS steel", *Nucl. Eng. Tech.*, **40** (2008) 305-310

33. Sanghoon Noh, Ryuta Kasada, Akihiko Kimura, Seung Hwan C. Park, Satoshi Hirano, "Microstructure and mechanical properties of friction stir processed ODS ferritic steels", *J. Nucl. Mater.*, **417** (2011) 245-248
34. J. Saito, T. Suda, S. Yamashita, S. Ohnuki, H. Takahashi, N. Akasaka, M. Nishida, S. Ukai, "Void formation and microstructural development in oxide dispersion strengthened ferritic steels during electron-irradiation", *J. Nucl. Mater.*, **258-263** (1998) 1264-1268
35. F. J. Humphreys and M. Hatherly "Recrystallization and related annealing phenomena 2nd ed.", *Elsevier*, 2004
36. H. Hadraba, B. Fournier, L. Stratil, J. Malaplate, A.-L. Rouffié, P. Wident, L. Ziolek, J.-L. Béchade, "Influence of microstructure on impact properties of 9–18%Cr ODS steels for fusion/fission applications", *J. Nucl. Mater.*, **411** (2011) 112-118
37. Jeoung Han Kim, Thak Sang Byun, David T. Hoelzer, Seong-Woong Kim, BongHo Lee, "Temperature dependence of strengthening mechanisms in the nanostructured ferritic alloy 14YWT: PartI—Mechanical and microstructural observations", *Mater. Sci. Eng. A*, **559** (2013) 101-110
38. P.K.C. Venkatsurya, Z. Jia, R.D.K. Misra, M.D. Mulholland, M. Manohar, J.E. Hartmann Jr., "Understanding mechanical property anisotropy in high strength niobium-micro alloyed line pipe steels", *Mater. Sci. Eng. A*, **556** (2012) 194-210
39. Takehide Senuma, Kaoru Kawasaki, Yoshito Takemoto, "Recrystallization Behavior and Texture Formation of Rapidly Annealed Cold-Rolled Extralow Carbon Steel Sheets", *Mater. Trans.*, **47** (2006) 1769-1775
40. Yoshito Sugino, Shigeharu Ukai, Bin Leng, Naoko Oono, Shigenari Hayashi, Takeji Kaito, Satoshi Ohtsuka, "Grain Boundary Related Deformation in ODS Ferritic Steel during Creep Test", *Mater. Trans.*, **53** (2012) 1753-1757
41. S.V. Mehtonen, L.P. Karjalainen, D.A. Porter, "Hot deformation behavior and microstructure evolution of a stabilized high-Cr ferritic stainless steel", *Mater. Sci. Eng. A*, **571** (2013) 1-12
42. T.S. Chou, H.K.D.H. Bhadeshia, "Recrystallization temperatures in mechanically alloyed oxide-dispersion-strengthened MA956 and MA957 steels", *Mater. Sci. Eng. A*, **189** (1994) 299-233

43. H.R.Z. Sandim, R.A. Renzetti, A. F. Padilha, D. Raabe, M. Klimenkov, R. Lindaud, A. Möslang, "Annealing behavior of ferritic–martensitic 9%Cr–ODS–Eurofer steel", *Mater. Sci. Eng. A*, **527** (2010) 3602-3608
44. Chun-Liang Chen, You-Ming Dong, Shu-Mei Fu, "Strain Heterogeneity, Recovery and Recrystallization of Nanostructured ODS Alloys during Cold Deformation", *Mater. Trans.*, **53** (2012) 1795-1800
45. R.A. Renzetti, H.R.Z. Sandim, M.J.R. Sandim, A.D. Santos, A. Möslang, D. Raabe, "Annealing effects on microstructure and coercive field of ferritic–martensitic ODS Eurofer steel", *Mater. Sci. Eng. A*, **528** (2011) 1442-1447
46. R.A. Renzetti, H.R.Z. Sandim, R.E. Bolmaro, P.A. Suzuki, A. Möslang, "X-ray evaluation of dislocation density in ODS-Eurofer steel", *Mater. Sci. Eng. A*, **534** (2012) 142-146
47. H.R.Z. Sandim, A.O.F. Hayama, D. Raabe, "Recrystallization of the ODS super alloy PM-1000", *Mater. Sci. Eng. A*, **430** (2006) 172-178
48. T. Grosdidier, E. Suzon, F. Wagner, "Primary recrystallization in an ODS FeAl alloy: an effective way to modify texture and microstructure", *Intermetallics*, **12** (2004) 645-654
49. P. Dou, A. Kimura, T. Okuda, M. Inoue, S. Ukai, S. Ohnuki, T. Fujisawa, F. Abe, "Polymorphic and coherency transition of Y–Al complex oxide particles with extrusion temperature in an Al-alloyed high-Cr oxide dispersion strengthened ferritic steel", *Acta Mater.*, **59** (2011) 992-1002
50. R. Kasada, N. Toda, K. Yutani, H.S. Cho, H. Kishimoto, A. Kimura, "Pre- and post-deformation microstructures of oxide dispersion strengthened ferritic steels", *J. Nucl. Mater.*, **367-370** (2007) 222-228
51. J.H. Schneibel, M. Heilmaier, W. Blum, G. Hasemann, T. Shanmugasundaram, "Temperature dependence of the strength of fine- and ultrafine-grained materials", *Acta Mater.*, **59** (2011) 1300-1308
52. K. Yabuuchi, Doctor's thesis, *Kyoto University* (2012)
53. Young Sik Ahn, Characteristic and application of nuclear reactor materials (2011)

54. M. Klimiankou, R. Lindau, A. Möslang, "TEM characterization of structure and composition of nanosized ODS particles in reduced activation ferritic–martensitic steels", *J. Nucl. Mater.*, **329-333** (2004) 347-351
55. Kiyohiro Yabuuchi, Ryuta Kasada, Akihiko Kimura, "Effect of Mn addition on one-dimensional migration of dislocation loops in body-centered cubic Fe", *Acta. Mater.*, **61** (2013) 6517-6523
56. H. Regle, A. Alamo, "Secondary recrystallization of oxide dispersion strengthened ferritic alloys", *Journal De Physique IV*, **3** (1993) 727-730
57. H.K.D.H. Bhadeshia, "Recrystallisation of practical mechanically alloyed iron-base and nickel-base superalloys" , *Mater. Sci. Eng. A*, **223** (1997) 64-77

Chapter 2

Microstructure and Mechanical Property of Annealing Processed ODS Ferritic Steels

2.1 Introduction

High performance characteristic features of ODS steels comes from fine microstructures consisted of dispersed nano-sized oxide particles with high number density and very fine grains. Among the issues for practical application of ODS ferritic steels, tube processing is most critical. ODS steels are often hot-extruded as a fabrication process and grains are elongated along with the extrusion direction, which causes an anisotropy in their mechanical properties showing less ductile properties in the radial direction. In order to reduce the anisotropy, recrystallization behavior has been investigated with keeping performance of ODS steels [1-5].

The chemical compositions such as Cr and Al affect not only corrosion resistance but also grain morphology with influencing oxide particles dispersion morphology. However, the detail of the effects has not been cleared yet. The recrystallization behavior is expected to be different between Al-added and Al-free ODS steel since Al has a strong effect on the oxide particles dispersion morphology. Oxide particles may have a grain boundary pinning effect as well as a strengthening effect. Therefore, an ODS steel and a ferritic steel without oxide particles are compared to investigate the effect of oxide particle on the recrystallization behavior. In this research, the recrystallization behavior and microstructure change affected by annealing processing of a 16-Cr conventional ferritic steel, SUS430, is investigated. In comparison to SUS430, the recrystallization behavior of 15Cr-ODS ferritic steels with and without Al addition is investigated with focusing on the correlation between microstructure and mechanical properties. The effect of recrystallization on the anisotropy and the specimen size effect on mechanical properties are also investigated for these two ODS steels.

2.2 Experimental procedure

2.2.1 Materials

2.2.1.1 ODS steels

The ODS steels used in this study are an Al-added ODS steel, composed of Fe (Bal.)-15Cr-2W-4Al-0.5Zr-0.33Y₂O₃ and an Al-free ODS steel, Fe (Bal.)-15Cr-2W-0.2Ti-0.33Y₂O₃. Chemical compositions of the ODS steels are shown in Table 2-1. These ODS ferritic steels were fabricated as follows; pre-alloyed powders and Y₂O₃ powder were mechanically alloyed by an attriter under Ar gas atmosphere. Mechanical alloying was performed at a rotation speed of 220 rpm for 48 hours. After mechanical alloying, fine powders were sieved out and encapsulated in a capsule made of mild steel. After the capsules were degassed in a vacuum of 10⁻³ torr. at 400 °C for 3h, hot extrusion was carried out at 1150 °C to shape into a rod with 25 mm diameter. The annealing processing at 1150 °C were performed for 1 hour for straightening and followed by air-cooling. The schematic diagram of processing for ODS steel is shown in Fig. 2-1 [3, 6, 7]. Through several experience of material fabrication processing, relatively large oxide particles of Al-Y complex oxide are observed in Al-added ODS steel, and these particles are believed to cause poor mechanical properties. However, a small amount of Zr addition to the Al-added ODS steel resulted in the refinement of oxide particles. It was shown that many Al-Y complex oxide particles are replaced by Zr-Y complex oxide by adding a small amount of Zr [8-10].

3.2.1.2 SUS 430 steels

SUS430 steel (Nilaco. Co. Japan, Table 2-2), of which the Cr content is similar to the ODS steels is used. 15Cr-ferritic alloy is contained high Cr, no transformation to γ phase or σ phase at all temperature area until liquid phase in ideal Fe-Cr phase diagram as shown Fig. 2-2.

Table 2-1 Chemical composition of Al-added and Al-free ODS ferritic steel

Elements	Composition (wt %)	
	Al-added	Al-free
Type		
Fe	Bal.	Bal.
C	0.031	0.045
Si	0.02	0.03
Mn	0.02	0.03
P	0.005	0.005
S	0.0015	0.0015
Cr	14.7	13.6
W	1.0	1.9
Al	3.3	0.02
Ti		0.16
Zr	0.51	
Y ₂ O ₃	0.33	0.33
Ex.O	0.04	0.04

*Ex.O = Total oxygen conc. - oxygen conc. in Y₂O₃

Table 2-2 Chemical composition of SUS 430

Elements	Fe	Cr	C	Si	Mn	Ni	P	S
wt %	Bal.	16.00	0.018	0.15	0.74	0.28	≤0.040	≤0.030

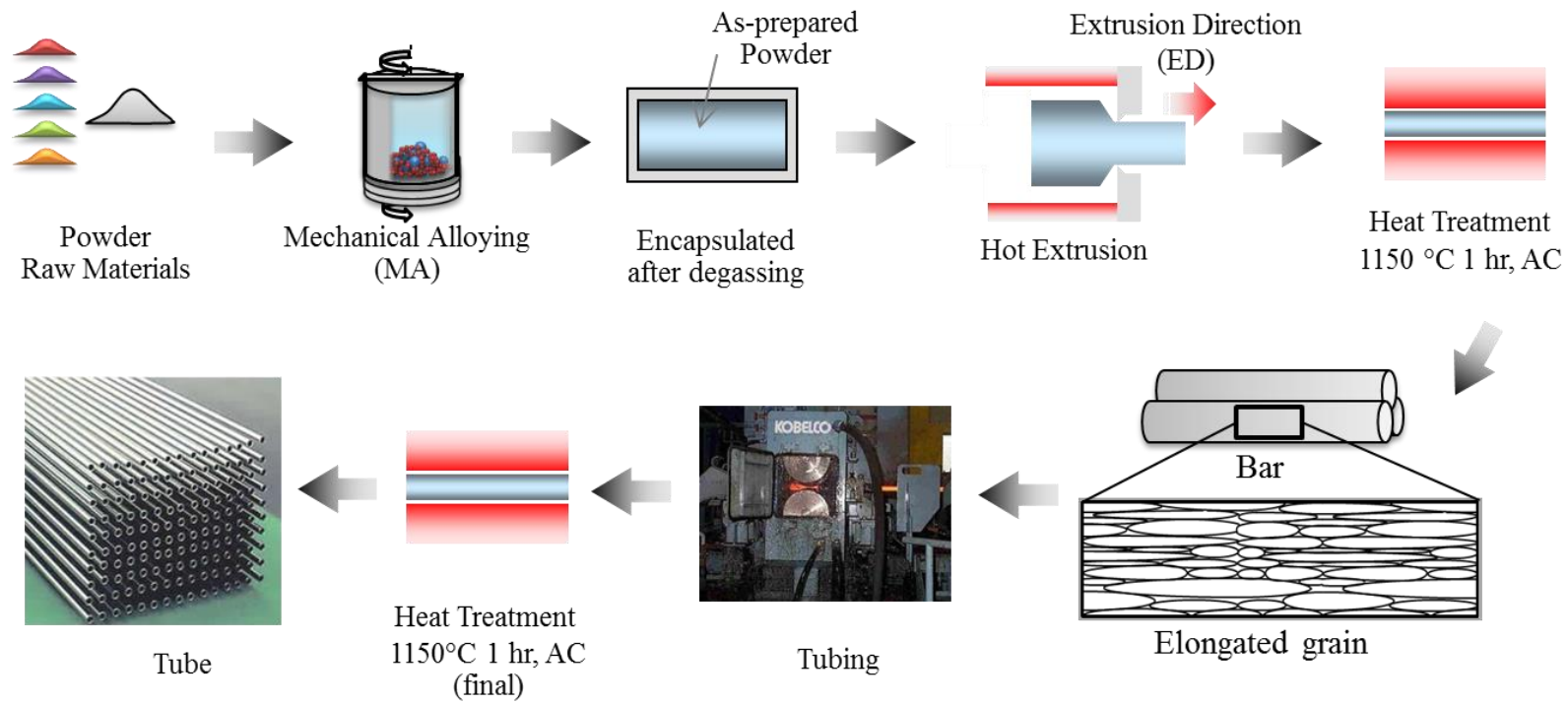


Figure 2-1 Fabrication schematic of ODS ferritic steel [3, 6, 7]

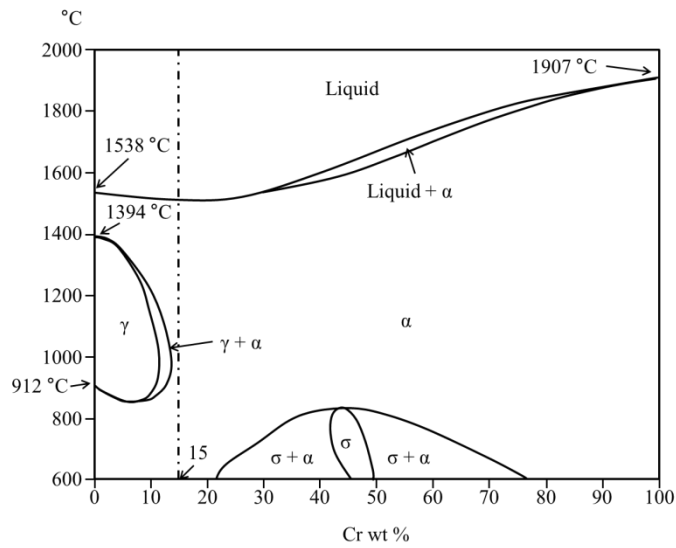


Figure 2-2 Fe-Cr phase diagram in ideal condition

2.2.2 Recrystallization treatment

The specimens, of which the geometry measures $10 \times 10 \times 1 \text{ mm}^3$, for annealing experiments to investigate recrystallization behavior were prepared from SUS 430 steel plates in as-received condition and 40 % cold rolled condition. Isothermal annealing was carried out at each temperature ranging from 300 °C to 1000 °C for 1 hour with a step of 100 °C. The microstructures are observed and the change of Vickers hardness is examined. ODS steels were fabricated from the bars to measure the recrystallization temperature and their microstructure evolution. Both Al-added and Al-free ODS steels were isothermally annealed at each temperatures ranging from 1050 °C to 1400 °C with a step of 50 °C for 1 hour. Hot press machine (versatile high temperature furnace, FVPHP-R-5, Fuji Dempa Kogyo Co.) was used for annealing in a vacuum condition as shown Fig. 2-3. The heating rate was 30 °C/min followed by furnace cooling.

After annealing processing, microstructures were observed by scanning electron microscope and Vickers hardness was measured at a loading of 1 kgf for 10 seconds.

2.2.3 Microstructure observation

For microstructural observation, the specimens after annealing were mechanically grinded with #800, #1200, #2400 and #4000 emery SiC papers. And then they were buff-polished with diamond paste in order of 6, 3, 1 and 0.25 μm diameters. Finally, colloidal silica polishing with 0.04 μm was performed [11]. The grain morphology was observed by field emission scanning electron microscope (FE-SEM) installed in field emission electron probe micro analyzer (FE-EPMA, JXA-8500FK, JEOL co., Japan).

Electron backscattering diffraction pattern (EBSD, Ultra-55, Zeiss Co., Germany) technique was also employed to analyze the texture, grain size and grain orientation as a useful crystallographic information. EBSD is known as an electron backscatter diffraction method for lattice structure determination using the Kikuchi pattern induced by back-scattered X-ray. To collect these patterns, the sample is tilted in SEM to approximately 70° as shown in Fig. 2-4. Observed surface is ND-RD surface (//TD). The collected data was analyzed by TSL OIM software.

The 3mm TEM discs specimens for transmission electron microscopy (TEM) observation were sampled from the specimens before and after annealing both Al-added and Al-free ODS steel. Then, they were mechanically ground to a thickness of 60 μm and electro polishing with HClO_4 and CH_3OH (1:19) at 20 V for 3~4minutes using Tenupole machine. Finally it is prepared by the ion beam milling

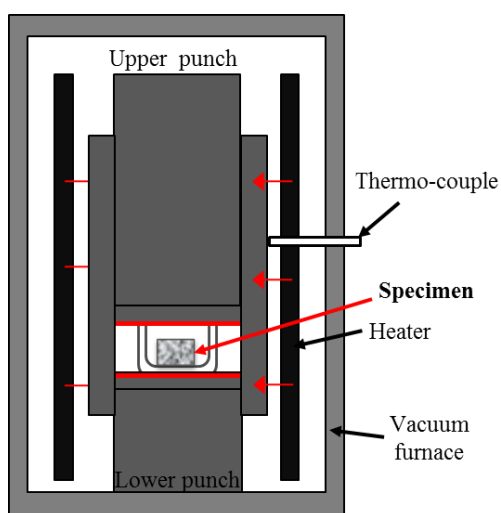


Figure 2-3 Annealing method using hot press, FVPHP-R-5

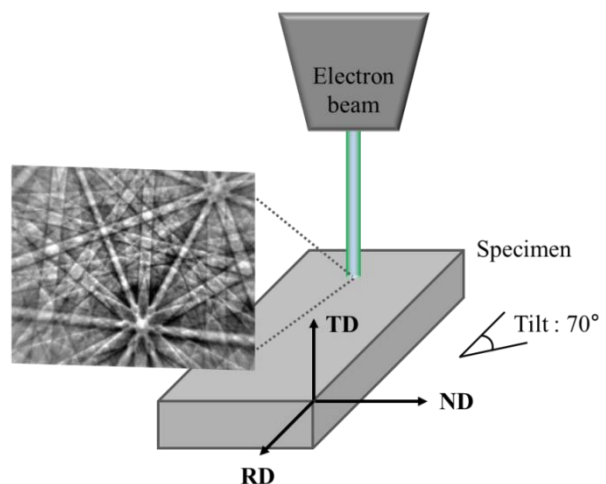


Figure 2-4 Electron backscattering diffraction pattern (EBSD) system

technique with Gentle mill machine up to the specimen thickness below 100 nm. The effect of annealing processing on the oxide particle distribution morphology was evaluated by TEM (JEM-2010, JEOL co., Japan) with an acceleration voltage of 200 kV.

2.2.4 Measurement of mechanical properties

2.2.4.1 Micro Vickers hardness test

Micro Vickers hardness measurements were performed after isothermal annealing using a square-based diamond-pyramid indenter with an included angle of 136 ° between opposite faced. The load range is usually between 1~50 kgf, meanwhile, it is between 0.05~1000 gf in a case of micro-Vickers hardness test. As a result of the indenter's shape, an impression on the surface of the specimen will be a square. Thus, when test load is P (kgf) and average diagonal length of squared impression is d (mm), the Vickers hardness, Hv, can be expressed as;

$$H_v = (2P/d^2) \sin (\theta/2) = 1.8544 P/d^2 \quad (2.1)$$

In this study, Micro Vickers Hardness tester (HM-102, Akashi co. Japan) was used to evaluate the hardness before and after annealing with a load of 1kgf for 10 seconds [12]. The averaged data was obtained from at least ten measurements for each specimen. The sample surface for the hardness evaluation was finally polished with a diamond paste of 6 μm.

2.2.4.2 Miniaturized tensile test

Anisotropy in the mechanical properties was investigated before and after annealing with miniaturized tensile specimens. The geometry of tensile specimen (SS-J2 sheet type) [6] measures 5 mm (l) x 1.2 mm (w) x 1.2 mm (t). For anisotropy examination, tensile test specimens were fabricated with three sampling directions relative to the extruded direction, which were L (longitudinal direction), Q (45 ° direction) and C (transverse direction) as shown Fig. 2-5. The specimen thickness was mostly 1.2 mm that is same with the specimen width to consider the effect of the shape of cross sectional area in comparison to thinner specimens with a thickness of 0.5 mm and 0.25 mm to verify the specimen

thickness effect on tensile properties. To investigate tensile property differences between before and after annealing at 1350 °C, the miniaturized tensile specimens were deformed at a strain rate of $6.7 \times 10^{-4} \text{ s}^{-1}$ at room temperature and elevated temperatures at 700 °C in a vacuum ($< 5 \times 10^{-5}$ torr) with a tensile test machine (205XK-KC, INTESCO co., Japan).

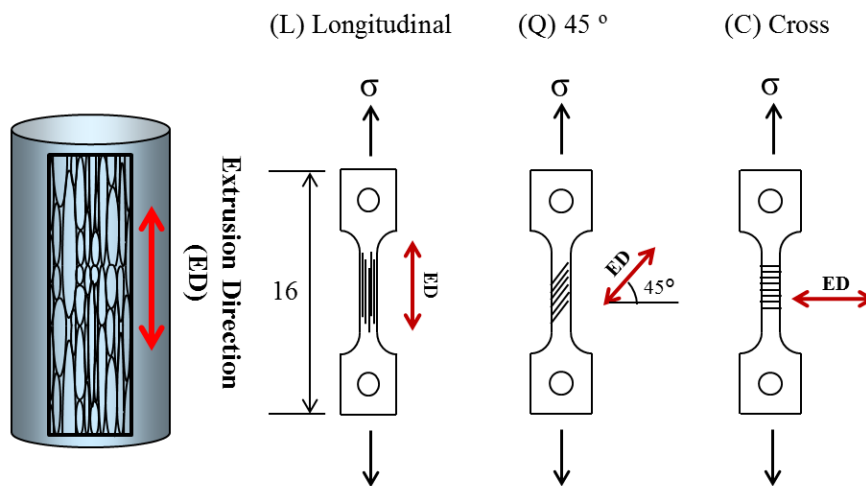


Figure 2-5 Geometric and directions of tensile specimens

2.3 Results and discussions

2.3.1 Annealing behavior of SUS 430

2.3.1.1 Microstructure change

Fig.2-6 shows the grain morphologies of both as-received and 40 % cold rolled SUS 430 after annealing at each temperature. The grain morphologies of as-received specimen were not significantly changed until at 700 °C, and the grain size after annealing at 800 °C was a little bigger than that before annealing. In case of 40 % cold rolled specimen, the grains are elongated along with cold rolling direction before annealing. After annealing at 700 °C, recrystallization occurred and their grain shape morphology was exquiauxed with reducing anisotropy. These grains grew a little by annealing at 800 °C. Above 900 °C, fine microstructure was observed near grain boundaries in both as-received and 40 % cold rolled specimens, and the amount of fine microstructure is gradually increased at 1000 °C as shown in SEM images. The result of EBSD analysis, as shown in Fig, 2-7, indicates that sub-grain boundaries below 5 ° are formed in 40 % cold rolled specimen before annealing, which is shown as white lines inside the grains. It is considered that the dislocations generated by cold rolling are thermally polygonized by annealing. The fine sub-grains created above 900 °C have no preferred orientation texture. Also, they appear to increase at 1000 °C in comparison to that at 900 °C. The fine microstructure may be secondary phase from γ phase, which is resided during annealing process at above 900 °C. Fig. 2-8 (a) shows an Fe-Cr phase diagram with 0.05 wt.% C. As carbon is stabilizer of austenitic phase, the upper limit Cr concentration beyond which austenite no longer forms is increased with addition of carbon. SUS 430 contained about 0.018 wt% C. Referring to Fe-Cr-C ternary phase diagram, the stainless steel has not only ferritic structure but also austenitic phase in the range of Cr content 12-18 % in addition with 0.05 wt.% C at elevated temperatures (Fig. 2-8, (b)). L. Colombier and J. Hochmann [13] reported that martensite phase were observed in the ferrite phase of Fe-17 % Cr stainless steel after water quenching from 1200 °C. Also, the fraction of austenitic phase was increased with increasing carbon contents. Therefore, it is considered that the fine microstructure observed in this study stems from the austenite phase, even it is very small amounts. According to Sourmail [14], $M_{23}C_6$ is generated from austenitic state. Because nucleation is relatively easier on

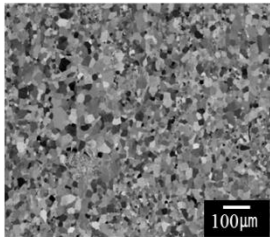
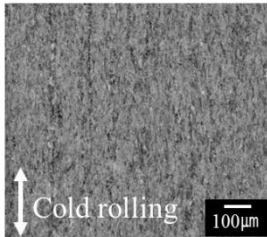
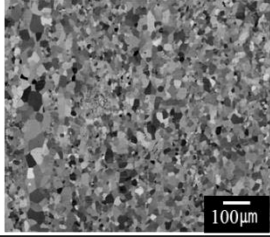
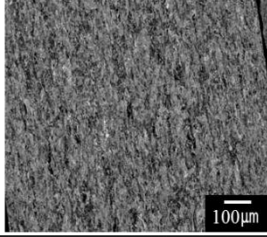
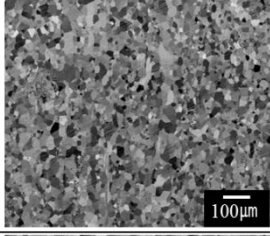
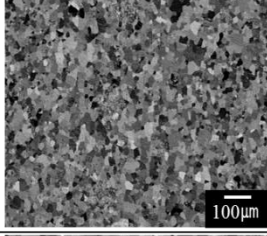
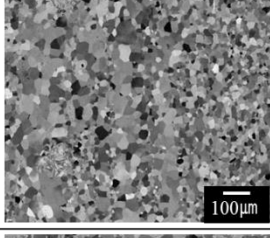
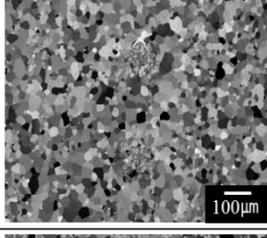
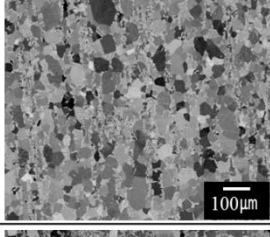
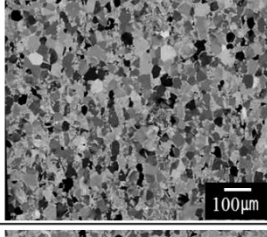
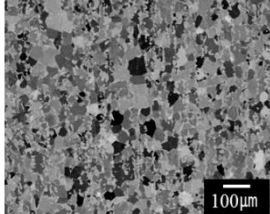
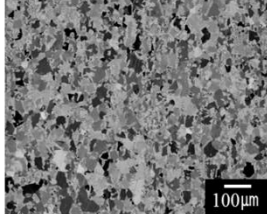
Temperature	As-received	40% cold rolled
Before annealing		
600 °C		
700 °C		
800 °C		
900 °C		
1000 °C		

Figure 2-6 Grain morphologies both of as-received and 40% cold rolled SUS430 after annealing at each temperature

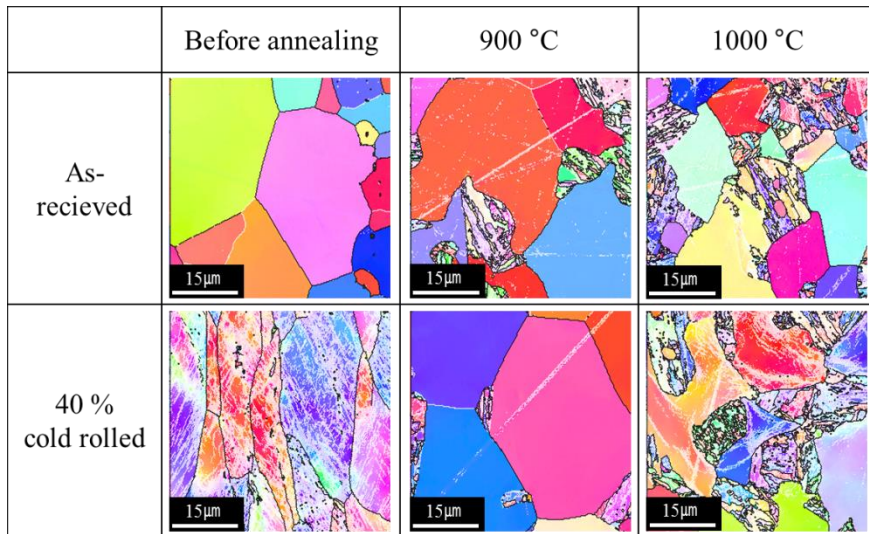


Figure 2-7 Grain orientation map of as-received and 40 % cold rolled SUS 430 after annealing

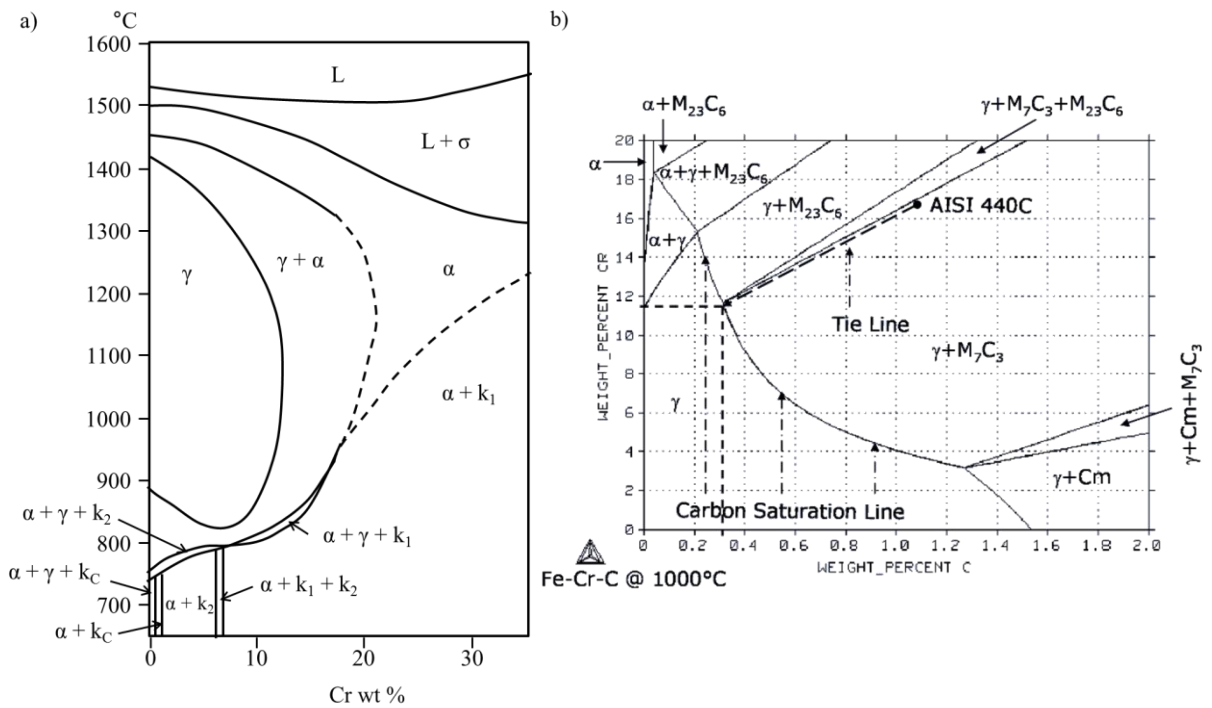


Figure 2-8 Fe-Cr isothermal phase diagram according to Cr and C contents; (a) Fe-Cr phase as temperature and Cr contents and (b) Fe-Cr-C phase diagram at 1000 °C [17]

grain boundaries, there is a very strong tendency for localized precipitation. Precipitation also does occur after longer exposure at high temperatures. Depending on the composition, $M_{23}C_6$ can be found on grain boundaries after only a few minutes at temperatures around 750 °C. The range of temperature in which sensitization occurs is bounded in the lower temperatures by the very slow kinetics of diffusion controlled transformations, and in the higher temperatures, by the fact that chromium depletion is less pronounced at higher temperatures [15, 16]. Since the carbon concentration is 0.018 wt.% in the steel, the amount of carbides is considered to be small.

2.3.1.2 Hardness change

Mechanical properties are essentially related to microstructure. Fig. 2-9 is the Vickers hardness of the as-received and 40% cold rolled SUS430 measured after isothermal annealing at each temperature. The hardness of as-received SUS 430 is almost unchanged until heating up to 850 °C, which reflects no change in grain size. In case of the 40 % cold rolled SUS 430, the hardness is higher than that of as-received specimen caused by high dislocation density by cold rolling process, as referred to earlier shown Fig. 2-7. The hardness of cold rolled specimens is abruptly reduced and becomes similar with that of as-received specimen at around 700 °C, at which dislocations generated by cold rolling recover. Also, recovery process is finished and recrystallization is progressed above 700 °C. Above 850 °C, the Vickers hardness of both as-received and 40 % cold rolled SUS 430 are increased.

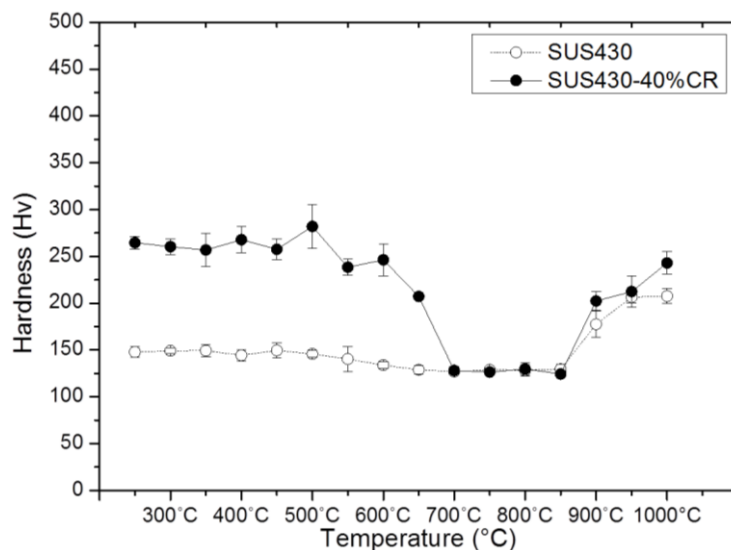


Figure 2-9 Vickers hardness of as-received and 40 % cold rolled SUS 430

2.3.2 Annealing behavior of ODS ferritic steels

2.3.2.1 Microstructure change

The strengthening mechanism of ODS steels is interpreted in terms of dispersion strengthening of fine oxide particles that obstruct migration of dislocation. In addition, the fine oxide particles also interrupt migration of grain boundaries, and consequently recrystallization of ODS steel is difficult to occur even annealed at elevated temperature. Fig. 2-10 shows the microstructure after annealing at each temperature by SEM and EBSD analysis. In case of Al-added ODS steel, the grains have anisotropy in their shape, elongated grains along with the extruded direction are observed before annealing. Also, the majority of planes in IPF (Inverse pole figure) are mostly {111} of blue colored area with a little area of {001} of red colored area. After isothermally annealed at each temperature for 1 hour below 1300 °C, grain morphologies are stable and textures are also not significantly changed, although the texture intensity is a little reduced. However, the grain after annealing at 1350 °C becomes abruptly bigger (noticed that scale bar of SEM image in Al-added ODS steel annealed at 1350 °C is different from the others). In contrast, in case of Al-free ODS steel, the elongated grains before annealing are finer than that of Al-added ODS steel, and that grain size are not considerably coarsened until annealing at 1400 °C. In IPF map, {111} planes are mainly distributed and a little {001}, {110} planes are observed. In both ODS steels, the grain orientation tends to rotate to $\langle 211 \rangle$ by annealing. The orientation of grains are examined more in detail in the (110) pole figure, as shown in Fig. 2-11. Before annealing, the RD orientation of both Al-added and Al-free ODS steel is $\langle 110 \rangle$, which is parallel to extruded direction. It is well known as a typical α -fiber texture (Fig. 2-12) in body centered cubic material, which is $\langle 110 \rangle // \text{RD}$, thus the grains on TD are rotating around $\langle 011 \rangle - \langle 111 \rangle$ edge of an orientation triangle between {001} $\langle 110 \rangle$ and {111} $\langle 110 \rangle$ [18-26]. After annealing at 1350 °C, the orientation of Al-added ODS steel is changed to {110} $\langle 100 \rangle$ that is so called Goss orientation accompanied by secondary recrystallization. Therefore, in Al-added ODS steel, the recrystallization accompanied by a significant grain growth occur at above 1300 °C. On the other hand, in Al-free ODS steel, the strong α -fiber texture is not changed until 1400 °C, even the intensity of {001} $\langle 110 \rangle$ becomes higher than that before annealing, suggesting that Al-free ODS steel appears to start to recrystallize at around 1400 °C.

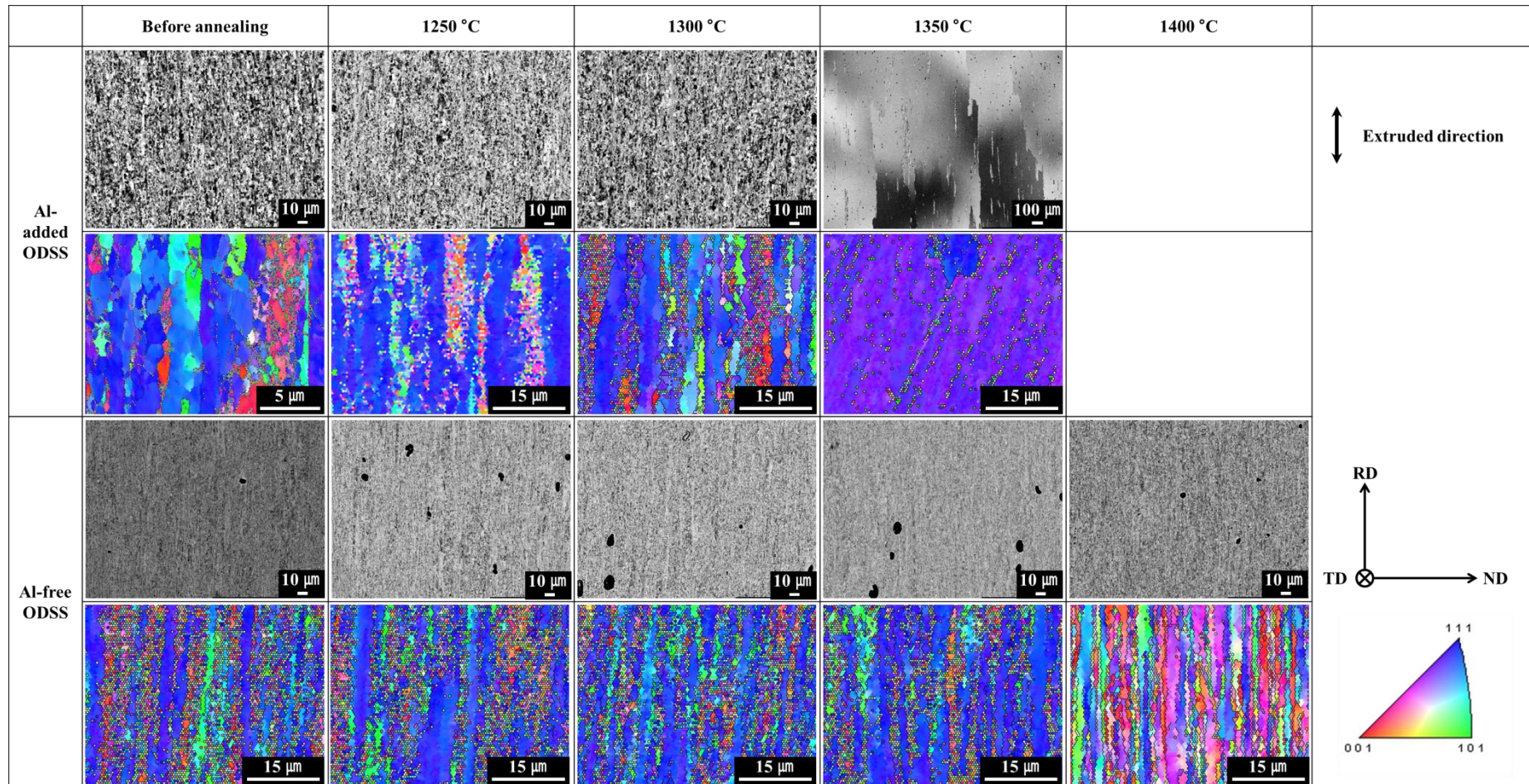


Figure 2-10 Grain morphologies of both Al-added and Al-free ODSS steel after annealed each temperature

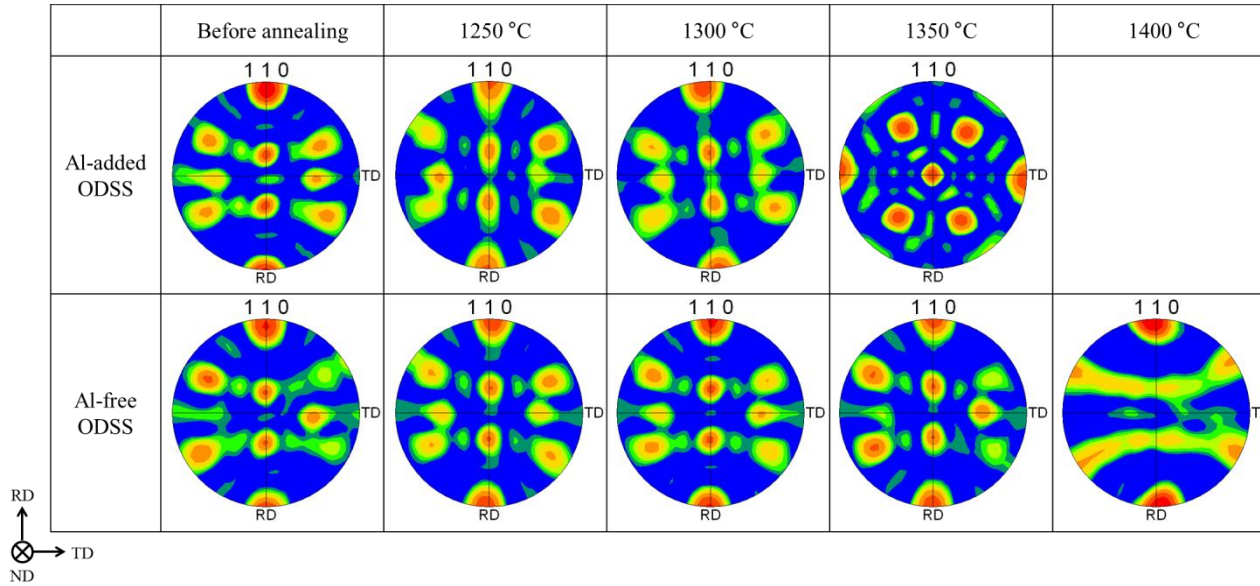


Figure 2-11 Pole figures of Al-added and Al-free ODS steel before and after annealing processing

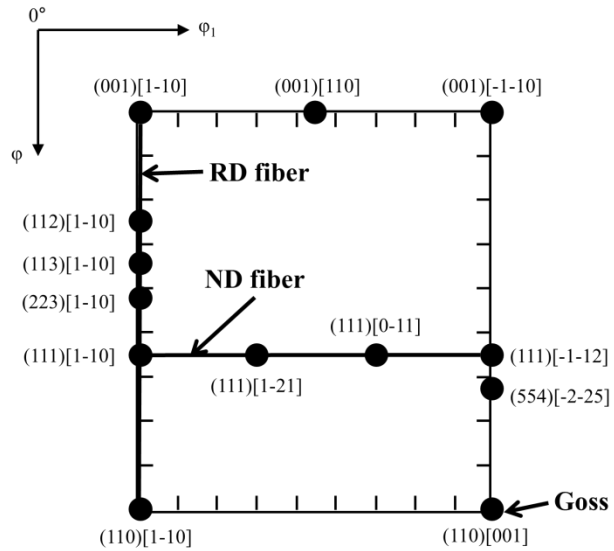


Figure 2-12 $\phi=45^\circ$ section of Euler space

The grain size of Al-added ODS steel is bigger than that of Al-free ODS steel both before and after annealing, and the recrystallization is also easy to occur in Al-added ODSS. The grain size was measured by a grain intercept method, in which the number of intersects of the lines and grain boundaries were counted and find the average of the length of segments between the intercepts to line length as below;

$$D_m = L \cdot P \cdot 10^3 / z \cdot V \quad (2.2)$$

where D_m is grain size, L is line length on the micrograph, P is the number of lines. Also, Z is the number of intersects on all the lines and V is magnification of micrograph. Since the grains have anisotropy in the shape, the lines were drawn perpendicular and parallel to the elongated grains. The obtained values are indicated in Table 2-3. The grain size of both Al-added and Al-free ODS steel gradually increases with increasing the annealing temperature. However, grain growth of Al-free ODS steel is very slow even up to 1400 °C.

Table 2-3 Grain size of annealed Al-added and Al-free ODS steel

Materials	Al-added ODSS	Al-free ODSS
Before annealing	1.55 μm	0.96 μm
1250 °C	1.80 μm	1.02 μm
1300 °C	2.03 μm	1.15 μm
1350 °C	230 μm	1.16 μm
1400 °C	--	1.29 μm

2.3.2.2 Mechanical property change

(1) Vickers hardness

Recrystallization is usually accompanied by a reduction in the strength and hardness of material caused by annealing out of dislocations and grain growth during annealing. Thus, the reduction of hardness reflects their recrystallization process and the temperature showing abrupt decrease in the

hardness can be defined as recrystallization temperature. The results of Vickers hardness test after isothermal annealing for 1 hour at each temperature are shown in Fig. 2-13. The hardness of both materials is reduced with increasing annealing temperature. Al-added ODS steel has lower hardness than that of Al-free ODS steel in whole regions.

In Al-added ODS steel, the hardness is abruptly decreased at above 1300 °C. It clearly indicates that Al-added ODS steel is recrystallized above 1300 °C in accordance with Vickers hardness change and also grain morphology change as shown Fig. 2-10 and 2-11. Therefore, the decrease in the hardness is due to annealing out of dislocations and grain growth by annealing. In case of Al-free ODS steel, there are two stages for reducing the hardness between 1250 °C and 1350 °C and above 1350 °C. But their grain size and deformation texture (also as shown Fig. 2-10 and 2-11) are not remarkably changed. Therefore, Al-free ODS steel is not fully recrystallized until 1400 °C. Although the grain morphology is not changed drastically, the Vickers hardness is reduced with increasing annealing temperature. It is considered that not recrystallization but recovery also determined the hardness, and strain induced a slight amount of grain boundary migration. The reduction of hardness at very high temperature is also other factors such as oxide particles dispersion morphology.

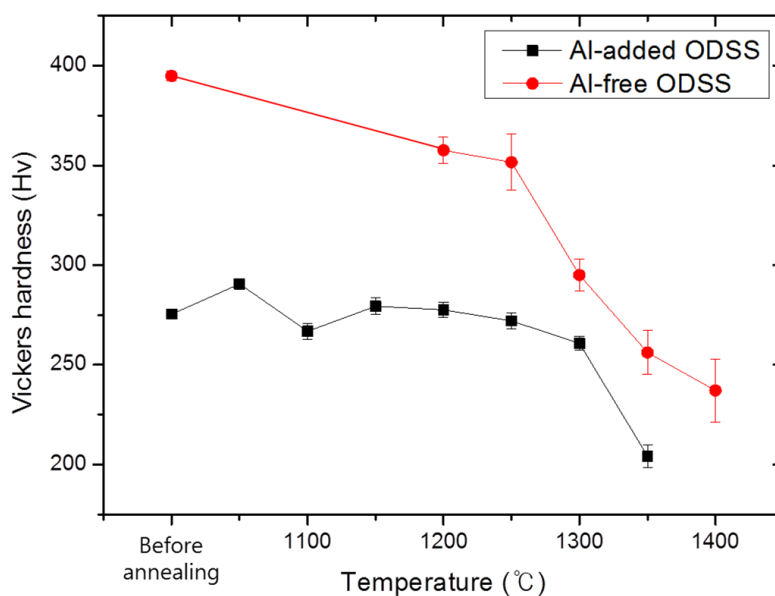


Figure 2-13 Vickers hardness of Al-added and Al-free ODS steel after annealing at each temperature

(2) Tensile properties

It was revealed by EBSD analysis that the grain shape has anisotropy related with elongated direction. The anisotropy in the mechanical properties was investigated in accordance to the recrystallization temperature of Al-added ODS steel. The specimens before and after annealing at 1350 °C for 1 hour were prepared for tensile test.

Fig. 2-14 is the stress-strain behavior of both Al-added and Al-free ODS steel with different specimen sampling directions and tested at room temperature before and after recrystallization. The specimen thickness is 1.2 mm so that the cross section is a square. After recrystallization, the tensile strength of Al-added ODS steel is significantly reduced but almost no change in the total elongation (notice the difference of yield strength and total elongation in right graph). As for anisotropy, the strength of L direction along with extruded direction is a little higher than that of Q direction of 45 ° with extruded direction before annealing, but it is almost same after recrystallization. Total elongation of C direction is lowest before and after recrystallization, but it is not significantly different with each direction and recrystallization behavior. The Al-free ODS steel shows similar behavior with the Al-added ODS steel even after the annealing at 1350 °C, indicating that the yield strength of L direction is higher, and the total elongation of C direction is the lowest before and after annealing. The total elongation is rarely changed by the annealing. Generally, the tensile strength of Al-free ODS steel is much higher than that of Al-added ODS steel in both before and after recrystallization treatment, even total elongation is similar each material. The yield stress difference between the specimens with and without annealing in Al-added ODS steel is bigger than that of Al-free ODS steel, which is considered to be due to the difference in grains and oxide particles morphology caused by Al addition. In case of Al-free ODS steel, the grain size is very small even after the annealing and the reduction of strength is considered to be due to annealing out of dislocations, that is, recovery but not by recrystallization.

Fig. 2-15 is grain morphologies in the necking part of Al-added ODS steel observed by FE-SEM. The grains of Al-added ODS steel are oriented with different directions, which are L, Q and C direction according to the extruded direction. Also, the edge of fracture surface is orientated with each grain direction. For example, the fracture surface of the specimen of C direction is parallel to the elongated grain direction. The difference in grain orientation reflected on the tensile results and fracture behavior. Fig. 2-16 shows the fracture surface observed from loading direction.

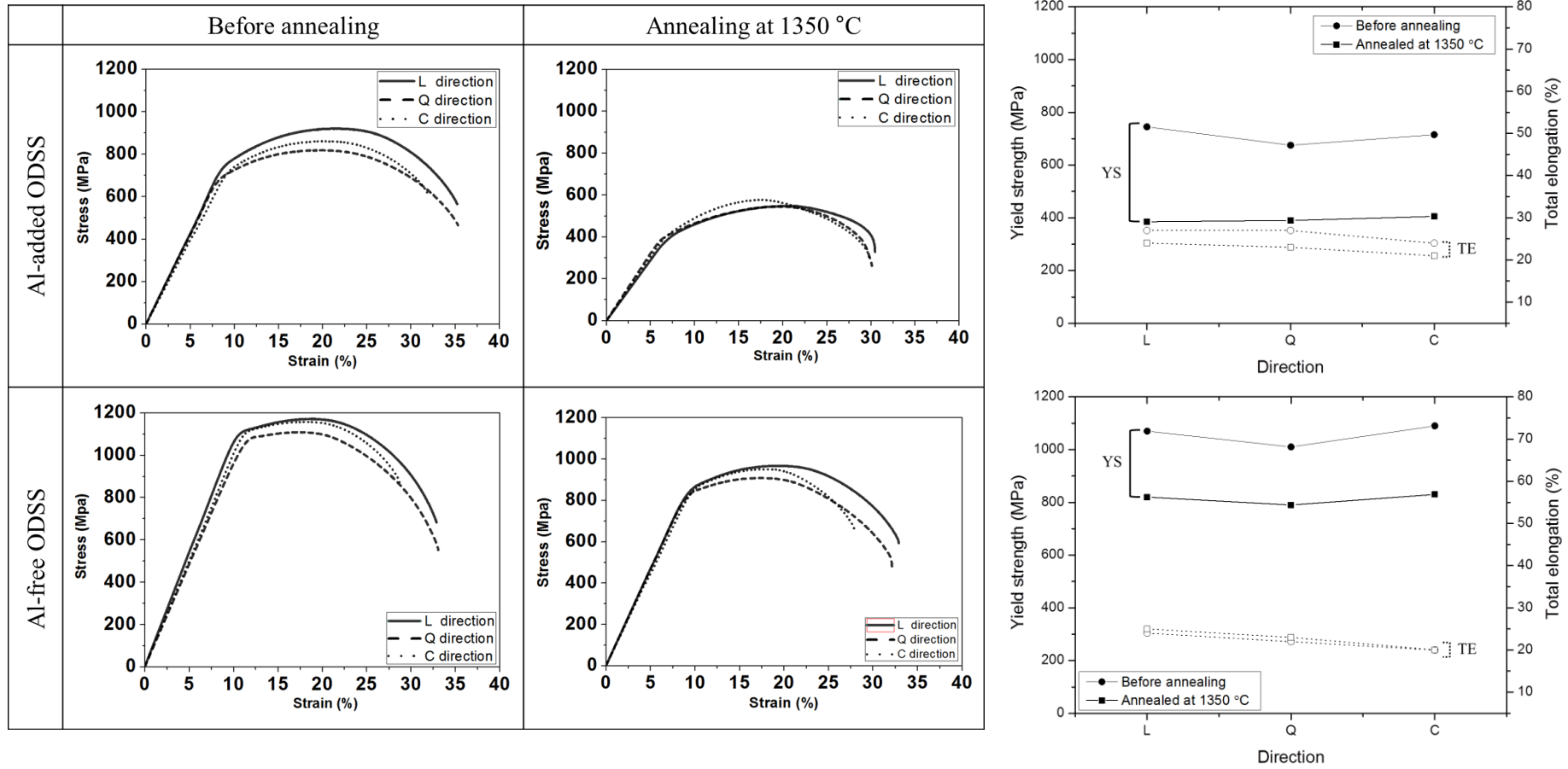


Figure 2-14 Stress-strain curves of both Al-added and Al-free ODS steel after tensile tests at room temperature

The specimen cross section is 1.2 mm square and there might be size effect on anisotropy in mechanical properties as discussed later. All the specimens show ductile fracture with small dimples on the fracture surface, and no effect of recrystallization on the fracture mode was observed, although ductile behavior appears more significant after recrystallization.

Al-added ODS steel is more ductile than that of Al-free ODS steel before and after annealing. Before annealing, the grain morphology is observed in the fracture surface, indicating that the fracture occurred along with grain morphology. It should be noticed that the specimens after recrystallization have coarse grains, which causes the isotropic rotation of slip plane and shows rather high reduction in area in Al-added ODS steel. In Al-free ODS steel, the fracture mode is also ductile showing very fine dimples in high magnification. After annealing at 1350 °C, the dimples are bigger and grain morphologies still remain along with each direction in fracture surface. These tensile test results show similar tendency with Vickers hardness as shown in Fig. 2-17. The lower mechanical properties of Al-added ODS steel than that of Al-free ODS steel is caused by softening effect of Al.

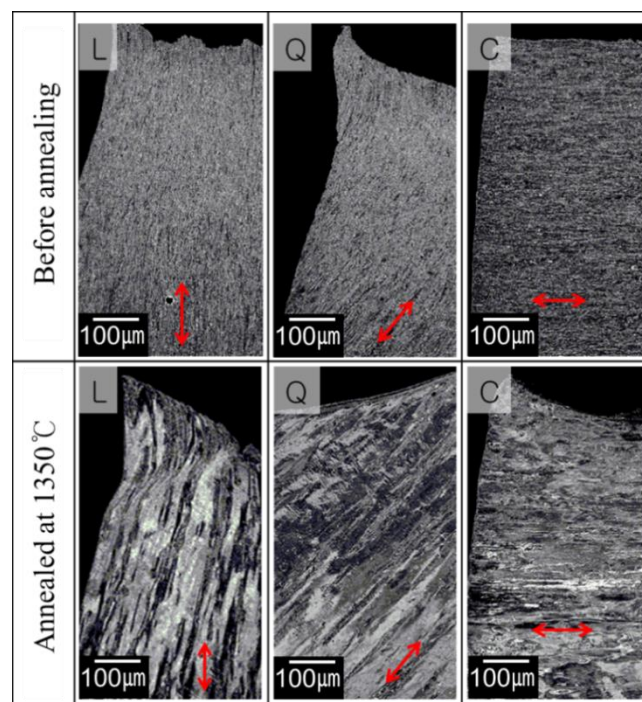


Figure 2-15 Grain morphology of Al-added ODS steel after tensile test at room temperature

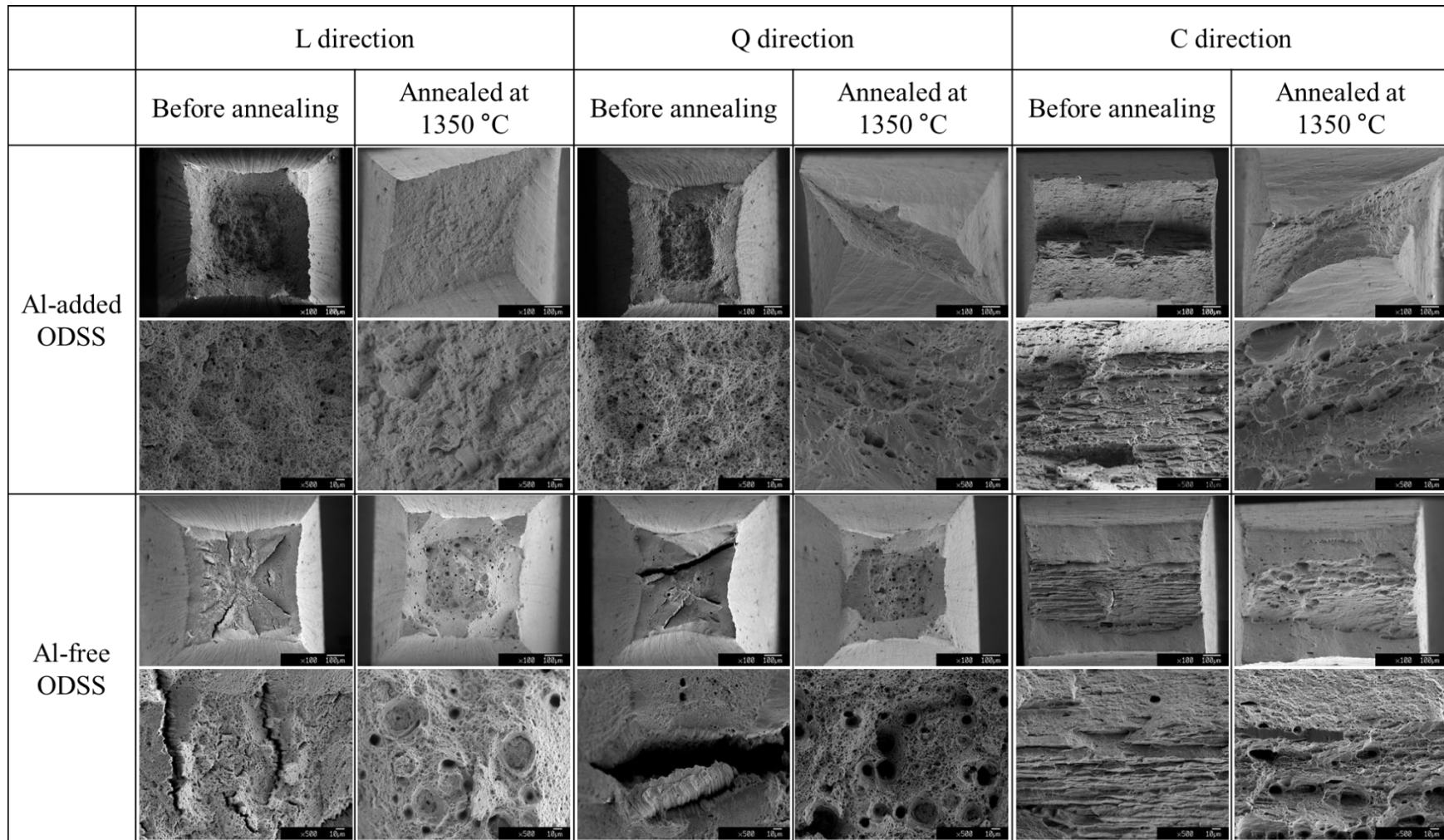


Figure 2-16 Fracture surfaces of both Al-added and Al-free ODS steel after tensile tests at room temperature

The results of tensile test at 700 °C are shown Fig. 2-18. As is expected that, in all of the case, the strength is lower and the elongation is larger than those at room temperature. The strength of Al-free ODS steel is still higher than that of Al-added ODS steel, and the difference is reduced in annealed specimens of both steels. In Al-free ODS steel, the difference in strength between before and after annealing is not large such as result at room temperature. The difference in elongation by annealing is conversely larger than that at room temperature. In contrast to the results at room temperature, a remarkable anisotropy is observed when tested at 700 °C. The strength of Al-added ODS steel is largest in the L direction, and the elongation appears smallest in the line of C direction both before and after annealing. In case of Al-free ODS steel, the yield strength is not significantly different before and after annealing, but the total elongation is particularly noticeable to change in Q and C direction. There is a large difference among three directions: L direction is the highest and C direction is the lowest. After annealing, the elongation of L direction is not changed but it is larger in Q direction, which almost same with L direction. C direction has the lowest elongation but it is also increased after annealing. The each specimen of Al-added ODS steel has a much larger elongation than that of Al-free ODS steel, although the change by the annealing is significant in Al-added ODS steel. As shown in Fig. 2-19, the size of dimples on fracture surface of all cases are bigger than that of the specimens tested at room temperature, also the specimen of C direction fractured along grain growth direction.

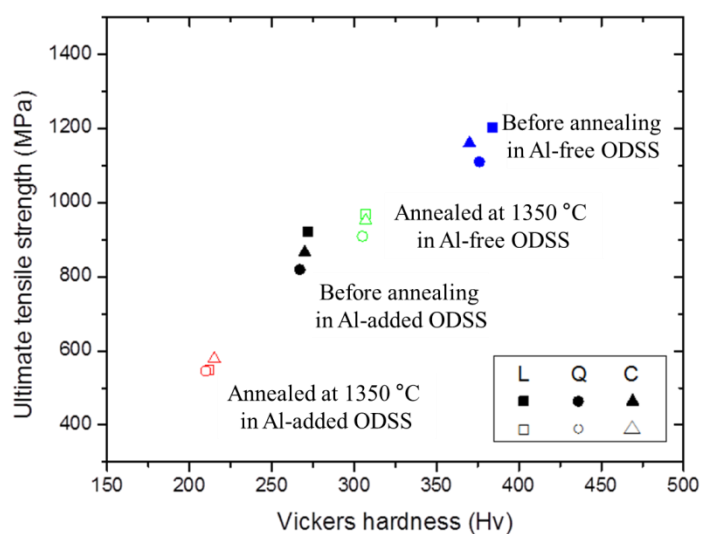


Figure 2-17 The relation between Vickers hardness and tensile strength of each direction at room temperature

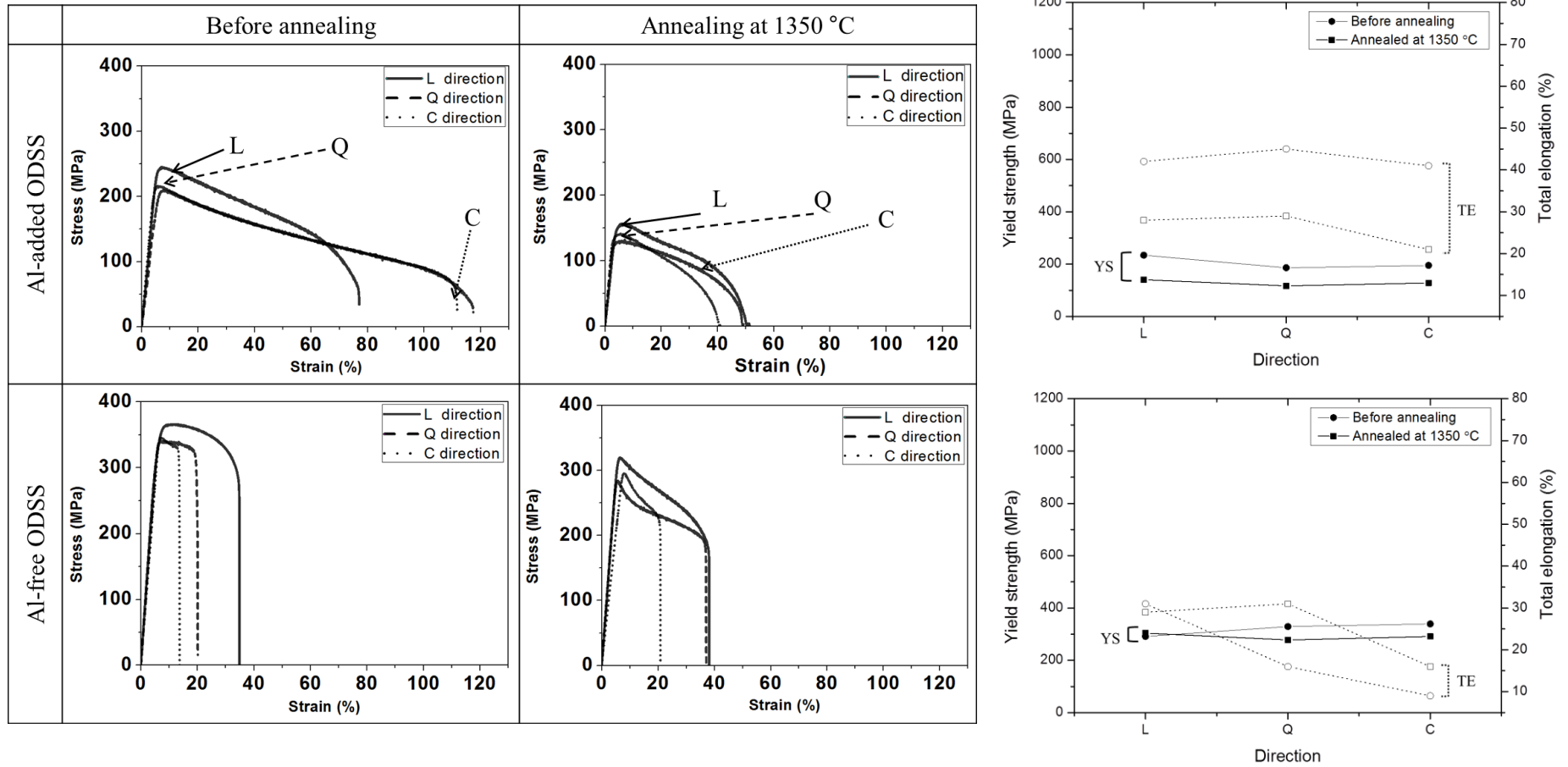


Figure 2-18 Stress-strain curves of both Al-added and Al-free ODS steel after tensile test at 700 °C

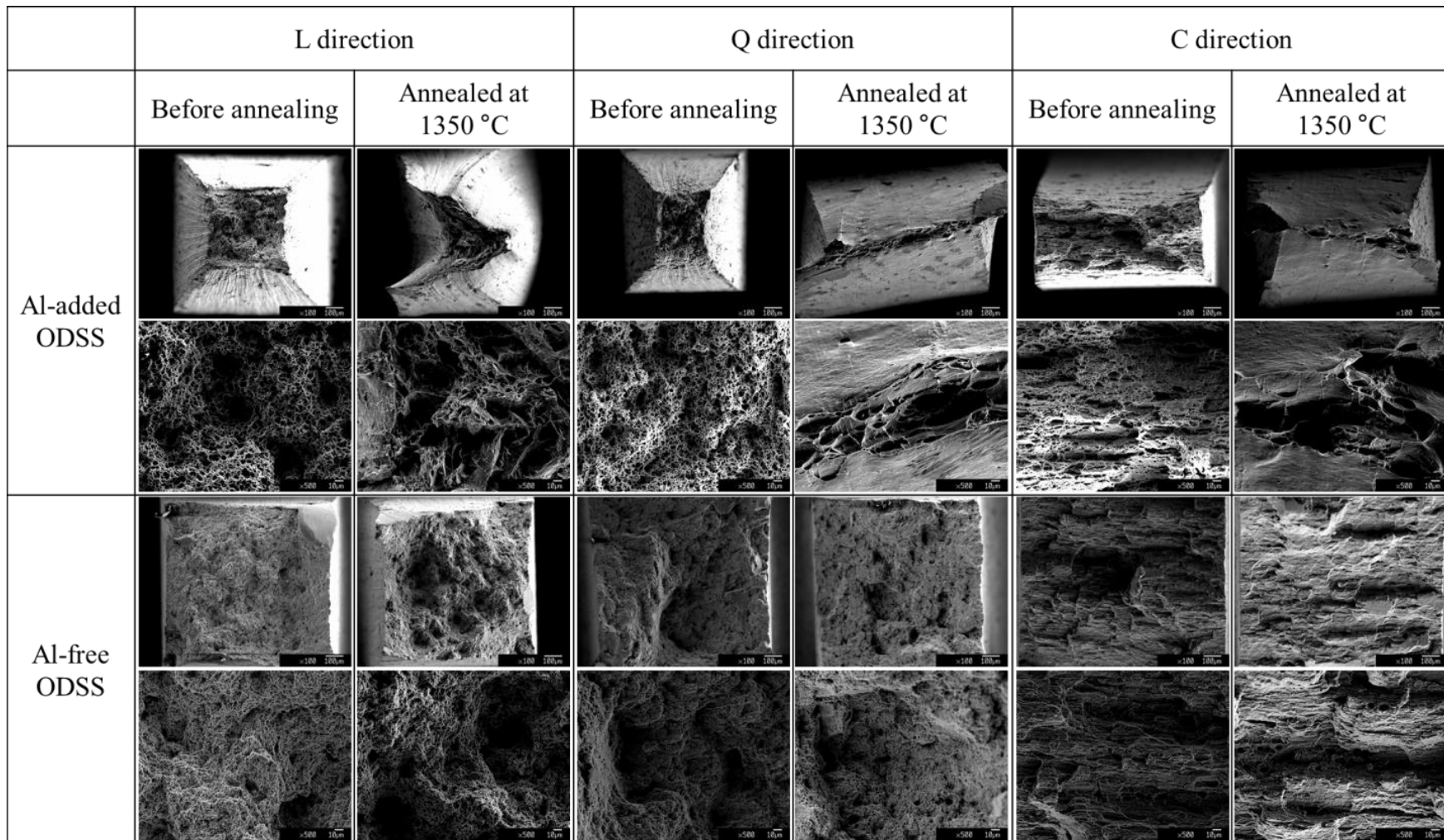


Figure 2-19 Fracture surfaces of both Al-added and Al-free ODS steel after tensile tests at 700 °C

2.3.2.3 Specimen size effect in tensile properties

Fig. 2-20 shows the summary of anisotropy in tensile properties together with the data obtained for the specimens with different specimen thickness. Black bars are tensile properties of the specimens with L direction, gray bars are the one of Q direction and white bars are of C direction, and each colored bar is of 3 different thickness of specimens. There is no significant anisotropy in the strength at (a) room temperature and (b) 700 °C, as expected from the anisotropy in grain morphology. However, the reduction of total elongation by recrystallization was affected by specimen thickness, especially when tensile tested at (d) 700 °C. In case of Al-added ODS steel, the reduction percent of total elongation in L direction is similar for both the specimens with the thickness of 1.2 mm and 0.25 mm, which can be indicated (1) - (2) = 14 % and (3) - (4) = 13 %. In contrast to this, (5) - (6) = 21 % and (7) - (8) = 32 % in C direction, which indicate that the anisotropy is more significant for the specimen of 0.25 mm thickness than that of 1.2 mm thickness. Again, the elongation of C direction with 0.25 mm specimen is lowest in all of the specimens.

Fig. 2-21 is the necking behavior observed for both the specimens with L and C direction tested at 700 °C. The blanketed numbers are corresponding to those in Fig. 2-20 (d). It can be said that the thinner specimen is the easier to deform. The fracture mode is simply described in Fig. 2-22. After recrystallization, the total grain boundary energy of coarse grains in Al-added ODS steel is decreased and furthermore it decreases with reducing the thickness of specimen. The total grain boundary area of C direction is more affected by specimen thickness than that of L direction. However, at room temperature, the anisotropy appears to be not so depending on specimen size effects. In the fabrication process for cladding tube, anisotropy can be considered for the processing, although all the specimens with different sampling direction and different thickness have total elongation above 10 % at ambient temperature. As shown in Fig. 2-21 (c), the change in the fracture behavior of Al-free ODS steel is much smaller than that of Al-added ODS steel, which suggests that the grain size is not significantly changed by annealing at 1350 °C.

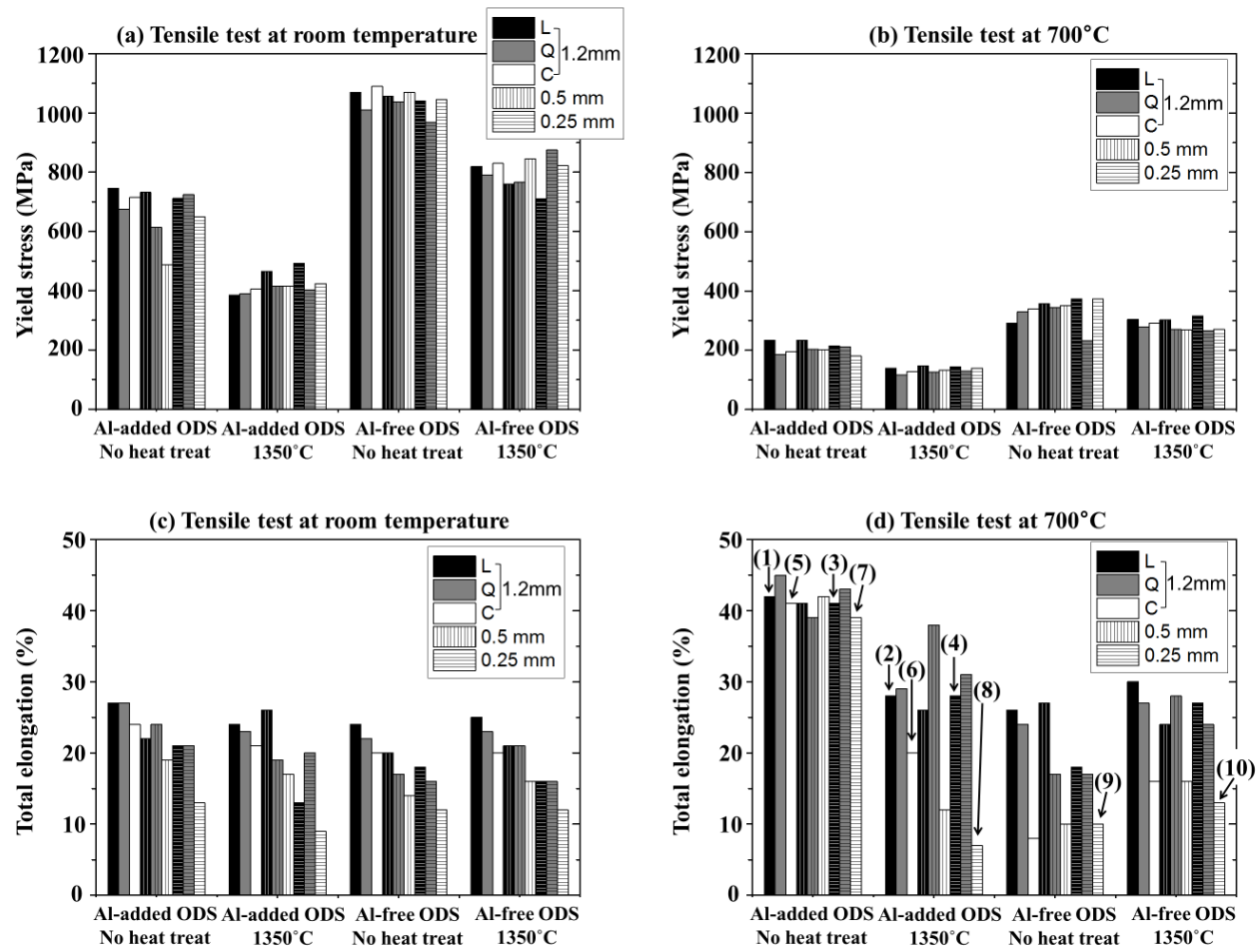


Figure 2-20 The yield stress of both ODS steels deformed at room temperature (a) and 700 °C (b), and the total elongation of both ODS steels deformed at room temperature (c) and 700 °C (d) before and after annealing

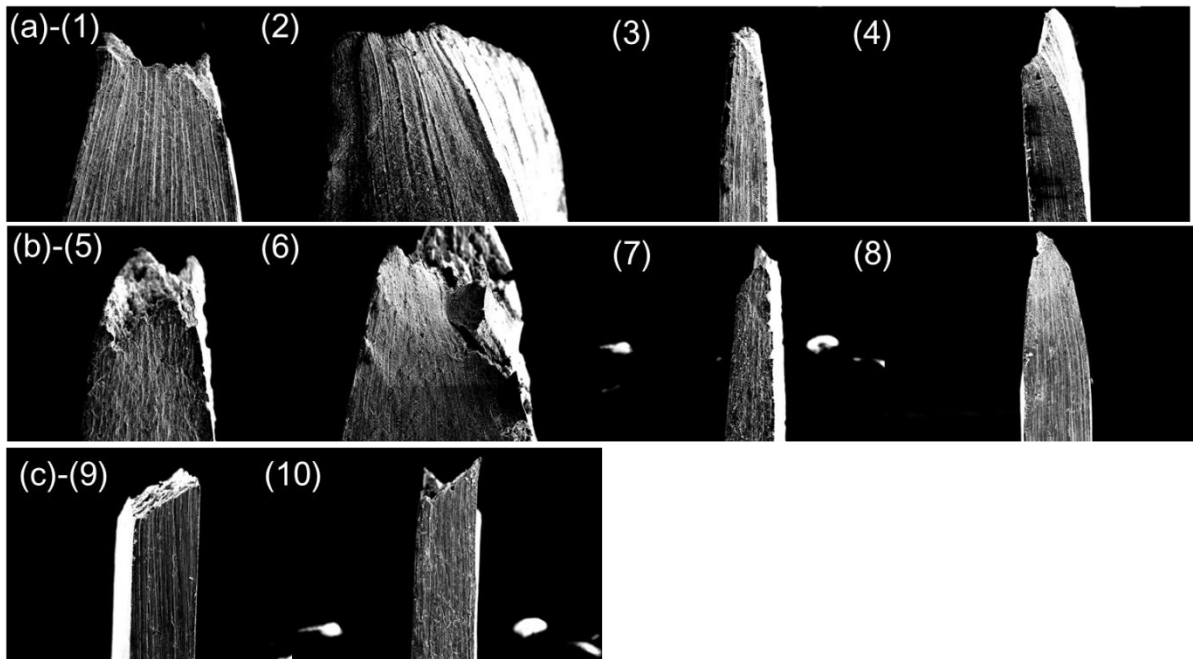


Figure 2-21 Fracture surface of Al-added ODS steel observed from specimen side surface (a) L direction (1-4), (b) C direction (5-8) and (c) Al-free ODS steel with L direction (9) and C direction (10)

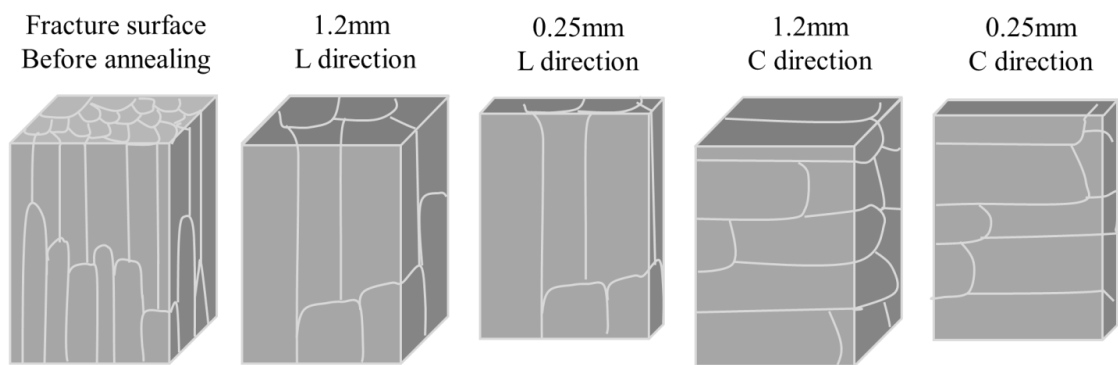


Figure 2-22 Schematic views of grain boundaries in the specimen with different thickness

2.3.3 Distribution morphologies of dispersed oxide particles

The dispersed oxide particles in the ODS steels are observed by TEM, and shown in Fig. 2-23. The oxide particles are very fine and dispersed in high number density in matrix. Therefore, it plays a role in reinforcement and improves the mechanical properties of ODS ferritic steels. In general, these oxide particles may have pinning effect on grain boundaries and retards grain boundary migration.

The size of oxide particles in Al-added ODS steel are larger than that of Al-free ODS steel before annealing. Al-free ODS steel has very fine oxide particles even after annealing at 1400 °C. Table 2-4 indicates the mean diameter and number density of oxide particles in each specimen. The mean diameter of Al-added ODS steel became larger and the number density is lower after annealing at 1350 °C. The oxide particles of Al-free ODS steel is very small and dispersed in high number density before annealing. After annealing at 1400 °C, the particle size and number density become similar with Al-added ODS steel but before annealing. It is considered that the ultra-fine oxide particles are formed at around 1250 °C as Y-Ti-O that is necessary to obtain high strength at elevated temperatures. Those fine oxide particles restrain recrystallization by pinning grain boundaries in ODS steel, so it interrupts the grain boundary migration effectively and caused retardation of recrystallization. The oxide particles are highly thermo-dynamically stable so that they still remain at high number density and small particle size even after annealing at 1400 °C as shown Fig. 2-23 (d).

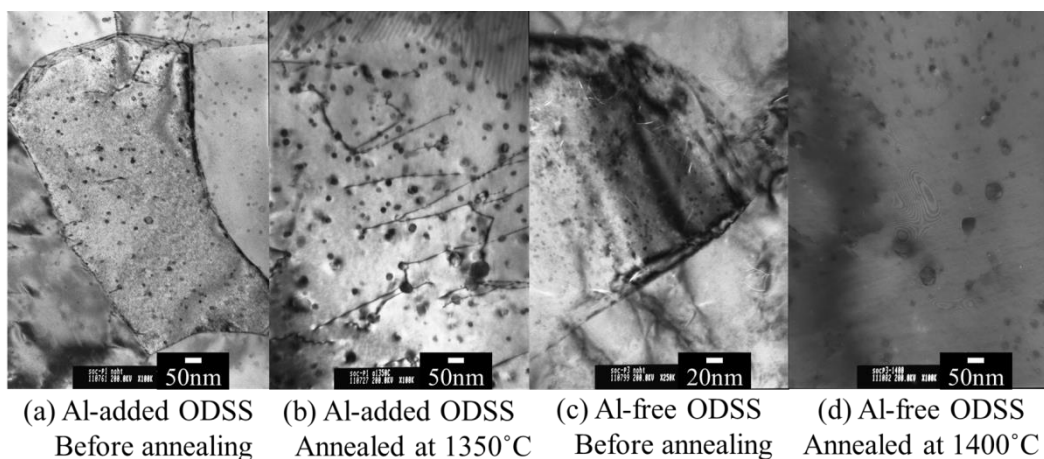


Figure 2-23 Effects of annealing on the dispersion morphology of oxide particles in the Al-added and Al-free ODS steels

In Al-added ODS steel, however, rather large oxide particles are preferentially formed as Al-Y-O instead of Y-Ti-O. These Al-Y-O particles are much larger than that of Y-Ti-O particles, which results in lower strength than the Al-free ODS steels in our previous work [27]. It was found that the simultaneous addition of Zr and Ti made oxide particles to be fine in Al-added ODS steels. However, single atom addition of Zr is not effective to reduce the size of oxide particles.

A large size and small number density of oxide particles are not effective to pin the grain boundaries. It is expected that the grain boundaries are easy to migrate in the existence of coarse oxide particles, which results in the easier occurrence of recrystallization than Al-free ODS steel. Also, it is assumed that secondary recrystallization by Ostwald ripening occurred in Al-added ODS steel at elevated temperatures such as 1350 °C.

Table 2-4 Distributions of oxide particles before and after annealing

	Al-added ODSS		Al-free ODSS	
	Before annealing	Annealed at 1350 °C	Before annealing	Annealed at 1400 °C
Mean diameter	11 nm	23 nm	4 nm	19 nm
Number density	$8.4 \times 10^{21} \text{ m}^{-3}$	$1.9 \times 10^{21} \text{ m}^{-3}$	$5.4 \times 10^{22} \text{ m}^{-3}$	$2.3 \times 10^{21} \text{ m}^{-3}$

2.4 Summary

In this research, the recrystallization behavior of 15Cr-ODS ferritic steels with and without Al addition is investigated with focusing on the correlation between microstructure and mechanical properties in comparison to SUS430 which contains 16 wt.% Cr. The effect of recrystallization on the anisotropy and the specimen size effect on mechanical properties are also investigated for these two ODS steels. The results obtained are summarized as follows;

- 1) The microstructure and Vickers hardness of as-received SUS 430 is not changed until around 850 °C, meanwhile 40% cold rolled SUS 430 is recrystallized at above 700 °C. Both of the SUS 430 have new fine microstructure when they are annealed at above 850 °C, and Vickers hardness is increased. This is due to the small amount of phase transformation from γ to α or even α' during cooling from annealing temperature.
- 2) The Vickers hardness and tensile strength is reduced after recrystallization. The yield stress of Al-added ODS steel is considerably reduced by the recrystallization at 1350 °C, while Al-free ODS steel is not fully recrystallized even after the annealing up to 1400 °C, and the reduction of the yield stress is small. The result of tensile test at 700 °C also shows the reduction of the yield stress, which is almost same as the results at room temperature.
- 3) The deformation texture is still observed in both ODS steels even after recrystallization. The anisotropy in the tensile properties at room temperature was not influenced by recrystallization, although the tensile strength at 700 °C indicated some anisotropy in both Al-added and Al-free ODS steel. The total elongation tested at 700 °C is reduced by annealing, and it becomes significant in the specimen with C direction. It is suggested that the total grain boundary area is more reduced in the C direction. Since the grain morphology of Al-free ODS steel is not changed by annealing, the anisotropy also is unaffected by annealing.
- 4) Anisotropy of tensile elongation is more obvious with decreasing the thickness of specimen.
- 5) The Al addition reduces recrystallization temperature caused by lowering pinning effect through the change in the oxide particles from Y-Ti-O to Y-Al-O.

References

1. P. He, R. Lindau, A. Moeslang, H.R.Z. Sandim, "The influence of thermomechanical processing on the microstructure and mechanical properties of 13.5Cr ODS steels", *Fusion Eng. Des.*, **8** (2013) 2448-2452
2. S. Ohtsuka, S. Ukai, M. Fujiwara, T. Kaito, T. Narita, "Nano-structure control in ODS martensitic steels by means of selecting titanium and oxygen contents", *J. Phys. Chem. Solids.*, **66** (2005) 571-575
3. Takeshi Narita , Shigeharu Ukai , Bin Leng , Satoshi Ohtsuka, Takeji Kaito, "Characterization of recrystallization of 12Cr and 15Cr ODS ferritic steels", *J. nucl. Sci. Technol.*, **50** (2013) 314-320
4. Bin LENG, Shigeharu UKAI, Yoshito SUGINO, Qingxin TANG, Takeshi NARITA, Shigenari HAYASHI, Farong WAN, Satoshi OHTSUKA, Takeji KAITO, "Recrystallization Texture of Cold-rolled Oxide Dispersion Strengthened Ferritic Steel", *ISIJ international* **51** (2011) 951-957
5. H.K.D.H. Bhadeshia, "Recrystallisation of practical mechanically alloyed iron-base and nickel-base superalloys", *Mater. Sci. Eng. A* **223** (1997) 64-77
6. Sanghoon Noh, Doctor's thesis, *Kyoto University* (2011)
7. Shigeharu UKAI, "Development of ODS Ferritic-Martensitic Steels for Fast Reactor Fuel Cladding", *サイクル機構技*, **7** (2000) 83-91
8. R. Kasada, S.G. Lee, J.H. Lee, T. Omura, C.H. Zhang, P. Dou, J. Isselin, A. Kimura, M. Inoue, S. Ukai, S. Ohnuki, T. Fujisawa, T. Okuda, F. Abe, "Super ODS Steels R&D for Fuel Cladding of Next Generation Nuclear Systems 5) Mechanical properties and microstructure", *Proc. Int. Cong. Advances in Nuclear Power Plants, (ICAPP-2009)*, (2009) 9072
9. Jerome Isselin, Ryuta Kasada, Akihiko Kimura, Takanari Okuda, Masaki Inoue, Shigeharu Ukai, Somei Ohnuki, Toshiharu Fujisawa, Fujio Abe, "Effects of Zr Addition on the Microstructure of 14%Cr4%Al ODS Ferritic Steels", *Mater. Trans.*, **51** (2010) 1011-1015
10. R. Gao, T. Zhang, X.P. Wang, Q.F. Fang, C.S. Liu, "Effect of zirconium addition on the microstructure and mechanical properties of ODS ferritic steels containing aluminum", *J. Nucl. Mater.*, **444** (2014) 462-468
11. S.H. Noh, B.J. Kim, R. Kasada and A. Kimura, "Diffusion bonding between ODS ferritic steel and F82H steel for fusion applications", *J. Nucl. Mater.*, **426** (2012) 208-213

12. Yoosung HA, Noriyuki IWATA, Akihiko KIMURA, "Effect of Al on the recrystallization behavior of 15Cr-oxide dispersion strengthened ferritic steel", *Proc. Int. Cong. Advances in Nuclear Power Plants, (ICAPP-2013)* (2013) FA017
13. L. Colombier and J. Hochmann, "Stainless and Heat Resisting Steels", *Edward Arnold* (1967)
14. T. Sourmail, "Precipitation in creep resistant austenitic stainless steels", *Materi. Sci. Techn.*, **17** (2001) 1-14
15. M Shimada, H Kokawa, Z.J Wang, Y.S Sato, I Karibe, "Optimization of grain boundary character distribution for intergranular corrosion resistant 304 stainless steel by twin-induced grain boundary engineering", *Acta Mater.*, **50** (2002) 2331-2341
16. D.N Wasnik, V Kain, I Samajdar, B Verlinden, P.K De, "Resistance to sensitization and intergranular corrosion through extreme randomization of grain boundaries", *Acta Mater.*, **50** (2002) 4587-4601
17. http://www.calphad.com/martensitic_stainless_steel_for_knives_part_1.html
18. Hirokazu OKADA, Shigeharu UKAI, Masaki INOUE, "Effects of Grain Morphology and Texture on High Temperature Deformation in Oxide Dispersion Strengthened Ferritic Steels", *J. nucl. Sci. Technol.*, **33** (1996) 936-943
19. Yoshito Sugino, Shigeharu Ukai, Shigenari Hayashi, Qingxin Tang, Bin Leng, "Directional recrystallization of ODS alloys by means of zone annealing", *J. Nucl. Mater.*, **417** (2011) 171-175
20. Shigeharu UKAI, Shunji MIZUTA, Masayuki FUJIWARA, Takanari OKUDA, Toshimi KOBAYASHI, "Development of 9Cr-ODS Martensitic Steel Claddings for Fuel Pins by means of Ferrite to Austenite Phase Transformation", *J. nucl. Sci. Technol.*, **39** (2002) 778-788
21. TERRY C. TOTEMEIER, THOMAS M. LILLO, "Effect of Orientation on the Tensile and Creep Properties of Coarse-Grained INCONEL Alloy MA754", *Metall. Mater. Trans. A*, **36** (2005) 785-795
22. J.J. Nah, H.G. Kang, M.Y. Huh, O. Engler, "Effect of strain states during cold rolling on the recrystallized grain size in an aluminum alloy", *Scripta Mater.*, **58** (2008) 500-503
23. T.S. CHOU, H.K.D.H. BHADESHIA, "Crystallographic Texture in Mechanically Alloyed Oxide Dispersion-Strengthened MA956 and MA957 Steels", *Metall. Mater. Trans. A*, **24** (1993) 773-779
24. C. Capdevila, M.K. Miller, G. Pimentel, J. Chao, "Influence of recrystallization on phase separation kinetics of oxide dispersion strengthened Fe–Cr–Al alloy", *Scripta Mater.*, **66** (2012) 254-257

25. H. M. CHAN, F. J. HUMPHREYS, "THE RECRYSTALLISATION OF ALUMINIUM-SILICON ALLOYS CONTAINING A BIMODAL PARTICLE DISTRIBUTION", *Acta Mater.*, **32** (1984) 235-243
26. G. Ghosh, G.B. Olson, "The isotropic shear modulus of multicomponent Fe-base solid solutions", *Acta Mater.*, **50** (2002) 2655-2675
27. R. Kasada, N. Toda, K. Yutani, H.S. Cho, H. Kishimoto, A. Kimura, "Pre- and post-deformation microstructures of oxide dispersion strengthened ferritic steels", *J. Nucl. Mater.*, 367-370 (2007) 222-228

Notice

Some portion of the work originally appeared in the Proceedings of the 8th Pacific Rim International Conference on Advanced Materials and Processing (PRICM-8), Copyright 2013 by The Minerals, Metals & Materials Society. It is reprinted with permission of The Minerals, Metals & Materials Society.

Chapter 3

Effect of Cold Rolling on Recrystallization Behavior

3.1 Introduction

Understanding recrystallization behavior is important for ODS ferritic steels to apply for cladding material for GEN IV systems and also first wall structural material for fusion blanket.

As shown in Chapter 2, recrystallization of ODS steel is harder than a conventional ferritic steel caused by the existence of oxide particles as obstacle for grain boundary migration as well as dislocation motion. There are several factors determining recrystallization behavior such as cold rolling, annealing method and chemical compositions. Since amount of strain may control strain energy that accelerates recrystallization [1-4], it is considered that the cold rolling process may affect the following recrystallization behavior. Therefore it is expected that cold rolling process assists recrystallization for ODS steels. In this research, effect of cold rolling on recrystallization behavior of ODS ferritic steel is investigated as follows:

- 1) For comparison, the recrystallization behavior of the ODS steel produced by hot isostatic processing of the laboratory scale is investigated together with that of cold rolled ODS steel.
- 2) Cold rolling with different reduction ratio is carried out in two directions according to the extrusion direction (ED); one is RD, which is cold rolled along with the extrusion direction and another is cold rolled in the direction perpendicular to the extrusion direction, called TD.

3.2 Experimental procedure

3.2.1 Hot isostatic processing

ODS steels are usually consolidated by hot extrusion processing or hot isostatic processing after mechanical alloying, and the grain morphology and microstructure are different between the products fabricated by each fabrication processing. Therefore, HIPed ODS ferritic steel, which contains Al, is prepared to examine the grain morphology change by fabrication processing conditions.

The Al-free ODS steel composed of Fe (bal.)-15Cr-0.1Ti-0.35Y₂O₃ is used in this study. The mechanically alloyed powders are sintered in hot press, as shown in Fig. 3-1 (a) using a hot press machine. The heating conditions were programmed as shown in Fig. 3-1 (b). The powders in a graphite sleeve were firstly degassed at 400 °C for 2 hours then heated up to 1150 °C for holding for 2 hours at a pressure of 60 MPa and followed by furnace cooling [5]. After hot isostatic processing, the material was annealed in the hot press machine. Also, 40 % cold rolled specimen is prepared.

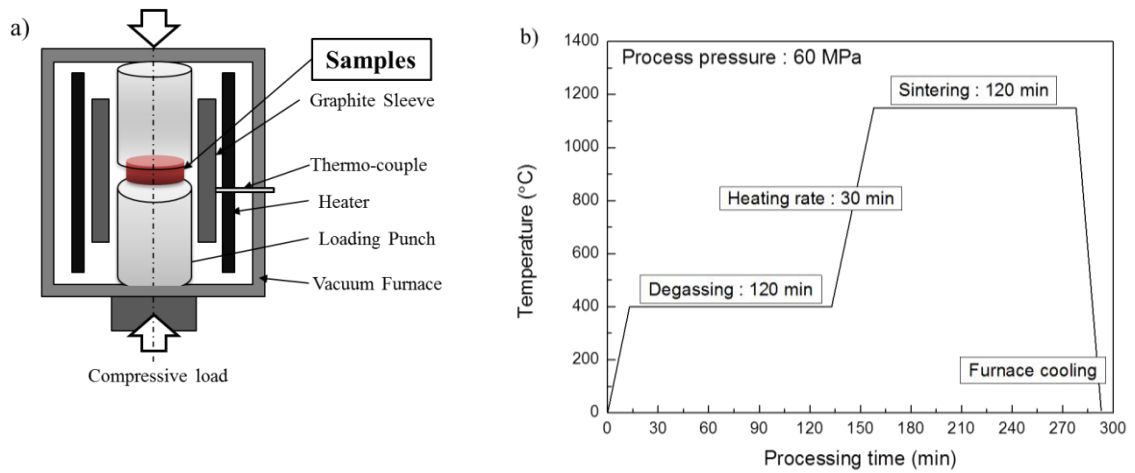


Figure 3-1 Hot isostatic processing of ODS ferritic steel;

(a) schematic view of hot press, and (b) heating up and pressure diagram

3.2.2 Cold rolling processing

Al-added and Al-free ODS ferritic steels are used for cold rolling processing after hot extrusion, of which the chemical compositions are same as Table 2-1.

The specimens of both the steels, which measure 10 mm (w) x 10 mm (l) x 1 mm (t), were cold rolled in the extrusion direction, which is named as RD direction (Fig. 3-2 (a)). The reduction ratio of specimen thickness was 20 %, 40 % and 80 % for both ODS steels, and each specimen was subjected to isothermal annealing in a vacuum at temperatures from 850 °C to 1400 °C with 50 °C steps for 1 hour. Heating rate for the annealing was 30 °C/min and the specimens were cooled in the furnace. All annealing process is performed by using hot press machine. To investigate the effects of cold rolling direction, another cold rolling was performed in the direction that the rolling direction is perpendicular to the extrusion direction, and called TD, with only 40 % of reduction ratio (Fig. 3-2 (b)). Tube manufacturing is practically conducted by repeating a set of cold rolling-annealing processing [6-9]. As shown in Fig. 3-3, the 40 % cold rolled Al-added and Al-free ODS steels were annealed at just below recrystallization temperature. And then, second cold rolling with 40 % reduction ratio was performed following second annealing at temperatures between 850 °C and 1400 °C.

3.2.3 Micro Vickers hardness test

Hardness measurements were performed after isothermal annealing. The surface of the specimen was mechanically grinded with emery SiC papers until #4000, and buff-polished with a diamond paste of 6 μm diameter. Micro-Vickers hardness tests for each cold rolling sample before and after annealing were carried out with a load of 1 kgf for 10 seconds.

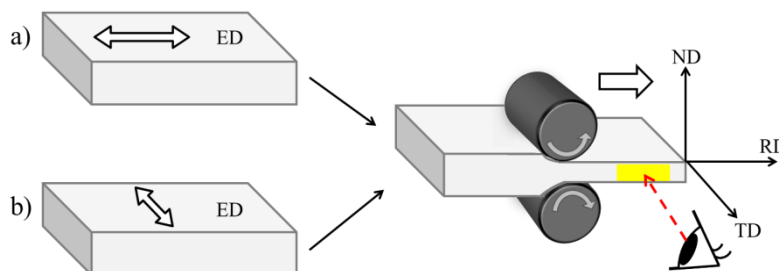


Figure 3-2 Schematic view of cold rolling direction along with extrusion direction

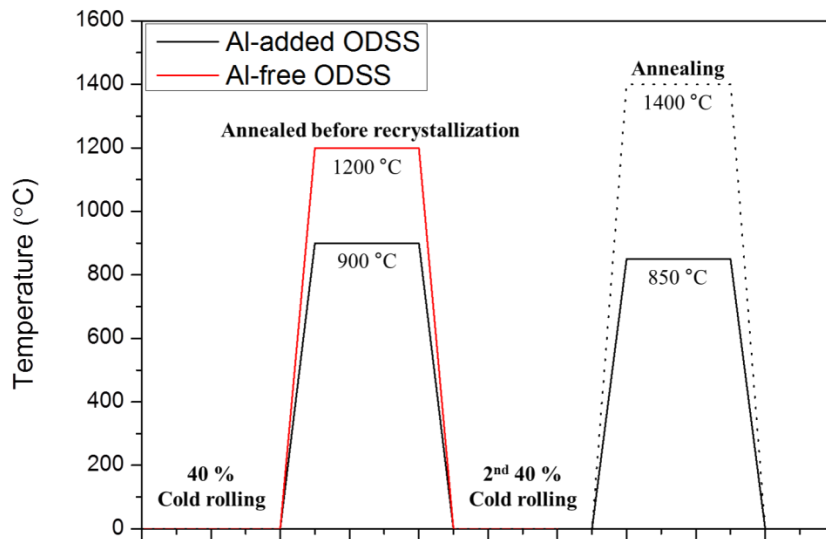


Figure 3-3 A series of cold rolling and annealing processing

3.2.4 Microstructure observation

The annealed samples were mechanically grinded with #800, #1200, #2400 and #4000 emery SiC papers. And then they were buff-polished with diamond paste of 6, 3, 1, 0.25 μm diameter. Finally, colloidal silica polishing with 0.04 μm diameter was performed. The grain morphology was observed by FE-SEM installed in FE-EPMA. EBSD analysis was carried out to obtain crystallographic information.

The specimens for TEM observation were sampled from the plates with each cold rolling ratio after recrystallization treatment of Al-added and Al-free ODS steels by focused ion beam (FIB) technique using JFIB-2100 and FB-2200. Thin foil samples, which measure $5 \times 10 \times 0.1 \text{ m}^3$, were prepared by Ga-ion bombardment and put on a Cu mesh. The surface damage layer induced by ion bombardment was removed by a gentle milling apparatus [10].

The effect of annealing on the oxide particle distribution morphology was examined by TEM (JEM-2010, JEOL co., Japan) with an acceleration voltage of 200 kV. All the micrographs were observed from the TD direction shown in Fig. 3-2.

3.3 Results and discussions

3.3.1 Annealing effect on HIPed 15Cr ODS ferritic steel

3.3.1.1 Hardness change by annealing

The Vickers hardness change by isothermal annealing is shown in Fig.3-4 for the HIPed 15Cr-ODS ferritic steels with and without cold rolling. Both as-received and 40 % cold rolled HIPed ODS steels have lower Vickers hardness than those of extruded ODS steels (compared with Al-free ODS steel in Fig. 2-13). In as-received material, the Vickers hardness is reduced with increasing annealing temperature without any dramatic changes but showing a drop in the hardness between 1250 °C and 1300 °C. In case of 40 % cold rolled specimen, the hardness is also gradually reduced with increasing annealing temperature, and there is also a drop in the hardness between 1150 °C and 1200 °C.

The hardness of 40 % cold rolled specimen is a little higher than that of as-received specimen after annealing below 1150 °C because of a higher dislocation density by cold rolling. After annealing at 1150 °C, the hardness of 40 % cold rolled specimen is lower than that of as-received specimen. It is suggested that the recrystallization of cold rolled specimen occurs at around 1150 °C where the hardness decreases. The high internal stress built by cold rolling acts as driving force for recrystallization, consequently the cold rolled specimen can be recrystallized at lower temperatures than as-received specimens.

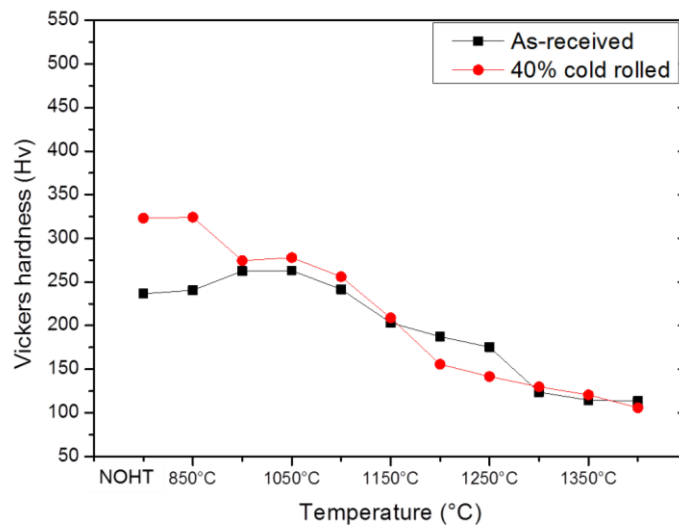


Figure 3-4 Vickers hardness of as-received and 40% cold rolled HIPed ODS steel

3.3.1.2 Microstructure change by annealing

The EBSD grain morphology before annealing is shown in Fig. 3-5 before annealing. As-received specimen doesn't have anisotropy and equiaxed grains are randomly distributed. The grain size is 7.4 μm , which is larger than that of extruded ODS steel (compare with Fig. 2-10). 40 % cold rolled specimen was deformed along with the cold rolling direction, grains are also shapely elongated along with the rolling direction. Many grains are oriented as the surface normal is a $\langle 110 \rangle$ orientation.

Fig. 3-6 shows the grain morphology after annealing at several temperatures observed by SEM. Before annealing, many pores exist on the specimen surface (high magnification picture in as-received specimen before annealing), of which the number density is much larger than that of the extruded ODS steels. This difference is considered to be due to the difference in the processing after consolidation: no processing in HIPed ODS steel but normalizing annealing at 1050 $^{\circ}\text{C}$ in a vacuum in extruded ODS steel. Thus, pores are more formed and sintering density is relatively lower in the HIPed ODS steel than hot extruded ODS steel. The initial grain size of HIPed ODS steel is also bigger than that of extruded ODS steel, which is reflected on the hardness reduction in the HIPed ODS steel. P. Unifantowicz et. al [9] reported that a HIPed ODS steel had twice larger number density of micro-pores and the grain size was bigger than that of hot extruded ODS steel. The tensile strength and Vickers hardness of hot extruded ODS steel at room temperature is remarkably higher than that of the HIPed ODS steel, which agreed with the result of this research. It should to consider that the dispersed oxide particles also affect the mechanical properties as different fabrication processing. Although the mechanical properties are different as fabrication processing, grain morphologies including anisotropy and recrystallization behavior with cold rolling are more focused in this study.

In as-received specimen as shown in Fig. 3-6, the grain morphology is not remarkably changed until annealing at 1200 $^{\circ}\text{C}$ and the recrystallization partially occurs at around 1250 $^{\circ}\text{C}$. Finally, the recrystallization is completed at above 1300 $^{\circ}\text{C}$, also the grain shape is isotropic. It is expected that recrystallization and grain growth resulted in the reduction of the Vickers hardness at above 1250 $^{\circ}\text{C}$ as is shown in Fig. 3-4. In case of 40 % cold rolled specimen, the recovery and recrystallization behavior competitively occurs from the annealing temperature of 1100 $^{\circ}\text{C}$, where hardness is gradually decreased, and almost a half of grains changes their size after annealing above 1150 $^{\circ}\text{C}$. Finally, all the grains are recrystallized at around 1200 $^{\circ}\text{C}$. It is noticed that recrystallization results in the disappearance of anisotropy. The effect of cold rolling process on grain morphology disappears

after recrystallization. In other words, grains are returned to original morphology, which is almost same with that before the cold rolling. The recrystallization temperature is at around 1300 °C of as-received specimen and 1200 °C of 40 % cold rolled specimen, respectively. Since the plastic deformation by cold rolling induces the internal stress and retained dislocations are rearranged or eliminated during annealing, the internal energy of material is reduced and there is a thermo-dynamic driving force for recrystallization, the high angle over 10~15 ° misorientation is migrated [11-13]. The high dislocation density induced by cold rolling accelerates recrystallizing at lower temperature.

Grains are coarse after recrystallization both as-received and 40 % cold rolled specimen and the Vickers hardness is also reduced as increasing annealing temperature. The grains of 40 % cold rolled specimen become particularly coarse after annealing at 1400 °C.

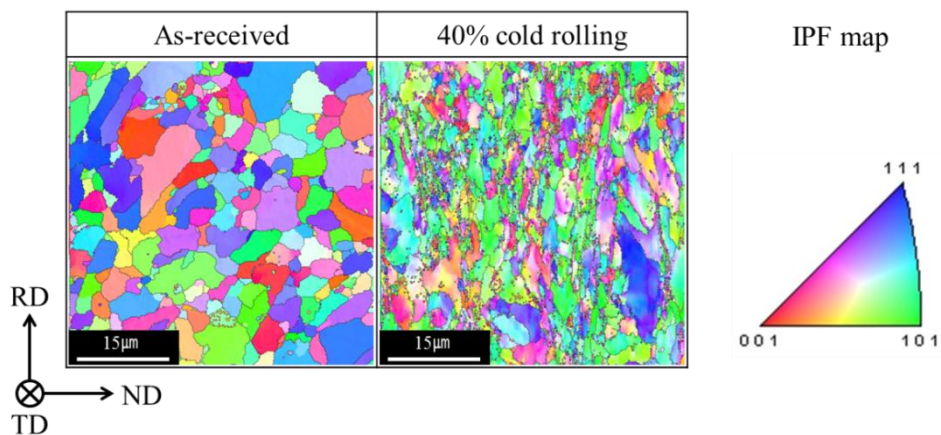


Figure 3-5 Grain orientation map of as-received and 40 % cold rolled HIPed ODS steel before annealing

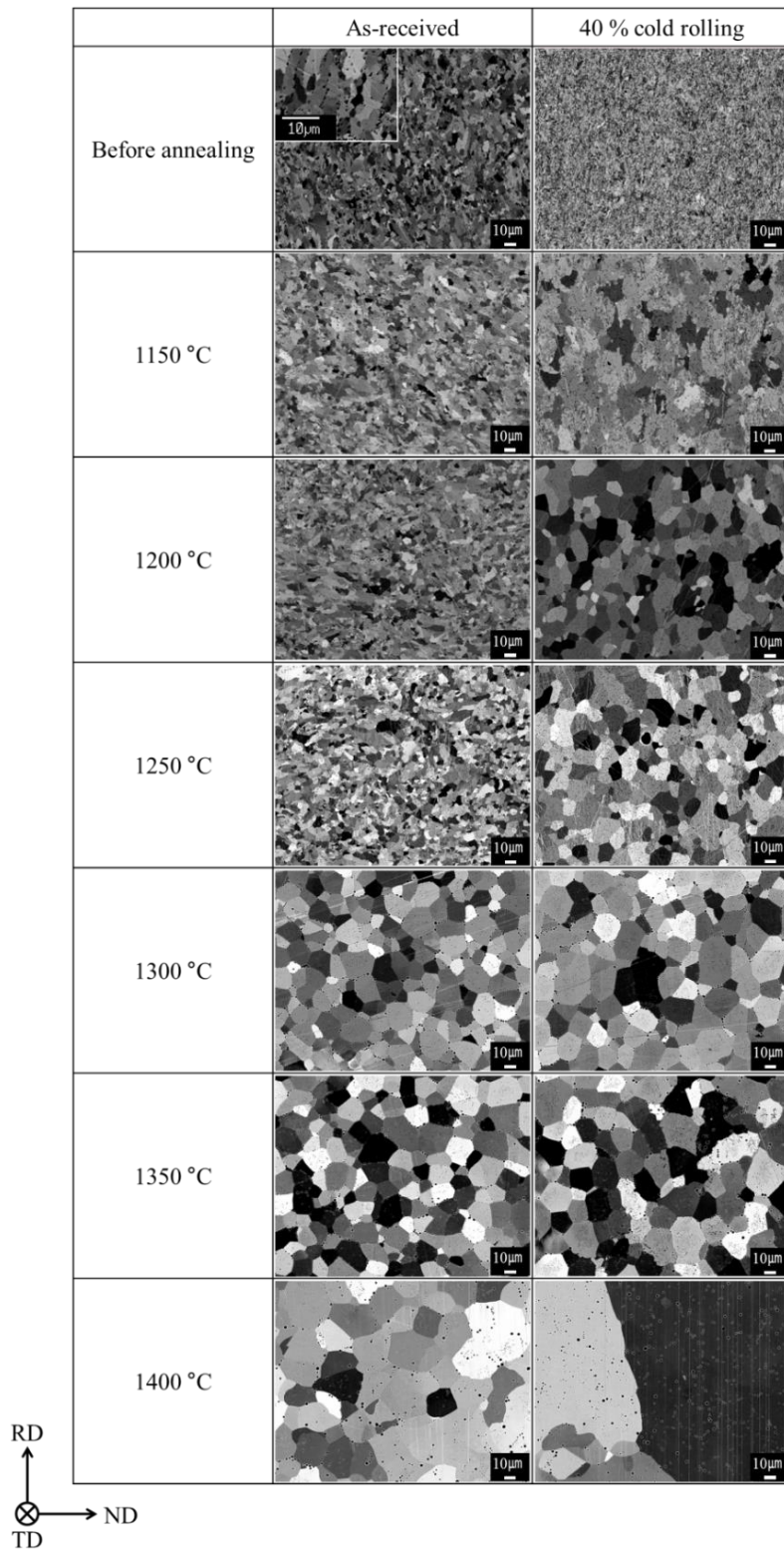


Figure 3-6 Grain morphology of as-received and 40 % cold rolled HIPed ODS steel after annealing at each temperature

3.3.2 Annealing effect on extruded 15Cr ODS ferritic steel

3.3.2.1 The hardness change by annealing

Effect of cold rolling ratio on Vickers hardness after isothermal annealing both Al-added and Al-free ODS steel fabricated by hot extrusion is shown in Fig. 3-7, where the Vickers hardness is reduced as increasing annealing temperature both the steels. The hardness of Al-free ODS steel is still higher than that of Al-added ODS steel, except 80 % cold rolled specimen after annealed at above 1300 °C.

Before annealing, hardness is highest in 80 % cold rolled specimen, as expected, caused by inducing dislocations with the highest density. The hardness is abruptly decreased with increasing annealing temperature which decreases with increasing in the reduction ratio of cold rolling. It is considered that the reduction of hardness is due to annealing out of dislocations.

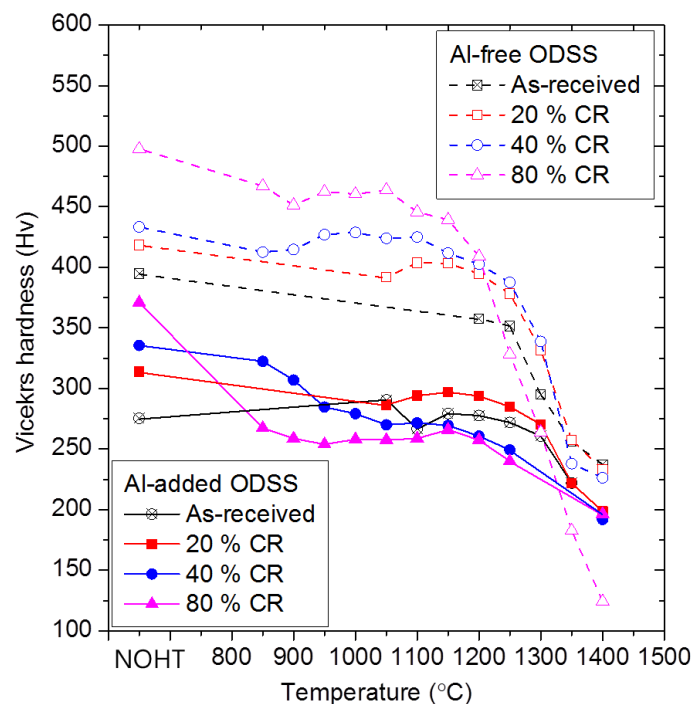


Figure 3-7 Vickers hardness of Al-added and Al-free ODSS with different cold rolling ratio

In case of Al-added ODS steel, the hardness of 20 % cold rolled specimen is reduced at around 1350 °C, which is similar with as-received specimen (in Chapter 2). The annealing temperature showing a considerable reduction of hardness is at around 950 °C in 40 % cold rolled specimen and

850 °C in 80 % cold rolled specimen, respectively. In comparison to Al-added ODS steel, it is similar that the hardness reduction starts at a lower annealing temperature but the temperature is higher in Al-free-ODS steel. The hardness of 40 % and 80 % cold rolled specimen are significantly decreased at around 1300 °C and 1250 °C, respectively.

3.3.2.2 Grain morphology change by annealing

Fig. 3-8 shows the examples of grain morphology change by annealing at different temperatures for both the ODS steels with different cold rolling ratio. These grain morphologies are those after annealing at each temperature where the Vickers hardness considerably decreased. The grain size of the specimens depends on annealing temperature, cold rolling ratio and Al content of the ODS steel.

The grain morphology of Al-added ODS steel was easily changed after annealing. The microstructure observation revealed that the recrystallization occurred in all the specimens shown in the figure. The grain size of 20 % cold rolled specimen is significantly increased after annealing at 1350 °C, and 40 % cold rolled specimen has smaller grains than that of 20 % cold rolled one because of a lower annealing temperature of 950 °C. The Al-added steel with 80 % cold rolling shows the smallest grains of recrystallization after annealing at 850 °C, of which the Vickers hardness is abruptly reduced by the annealing. It is considered that the reduction of the hardness is due to not only the recovery of dislocations but also recrystallization, namely, grain coarsening. Grain growth becomes more significant with increasing annealing temperature and decreasing cold rolling ratio.

The recrystallization behavior of Al-free ODS steel is considerably different from that of Al-added ODS steel. The 20 % cold rolled Al-free ODS steel never shows recrystallization or grain growth after the annealing at 1350 °C, although the hardness is remarkably decreased at each annealing temperature. The grain morphology is similar to the case of the annealing at 1300 °C after 40 % cold rolling. Therefore, not recrystallization but recovery induced the softening. The 80 % cold rolled specimen of Al-free ODS steel recrystallizes at above 1250 °C. It is confirmed that Al-free ODS steel is still hardly recrystallized after cold rolling processing.

At moderate high temperatures, the recovery occurs easily and free dislocations will promptly rearrange themselves into low-angle grain boundaries. The driving force is the difference in energy

between the deformed and recrystallized state, ΔE per unit volume, which can be determined by the dislocation density or the sub-grain size and surface energy [14].

$$\Delta E \approx \rho G b^2 \approx 3 \gamma_s / d_s \quad (3.1)$$

where ρ is the dislocation density, G is the shear modulus, b is the Burgers vector of the dislocations. γ is the sub-grain boundary energy and d_s is the sub-grain size.

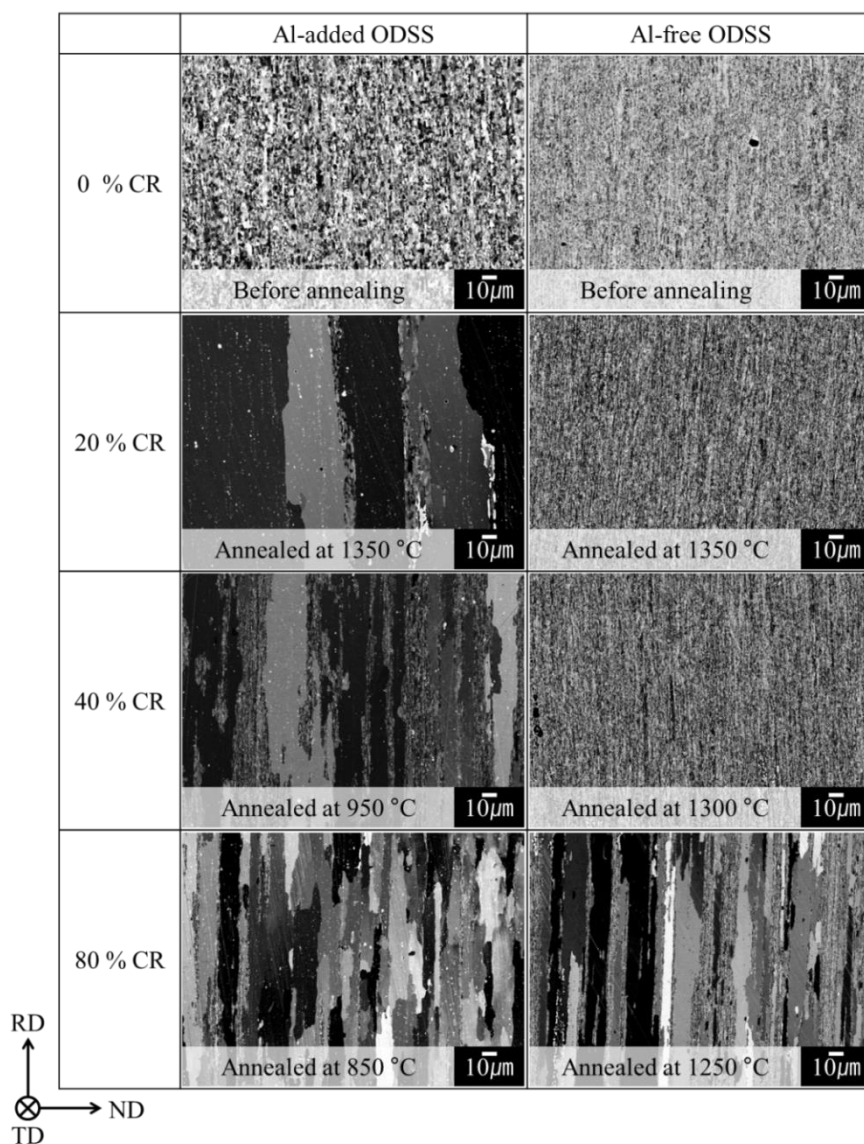


Figure 3-8 Grain morphology of Al-added and Al-free ODS steel after annealing

Because the internal stress is too small to recrystallize at low cold rolling ratio, the annealing at higher temperature up to 1350 °C is required for grain growth along with the strong texture of extruded ODS steels. With increasing cold rolling ratio, the stored energy is increased and recrystallization was accelerated. 80 % cold rolling makes recrystallization occur at lower temperature.

Deformation texture was examined by EBSD analysis and pole figures are shown in Fig. 3-9 before and after annealing at each temperature. Before annealing, all the pole figures indicate that the $\langle 110 \rangle$ deformation texture developed along with the extrusion direction denoted as RD. The grain orientations are allocated on the edge of stereo triangle connecting $\langle 001 \rangle$ and $\langle 111 \rangle$, which enables to define the texture as $\{112\} \langle 110 \rangle$ orientation. The grains are elongated parallel to the extrusion direction (ED) that is also the cold rolling direction in this case. As increasing the cold rolling reduction ratio, the more dense RD fiber is formed in both Al-added and Al-free ODS steels. After annealing, the pole figure changes in accordance with the annealing temperature and cold rolling ratio.

The pole figure of 20 % cold rolled Al-added ODS steel after the annealing at 1350 °C indicates almost no texture in the extrusion direction, which agrees with the well-grown grains in Fig. 3-8. The orientation is $\{110\} \langle 100 \rangle$, coarse Goss orientation in secondary recrystallization, it is same with 0 % cold rolling after recrystallization texture. In the 80 % cold rolled Al-added ODS steel, it is also shown that recrystallization relieves the strong deformation texture along with the extrusion direction. Furthermore, the grain orientations appear to change from $\{112\}$ to $\{110\}$, $\{112\}$ and $\{113\}$ texture is increasing with high reduction ratio. But it is not secondary recrystallization texture.

The Al-free ODS steel with 20 % and 40 % cold rolling show no change in the pole figure after the annealing, while 80 % cold rolled specimen shows a change in the pole figure showing rather random deformation structure. This trend reflects the change in the grain morphology from very fine grains to coarsened and elongated grains as shown in Fig. 3-8.

As for the effect of Al addition on the recrystallization behavior of the ODS steel, all the experimental results indicate that the recrystallization of 15Cr-ODS ferritic steel is enhanced by the addition of Al, as result of Chapter 2.

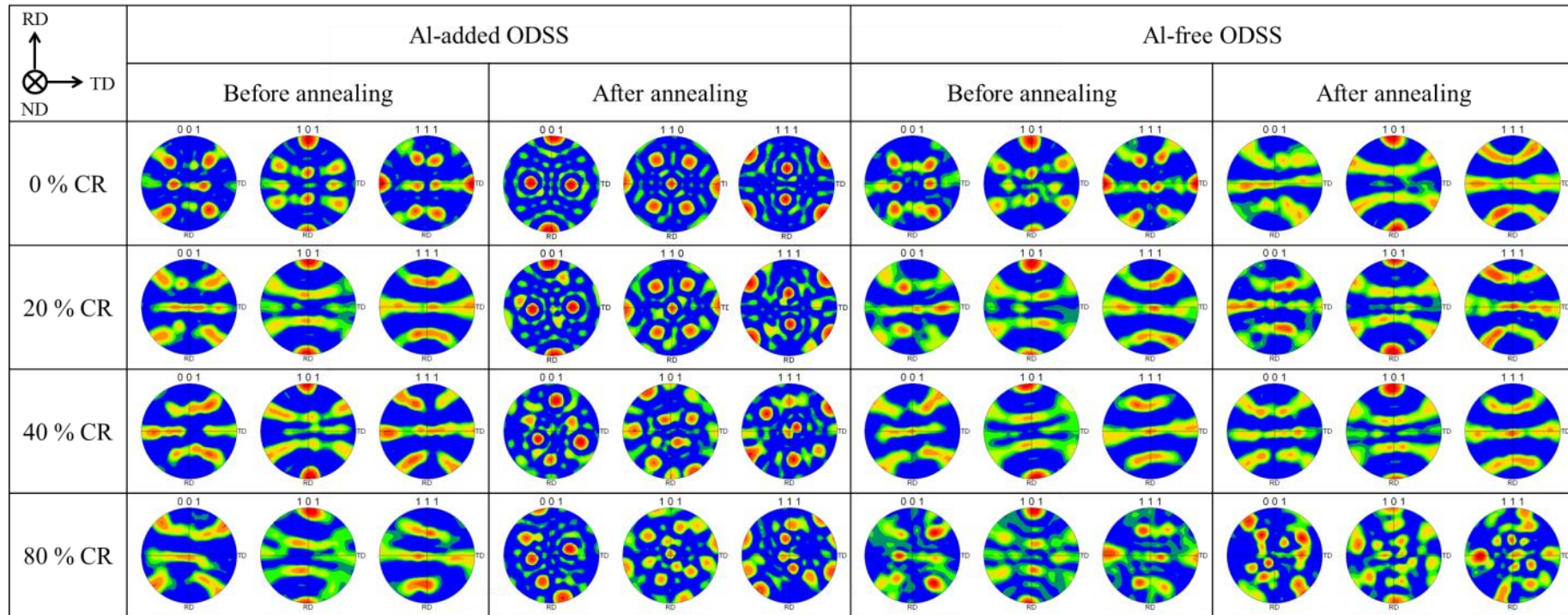


Figure 3-9 Pole figures with each cold rolled ratio before and after annealing

3.3.2.3 Distribution change of dispersed oxide particles by annealing

Recrystallization is accompanied by grain growth through grain boundary motion. In the ODS steels, dispersed oxide particles play a role to pin down the grain boundary motion to cause retardation of recrystallization. Fig. 3-10 shows the morphology of dispersed oxide particles in each case. In the case of Al-added ODS steel, annealing caused remarkable grain growth and softening, indicating that recrystallization, which was accompanied by a remarkable Ostwald ripening, was induced in this ODS steel. Oxide particles are significantly coarser after annealing in as-received material as already shown in Fig. 2-23. As for Al-free ODS steel, the microstructure was surprisingly stable, showing almost no significant change in grain morphology, while the softening is considerable. Because ultra-fine oxide particles such as Y-Ti-O complex were dispersed in Al-free ODS steel, the ODS steels can obtain high strength at elevated temperatures. Consequently, it is suggested that the Y-Ti-O fine oxide particles restrain recrystallization by pinning grain boundaries in Al-free ODS steel, while Al-added ODS steel was easily recrystallized because of weak pinning by a low number density of large Y-Al-O oxide particles. Also, the decreased hardness of Al-free ODS steel may be induced by the coarsening of Y-Al-O oxide particles. In the same vein, the hardness of Al-added ODS steel is lower than that of Al-free ODS steel caused by Al softening effect. After 80 % cold rolled specimen of Al-added ODS steel, the oxide particles are not coarse but similar size with as-received material at 850 °C. Although recrystallization is occurred at 1250 °C, oxide particles are smaller than those after annealing at 1400 °C of as-received material in 80 % cold rolled specimen of Al-free ODS steel. Oxide particle growth is almost depending on annealing temperature. But, recrystallization and grain growth are controlled by multiple factors such as dislocation density, initial grain size and oxide particle distribution morphology. Stored energy by cold rolling accelerates grain movement. Therefore, it is suggested that recrystallization is easier with bigger oxide particles in matrix, as reported by Baker and Martin [15]. These agree with the result of this research.

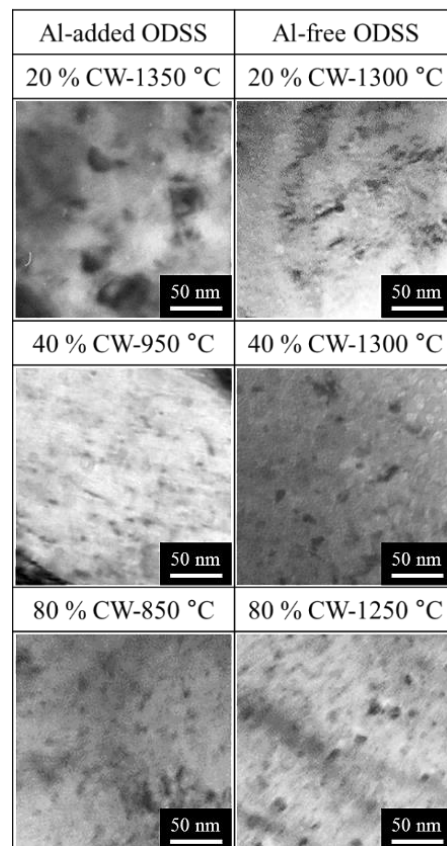


Figure 3-10 Dispersed oxide particles in cold rolled materials after annealing

3.3.3 Effect of cold rolling direction on grain morphology

As well known that body centered cubic (BCC) structure have a preferred crystallographic orientation texture both before and after recrystallization. It is also verified in this study, Chapter 2, which is changed from $\langle 110 \rangle$ to $\langle 100 \rangle$ in Al-added recrystallized ODS steel. Because the cold rolling direction is same with extruded direction during the fabrication processing, the anisotropy remains in elongated grains. Therefore, the cold rolling processing is performed with the different cold rolling direction, which is perpendicular to extruded direction. The change in grain morphology and anisotropy are investigated in this session.

Fig. 3-11 is the effect of cold rolling on the 3D microstructure of deformation texture of Al-added ODS steel. (a) is the definition of three directions of cold rolled specimen and (b) is a stereo-triangle of crystallographic orientation. Noted that each surface from 3D microstructure is not rotating with standard of ND surface, it is just observed surface. As shown in (c), the specimen without cold rolling has elongated grains along with extrusion direction. Top and front surface are similar each other but the side surface shows that many grains oriented in the $\langle 110 \rangle$ direction as well-known as an alpha fiber texture, that is, RD is parallel to $\langle 110 \rangle$ direction shown with light green of stereo triangle. The figure (d) is of 40 % cold rolling along with the rolling direction, which indicates that the orientation relationship is similar to that of without cold rolling, although the front surface indicates that cold rolling makes the grains be fine width.

In contrast to this, the case of cold rolling (e) in the direction of TD has two different behaviors. One is the orientation change in the top surface, that is, the surface orientation is mainly blue $\{111\}$ and partially red $\{100\}$. The second is the front surface, indicating the orientation is mainly rotated to $\{112\}$ because it is distorted by compression strain. The grain morphology has pushed away from cold rolling direction, it seems to be reduced anisotropy, so it appears more equiaxed than that of RD specimen in high magnification. However, they still have anisotropy along with extrusion direction.

Based on the results obtained by EBSD analysis as shown Fig. 3-11, the following texture formation mechanism is considered (Fig. 3-11 (f)). In BCC crystal, the slip direction is $\langle 111 \rangle$ and the specimen axis rotates to $\langle 111 \rangle$ first, and once the axis overshoots the line from $\langle 001 \rangle$ to $\langle 011 \rangle$ edge, the axis rotation is now conversed to the $\langle -111 \rangle$ direction. This lead to the final rotation to the $\langle 011 \rangle$ direction, which is the formation of alpha fiber structure in the extruded ODS steel.

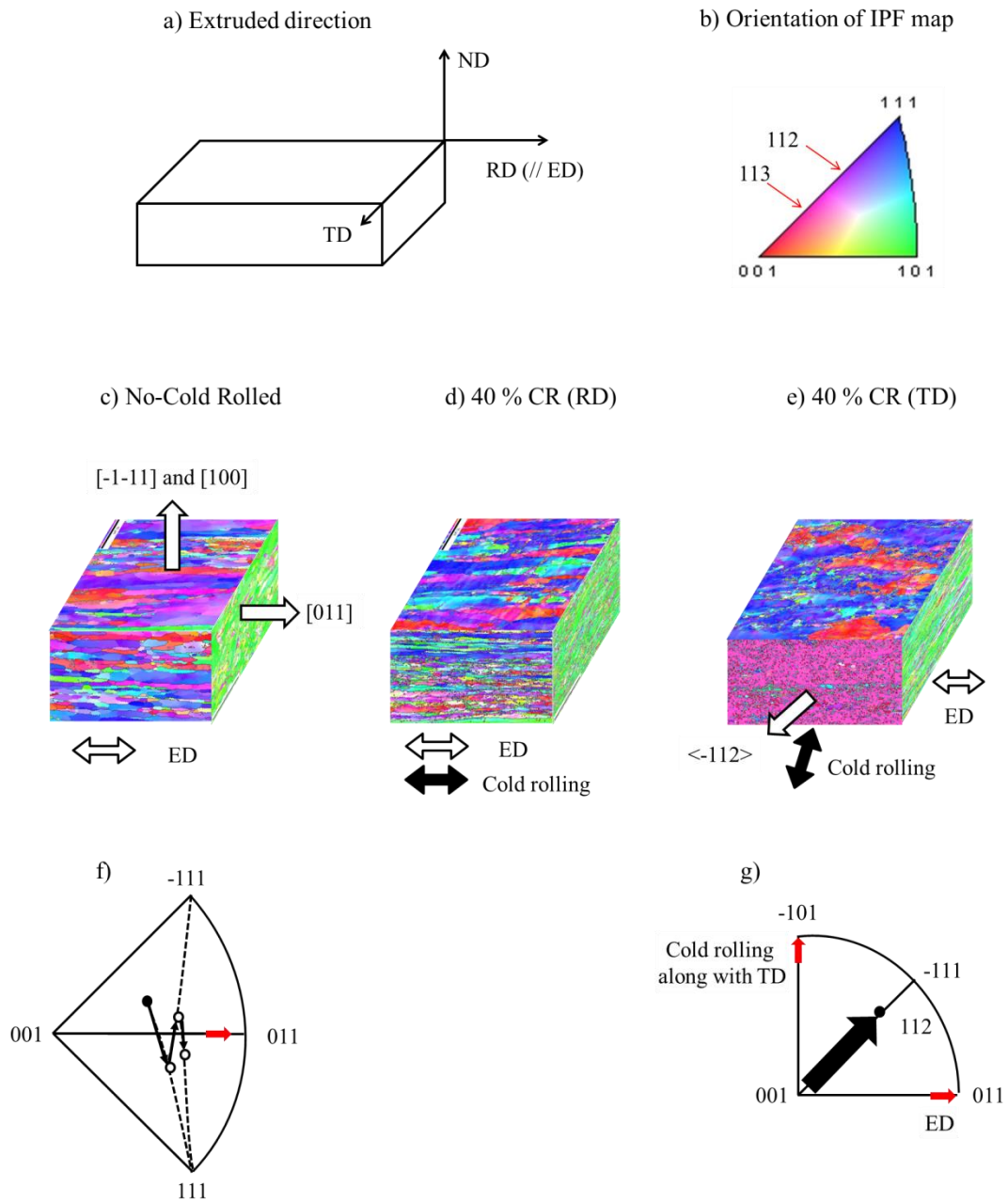


Figure 3-11 Grain orientation of Al-added ODS steel with 40 % cold rolling each direction before recrystallization treatment

After cold rolling perpendicular to the extruded direction, the grain orientation change with rolling direction is shown Fig. 3-11 (g), TD. In this case similar rotation occurs but the rotation direction is not $\langle 011 \rangle$ but $\langle -101 \rangle$ which marked the red arrow with TD. It is considered that the rotation can be proceeding to the combination of two rotations (one is extruded direction and another one is cold rolling direction), and the total direction of the axis can be $\langle -111 \rangle$. This indicates that the axis rotates along the edge of the triangle from $\langle 001 \rangle$ to $\langle -111 \rangle$, as marked black arrow. There is $\langle -112 \rangle$ on this edge indicated in (b). It is well agreed with the experimental results of EBSD analysis.

The cold rolled specimens both perpendicular and parallel to extrusion direction are annealed at 1000 °C for 1 hour, the effects of recrystallization on the deformation structure is investigated. Fig. 3-12 is the 3D structure after recrystallization in both TD (a) and RD (b) rolling direction. In the case of transverse direction, TD, the grains on the front surface are rearranged parallel to extrusion direction. This orientation is similar with that of before cold rolling processing. Also, it is observed that coarse recrystallization partially occurred in $\{110\}$. In case of 40 % cold rolling with RD, the grain is coarser and more anisotropic compared with before recrystallization. It is also clear that the recrystallization occurred and coarse grains were $\{110\}$ and fine grains were $\{111\}$ with anisotropy.

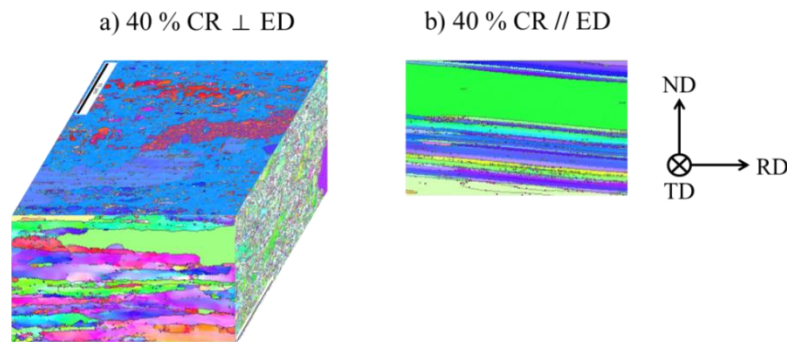


Figure 3-12 Grain morphology of Al-added ODS steel with 40 % cold rolling each direction after recrystallized at 1000 °C

On the other hand, the Al-free ODS steel shows different behavior from Al-added ODS steel in this research. Fig. 3-13 shows the top surface of the specimens, which was pressed directly during cold rolling processing with perpendicular to extruded direction (b) and then after annealing (c). Grain morphology and orientation of these three cases are not significantly changed compared with Al-added ODS steel. This is considered to be due to suppression effect by much stronger pinning effects of grain boundaries by Y-Ti-O oxide particles formed in Al-free ODS steel.

Also, it can be said that Al-added ODS steel are more easily affected by cold rolling caused by Al component because of Al-Y-O oxide particles. Therefore the grain size of each case is finer generally than that of Al-added ODS steel. The annealing after cold rolling appears to show starting recrystallization, but it is partial and still remained anisotropy of grain morphology.

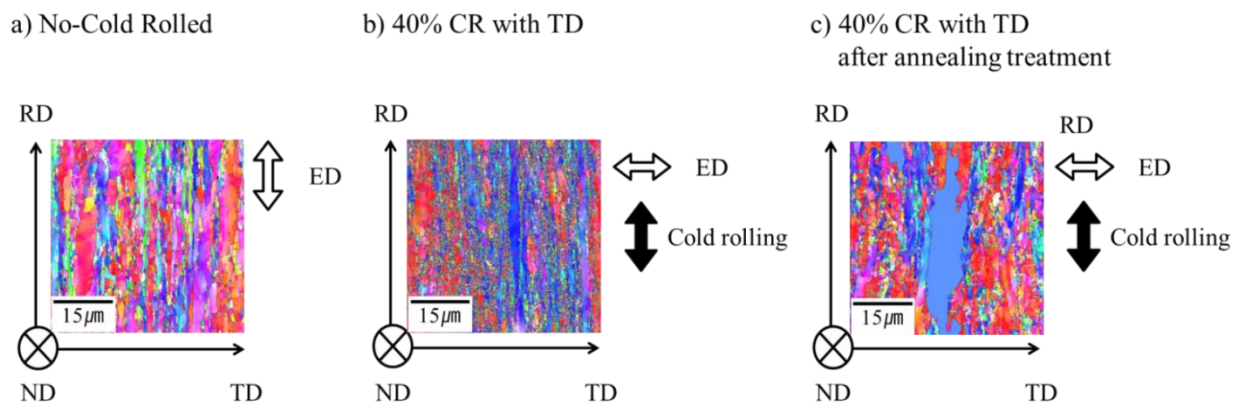


Figure 3-13 Grain morphology observed on ND surface in Al-free ODS steel; (a) before and (b), (c) after cold rolling along with TD

3.3.4 Grain morphology on cyclic cold rolling processing in ODS steels

3.3.4.1 The hardness change with cyclic cold rolling processing

During the fabrication processing, cladding tubes or sheets of structural material were subjected by several cycles of annealing and cold rolling to improve mechanical properties of ODS steels.

Fig. 3-14 is indicated that the Vickers hardness change with annealing after first and second cold rolling of 40 % rolling ratio. In this research, the annealing temperature was selected to be 900 °C in Al-added ODS steel and 1200 °C in Al-free ODS steel. Al-free ODS steel is still higher hardness than that of Al-added ODS steel, except annealed at 1400 °C in second cold rolled specimen.

The hardness of Al-added ODS steel is not significantly reduced, the difference about 50 Hv. Also, the hardness is similar with first cold rolled specimen. A more decrease in the hardening was observed after annealing at 1250 °C. In case of Al-free ODS steel, the hardness is remarkably reduced at around 1350 °C, and finally reached to about 150 Hv after annealing at 1400 °C as a second annealing.

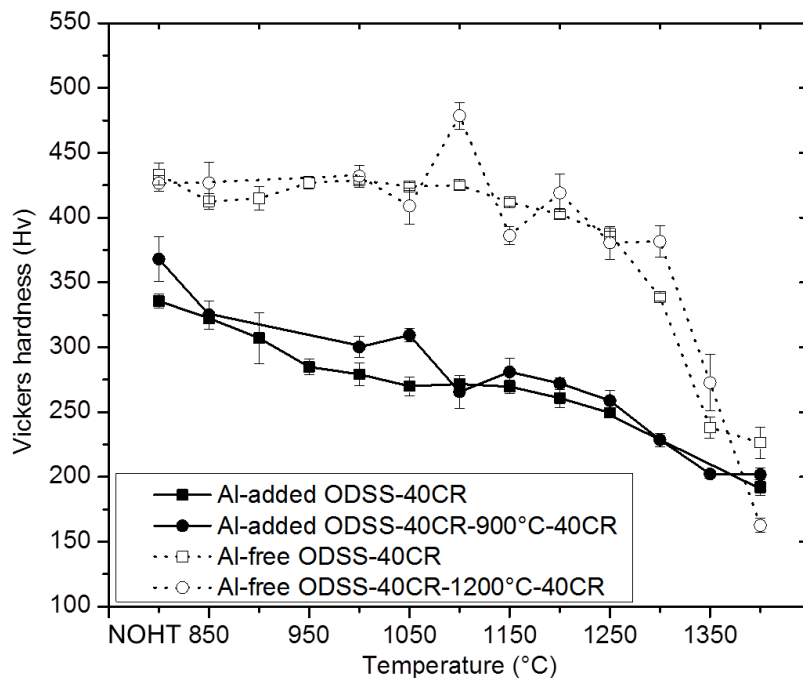


Figure3-14 Vickers hardness of 40 % cold rolled and second 40% cold rolled materials after annealing

3.3.4.2 Grain morphology change by annealing processing

Fig. 3-15 shows the change in grain morphology after annealing of second cold rolling processing. Both Al-added and Al-free ODS steels tend to recrystallize with increasing annealing temperature. In Al-added ODS steel, the recrystallization started partially at 1000 °C. After annealing at 1300-1350 °C, the grains are almost fully recrystallized. Al-free ODS steel is more difficult to recrystallize than that of Al-added ODS steel, and second cold rolled specimen started recrystallization at around 1200 °C.

Fig. 3-16 shows the results of EBSD analysis before and after annealing at 1400 °C of both Al-added and Al-free ODS steel. Before annealing, both second cold rolled ODS steels have grain with $\{111\}/\{100\} \langle 110 \rangle$ orientation in the TD direction, which corresponds to α -fibre texture. Al-added ODS steel has many sub-grains and dislocations in the large grains as indicated with white lines of misorientation angle below 5 °. After annealing at 1400 °C, the both of ODS steels are recrystallized and grain growth occurs.

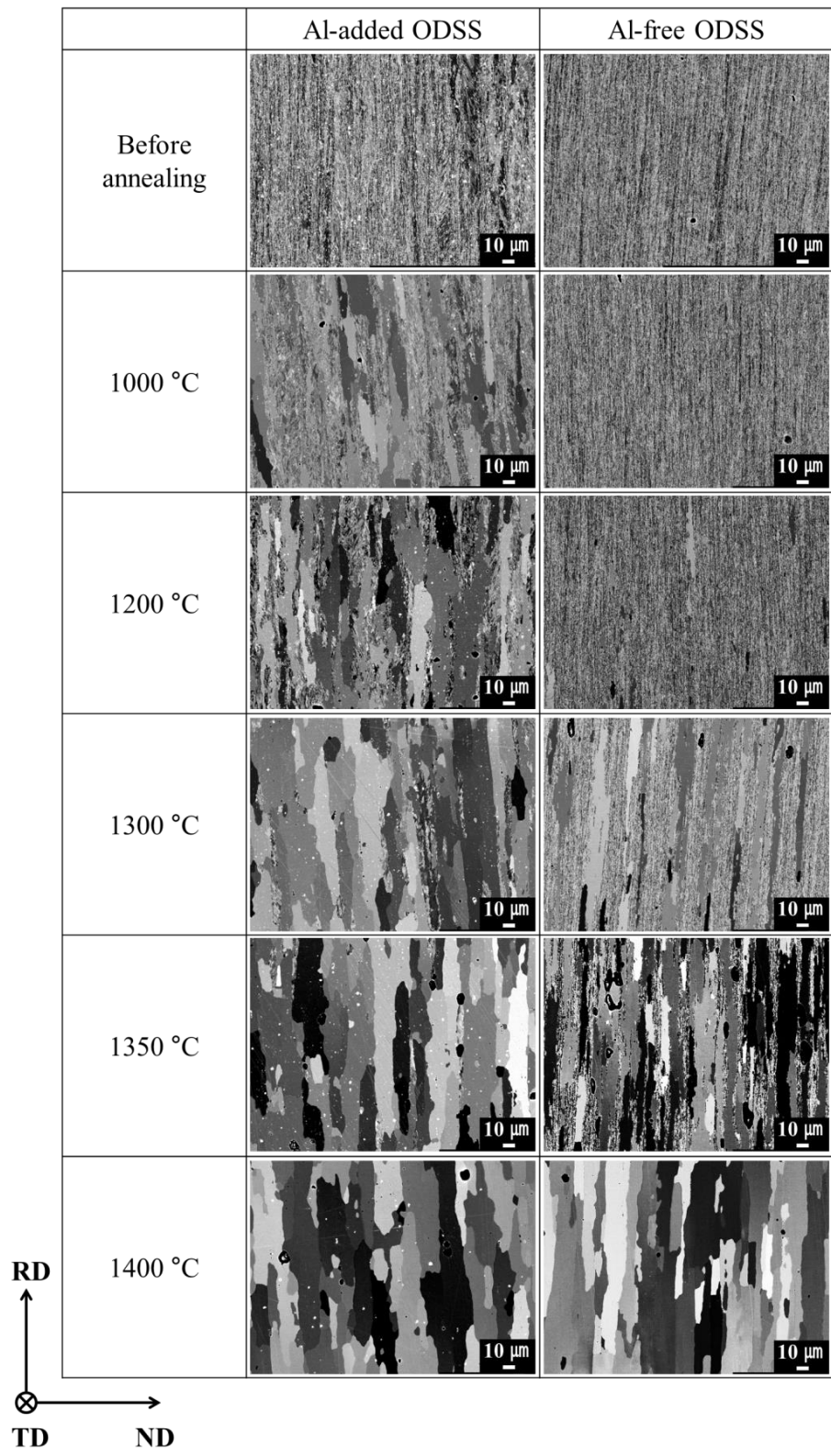


Figure 3-15 Grain morphology of second cold rolled materials after annealing at each temperature

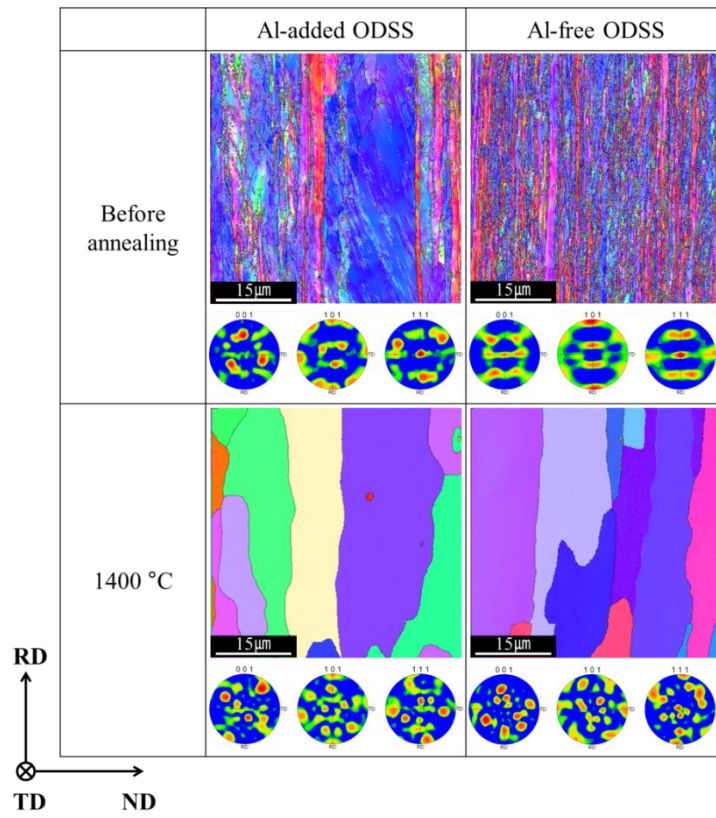


Figure 3-16 Grain orientation map and pole figure before and after annealing at 1400 °C

3.4 Summary

The effect of cold rolling on recrystallization behavior of 15-Cr ferritic ODS steels was investigated. The change of microstructure is particularly noticeable in cold rolling and annealing conditions. The results obtained are summarized as follows;

- 1) The recrystallization temperature is decreased with increasing cold rolling ratio, which is considered to be due to acceleration of microstructure change by strain induced stored energy. The Al-free ODS steel is still difficult to recrystallize caused by fine oxide particles, although the effect of cold roll is evident.
- 2) The cold rolling direction also influences on grain morphology and recrystallization behavior in Al-added ODS steel, and the rolling to the perpendicular direction to cold rolling direction induces the rotation of the RD from $\langle 110 \rangle$ to $\langle 112 \rangle$. The recrystallization temperature is not significantly changed by cold rolling direction.
- 3) ODS ferritic steel fabricated by hot isostatic processing has equiaxed grains, and annealed specimens after cold rolling is rearranged to grain. It is suggested that the fabrication processing is more effected on grain morphologies than that of cold rolling processing.

References

1. Bin LENG, Shigeharu UKAI, Yoshito SUGINO, Qingxin TANG, Takeshi NARITA, Shigenari HAYASHI, Farong WAN, Satoshi OHTSUKA, Takeji KAITO, "Recrystallization Texture of Cold-rolled Oxide Dispersion Strengthened Ferritic Steel", *ISIJ international*, **51** (2011) 951-957
2. M. Hölscher, D. Raabe, K. Lücke, "Rolling and recrystallization textures of bcc steels", *Steel research*, **62** (1991) 567-575
3. R. K. Ray, J. J. Jonas, R. E. Hook, "Cold rolling and annealing textures in low carbon and extra low carbon steels", *International Materials Reviews*, **39** (1994) 129-172
4. D. Dorner, S. Zaefferer, D. Raabe, "Retention of the Goss orientation between microbands during cold rolling of an Fe 3% Si single crystal", *Acta Mater.*, **55** (2007) 2519-2530
5. S.H. Noh, B.J. Kim, R. Kasada and A. Kimura, "Diffusion bonding between ODS ferritic steel and F82H steel for fusion applications", *J. Nucl. Mater.*, **426** (2012)208-213
6. Shigeharu UKAI, Toshio NISHIDA, Takanari OKUDA, Tunemitsu YOSHITAKE, "Development of Oxide Dispersion Strengthened Steels for FBR Core Application, (II)", *J. Nucl. Sci. Techn.*, **35** (1998) 294-300
7. S. V. Mehtonen, L.P.Karjalainen,D.A.Porter, "Hot deformation behavior and microstructure evolution of a stabilized high-Cr ferritic stainless steel", *Mater. Sci. Eng. A*, **571** (2013) 1-12
8. D. Sornin, T.Grosdidier, J.Malaplate, I.Tiba, P.Bonnaillie, N.Allain-Bonasso, D.Nunes, "Microstructural study of an ODS stainless steel obtained by Hot Uni-axial Pressing", *J. Nucl. Mater.*, **439** (2013) 19-24
9. P. Unifantowicz, Z. Oksiuta, P. Olier, Y. de Carlan, N. Baluc, "Microstructure and mechanical properties of an ODS RAF steel fabricated by hot extrusion or hot isostatic pressing", *Fusion Eng. Des.*, **86** (2011) 2413-2416
10. P. Dou, A. Kimura, T. Okuda, M. Inoue, S. Ukai, S. Ohnuki, T. Fujisawa, F. Abe, "Polymorphic and coherency transition of Y–Al complex oxide particles with extrusion temperature in an Al-alloyed high-Cr oxide dispersion strengthened ferritic steel", *Acta Mater.*, **59** (2011) 992-1002
11. M. Abe, Y. Kokabu, Y. Hayashi, S. Hayami, "Effect of grain boundaries on the cold rolling and annealing textures of pure iron", *T. Jpn. I. Met.*, **23** (1982) 718-725

12. L.S. Toth, A. Molinari, D. Raabe, "Modeling of Rolling Texture Development in a Ferritic Chromium Steel", *Metall. Mater. Trans. A*, **28** (1997) 2343-2351
13. Chun-Liang Chen, You-Ming Dong, Shu-Mei Fu, "Strain Heterogeneity, Recovery and Recrystallization of Nanostructured ODS Alloys during Cold Deformation", *Mater. Trans.*, **53** (2010) 795-1800
14. R. D. Doherty, "Primary recrystallization", *Encyclopedia of Materials: Science and Technology* (2011) 7847-7850
15. I. Baker, J. W. Martin, "Effect of fine second phase particles on deformation structure in cold rolled copper single crystals", *Mater. Sci. Tech.*, **17** (1983) 459-468

Chapter 4

Factors Controlling Hardness of ODS Ferritic Steel Before and After Recrystallization

4.1 Introduction

The nanostructure characteristics of the ODS steel with ultra-fine dispersed oxide particles and sub-microns of grain sizes provide many advantages in the performance of structural materials used in a harsh environment of nuclear power systems. These microstructures have each strengthening factor in the matrix of ODS steel: 1) strengthening by fine-grains was interpreted on the basis of the Hall-Petch effect in spite of very limited literature data [1], 2) strengthening by fine oxide particles, and 3) strengthening by dislocation. However, the relationship and interactions between each factor are intensely complicated.

There are several factors determining recrystallization behavior such as cold rolling, heat treatment method and chemical compositions, and it is necessary to control these factors. Although it is expected that the dispersed particles pin down grain boundaries to retard recrystallization, the effect of the dispersion morphology of the particles was not fully understood yet. The contribution of each strengthening source for mechanical properties also works for retarding recrystallization.

In the previous study, it is confirmed that recrystallization behavior is influenced by steel compositions and cold rolling. Annealing for recrystallization results in the morphology changes in not only grains but also dispersed oxide particles and possibly the other precipitates formation. However, the mechanism of strengthening matrix and retarding recrystallization as well as the roles of each microstructure in ODS steels are not clearly understood.

In this research, the factors controlling mechanical properties of ODS steels are discussed on the bases of before and after recrystallization, especially with focusing on the role of each microstructure change by recrystallization on the hardness. Also the effect of grain shape anisotropy in the hardness is investigated.

4.2 Experimental procedure

The materials used in this study are Al-added and Al-free ODS ferritic steel, same as Chapter 1 and 2. Also, cold rolling and annealing processing are carried out with same method in the previous chapters. Vickers hardness is measured using a Micro Vickers Hardness tester with a load of 1kgf and microstructure observation is performed by FE-SEM and TEM.

4.3 Results and discussions

4.3.1 Grain size effect on mechanical properties

4.3.1.1 Grain boundary strengthening mechanism

In polycrystalline material, grain size has a great influence on the mechanical properties. Because grains usually have varying crystallographic orientations, grain boundaries exist. While undergoing deformation, the dislocation motion takes place. Grain boundaries may act as obstacles to dislocation motion because slip planes are changed at the grain boundaries caused by orientation of the grains. Also the large atomic mismatch between the different grains may generate a repulsive stress field to oppose continued dislocation motion, depending on the strain field around dislocation.

4.3.1.2 Anisotropy in the grain shape before and after annealing

The aspect ratios of the grains between the cross and parallel section to the extrusion direction are shown in Fig. 4-1 for both the ODS steels without cold rolling. The aspect ratio of Al-added ODS steel is about 0.5, and they increase with increasing annealing temperature (a). In Al-free ODS steel (b), the aspect ratio is a little higher than that of Al-added ODS steel before annealing and it remains after annealing. The anisotropy of both ODS steels are reduced by recrystallization or annealing.

Fig. 4-2 shows grain aspect ratio of cold rolled specimen before and after recrystallization. In Al-added ODS steel, grains have low aspect ratios before annealing, which means they are elongated with a significant anisotropy (a). The grains tend to be equiaxed after annealing (b), indicating recrystallization. In case of Al-free ODS steel, the anisotropy of grains is lower before annealing (c), and even after annealing, they don't changed (d). The grains of both steels still have anisotropy, although they become more equiaxed after annealing.

4.3.1.3 Hall-Petch relationship in ODS steels

For conventional polycrystalline materials, the hardness, H_v , is related with the average grain size, d , in the well-known Hall-Petch relationship [2, 3],

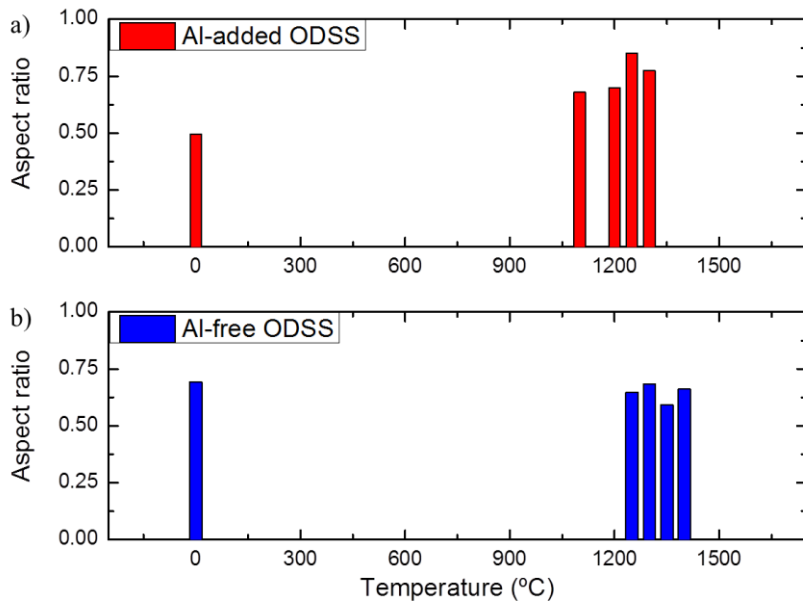


Figure 4-1 Grain aspect ratio before and after annealing in (a) Al-added and (b) Al-free ODS steel

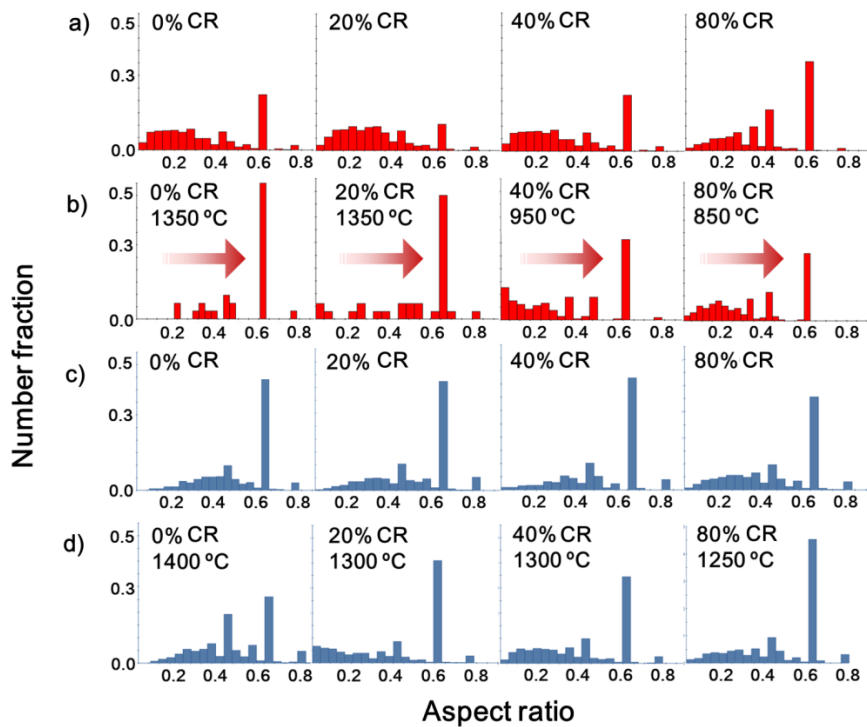


Figure 4-2 Grain aspect ratio; a) before and b) after annealing of cold rolled Al-added ODS steel, c) before and d) after annealing of cold rolled Al-free ODS steel

$$H_v = H_0 + kd^{-1/2} \quad (4.1)$$

where H_0 and k are constants. Normally the value of k is positive, or the hardness of a polycrystalline increase with a refinement of grains. In ODS steel, the strengthening is due to both the fine grains and oxide particles.

Although refinement of grain size usually resulted in strengthening, the materials with nano-sized very fine grains may not be subject to vacancy hardening because many grain boundaries and particle-matrix interfaces act as sinks allowing elimination of excess vacancies [4]. From this reason, the grain boundaries of nano-sized grains have smaller interfacial excess energies than that of conventional grain boundaries, which may make dislocations penetrate into a neighboring grain and soften the nano crystalline materials [3]. In other words, the Hall-Petch relationship breaks down. G. E. Fougere et. al [5] reported that nano crystalline of Cu showed no hardening with decreasing the grain size below 10 nm as shown in Fig. 4-3 [6]. The Hall-Petch break down is generally presumed to occur in the grain size range below 20 nm or 10 nm. There is no critical value of the grain size showing the break down because it is rather different to measure the nano-scaled grain size. The Hall-Petch plots were attempted in this research to investigate the Hall-Petch relationship in ODS steels with fine grains ranging from 50 nm to 500 nm.

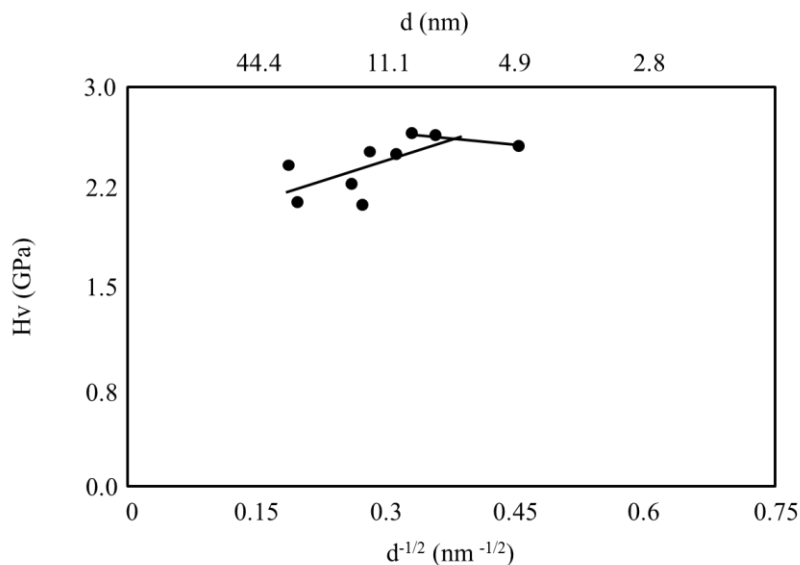
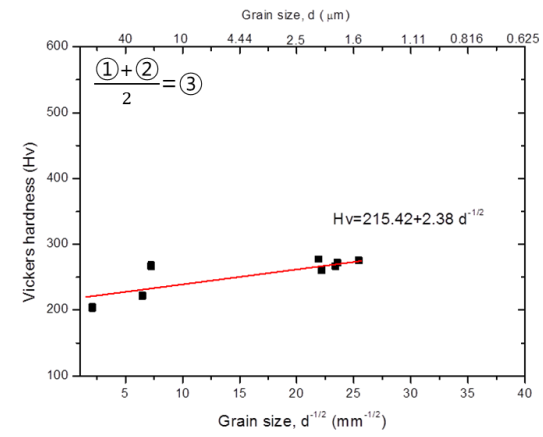
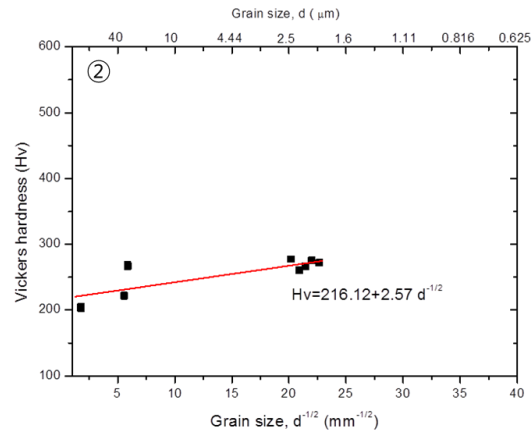
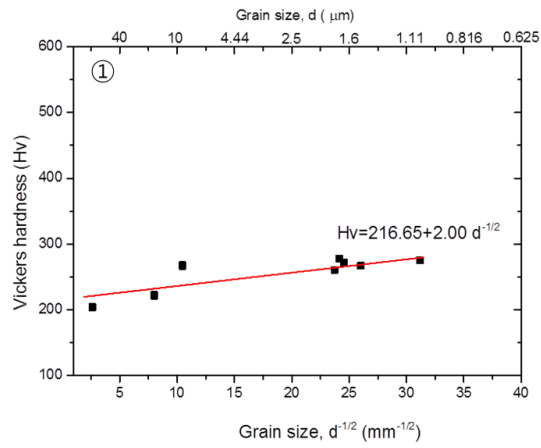


Figure 4-3 Hall-Petch plot of Vickers microhardness, H_v , for nano-crystalline Cu [6]

Fig.4-4 shows the Hall-Petch relation of (a) Al-added and (b) Al-free ODS steel with and without cold rolling. Since the grains have an anisotropy in the grain shape, the grain sizes are shown as three values as follows; ① is the average grain size measured perpendicular to the extruded direction, ② is the average grain size parallel to the extruded direction and ③ is the average of ① and ②. Although anisotropies are confirmed in the tensile properties and grain aspect ratio, these three Hall-Petch relation plots are similar among them in Al-added ODS steel. The slope of Al-added ODS steel is very low (2.5 in the graph). In case of Al-free ODS steel, the Hall-Petch plots are similar among three graphs. However, the trend line is remarkably different from that of Al-added ODS steel. In this steel, the grain morphologies are stable during cold rolling and annealing, the range of grain size is not remarkably spread, and the reduction of Vickers hardness is caused mainly by recovery. The trend lines can be divided into two types for the selected grain size ranges. In the right side of the graph, the slope of the line is much larger than that of Al-added ODS steel. However, in the left side the slope is reduced. Since recrystallization results in not only grain boundaries but also the morphology change of oxide particles, that is also another important factor controlling the strength of ODS steels.

a) Al-added ODS steel



b) Al-free ODS steel

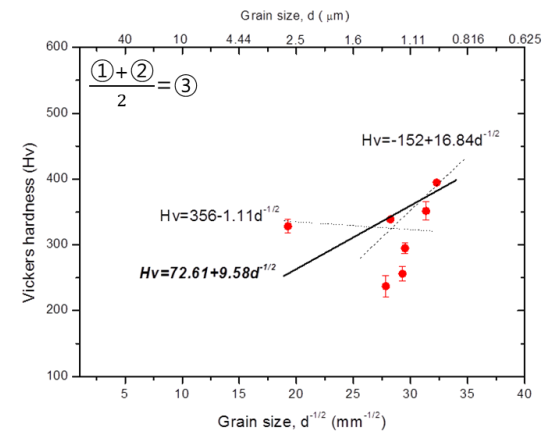
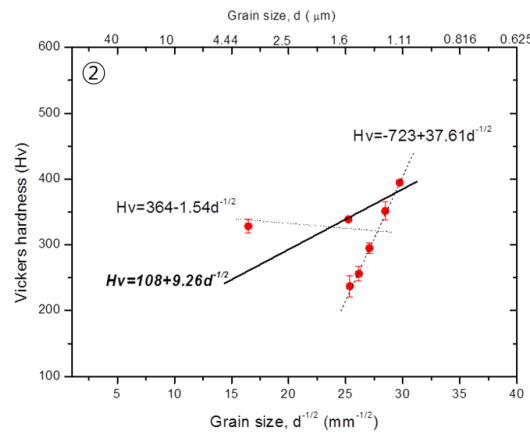
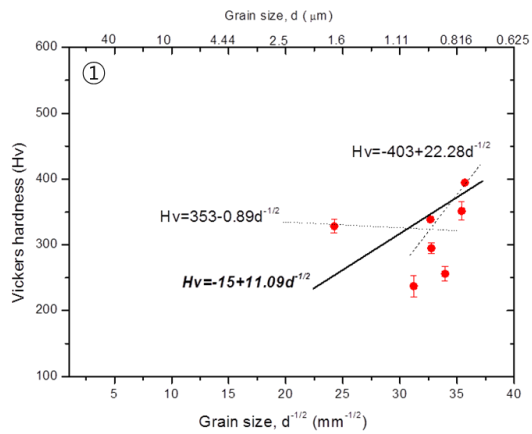


Figure 4-4 Hall-Petch plots of Vickers hardness with grain size; (a) Al-added and (b) Al-free ODS steel

4.3.2 Dispersion strengthening

Dispersion strengthening by thermally stable oxide particles is a method for improving high temperature strength of alloys. Thermo-mechanical processing plays an important role in the control of the final microstructure and associated mechanical properties [7]. Coarsening of oxide particles leads to a decrease in number density, which results in an increase in mean particle distance, and thus decreasing in the strength [8].

In Chapter 1, it was introduced that the Al-addition to ODS steels improved corrosion resistance in severe environment of nuclear power systems, although the mechanical properties are degraded by the addition. The reduction of the mechanical properties is caused by the change in the oxide particles distribution morphology from fine to coarse distribution [9-11]. Although dispersoids are more thermally stable than the precipitates in the conventional super alloys such as carbides or intermetallic compounds, the coarsening of complex oxide particles at elevated temperatures has been observed not only our research but also elsewhere [12]. Finally, the addition of small amount of Zr to the Al-added ODS steels results in a significant increase in creep strength at 700 °C because of the refinement of oxide particles of Y-Zr-O [13-15].

The oxide particle distribution morphology is expected to be changed by annealing in both Al-added ODS steel and Al-free ODS steel. Fig. 4-5 shows that the effect of cold rolling and/or annealing on the average size and size distribution of oxide particles before and after annealing. In case of Al-added ODS steel, the oxide particles remarkably became coarser about 2 times after recrystallization, and the particle size is widely distributed. In the Al-added ODS steel 20 % cold rolled then annealed at 1350 °C, the oxide particles are coarser than before annealing. In 80 % cold rolled specimen, the distribution morphology is similar with that in as-received material even after the annealing at 850 °C. Dispersed oxide particles in Al-free ODS steel are surprisingly stable, showing almost no significant change between before and after annealing. The oxide particle size of 80 % cold rolled specimen after recrystallization is 2 times coarser after annealing at 1250 °C.

Our previous works [16, 17] indicated that Al addition caused a decrease in the strength of ODS steels caused by the formation of Y-Al-O oxide particles, of which the size were 3 times larger than Y-Ti-O oxide particles.

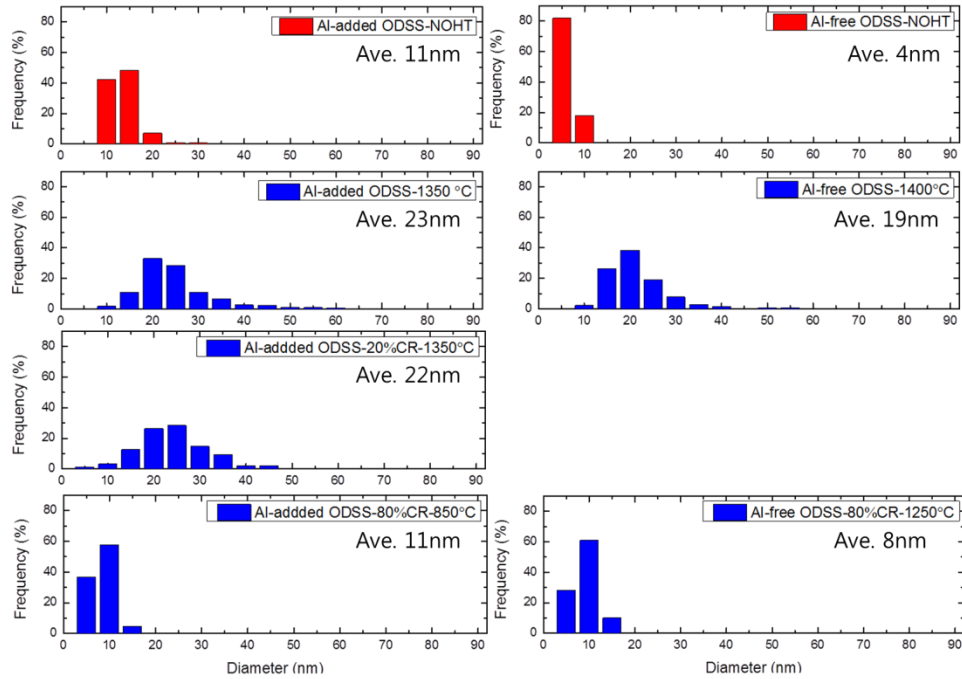


Figure 4-5 Distribution of oxide particles in Al-added and Al-free ODS steel

Fig. 4-6 (a), (b) and (c) show the distribution morphologies of oxide particles after recrystallization of Al-added ODS steel, indicating that the oxide particles become significantly coarser than before recrystallization. And the particles exist not only (a) in the grains but also (b) at grain boundaries. The oxide particles still play a role as obstacles to dislocation movement as pinning effect, although the size is bigger than before annealing (Fig. 4-6 (c)). As for Al-free ODS steel, ultra-fine oxide particles such as Y-Ti-O complex is bigger after annealing, but it is still fine as comparison with Al-added ODS steel. Therefore, the strength of Al-free ODS steel is still remained by the fine oxide particles as shown in Fig. 4-6 (d). A few large precipitates (e) are sometimes observed.

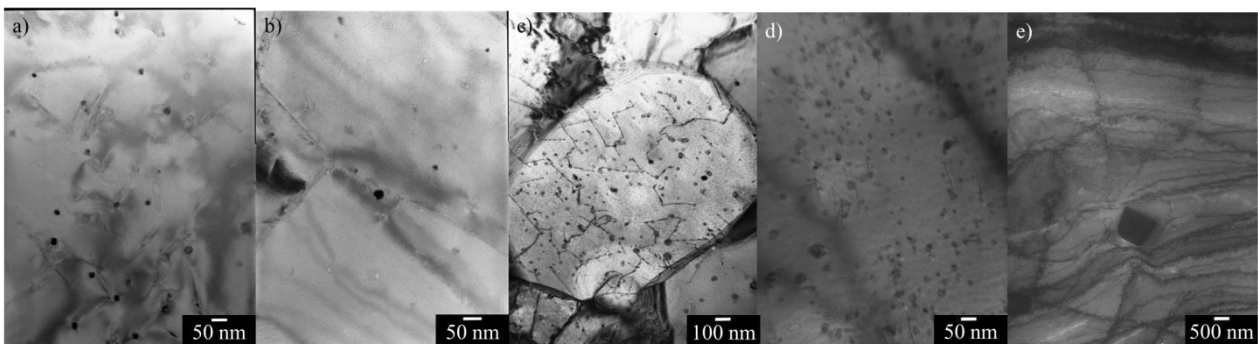


Figure 4-6 Oxide particles after recrystallization or annealing in Al-added and Al-free ODS steels

The amount of strengthening by oxide particles is estimated by Orowan type by-passing mechanism (In Chapter 1). Fig. 4-7 shows the estimated Orowan strengthening mechanism based on the following calculated equation,

$$\Delta\sigma_{OR} = M\alpha\mu b\sqrt{Nd} \quad (4.2)$$

where M is Taylor factor 3.06, which is converted from shear stress to yield stress, α is constant, it is needed for barrier application of oxide particles. If it is 1, the oxide particle is perfectly applied for barrier of dislocation migration. But dispersoids are not always applied for barrier perfectly in experimental results, so it is 0.8 in this study [22]. $\mu=80500$ MPa, $b=0.286$ nm, N is the number density and d is the average diameter of particles.

Orowan strengthening is decided from oxide particle size and number density of oxide particle distribution. The number density of oxide particles in cold rolled specimen is higher than without cold rolled specimen. Since oxide particles are very stable at high temperature, the particle size is fine and number density is high in (a) 80 % cold rolled Al-added ODS steel even recrystallization is occurred at 850 °C. The most of stored energy by cold rolling is used for grain migration and grains are growth, meanwhile dispersed oxide particles morphology is changed as high annealing temperature. The Orowan strengthening of Al-free ODS steel (b) is also changed with annealing temperature irrespective cold rolling. Orowan strengthening of Al-free ODS steel is higher than that of Al-added ODS steel.

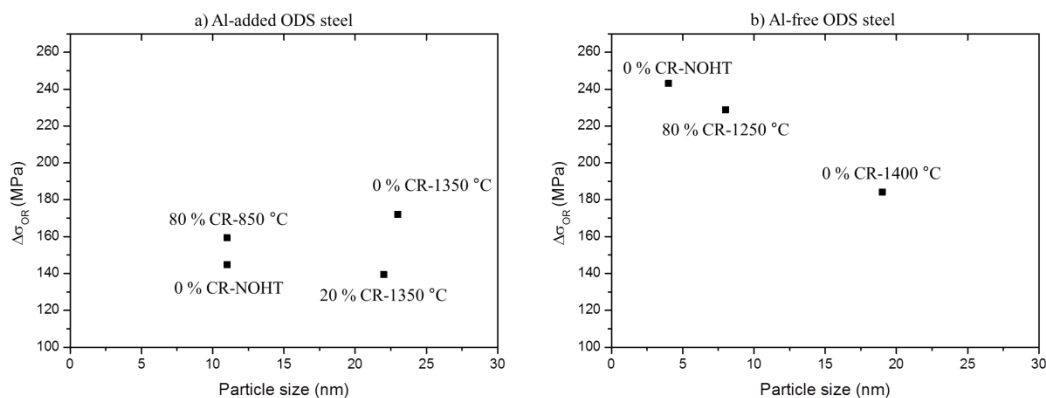


Figure 4-7 Estimated Orowan strengthening from the TEM observation of oxide particles

4.3.3 Work hardening

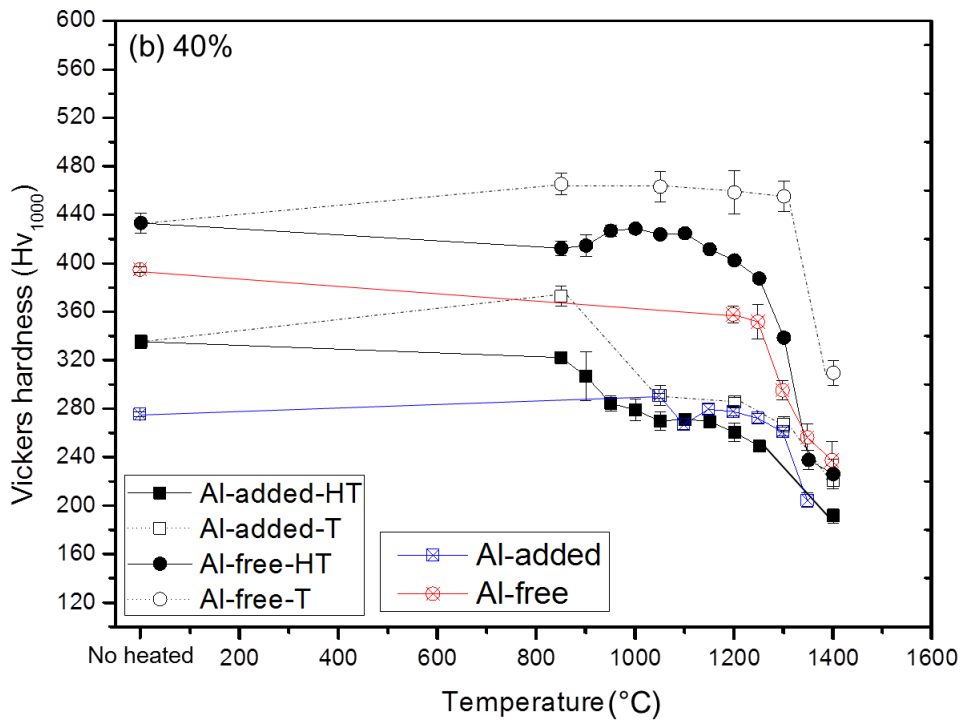
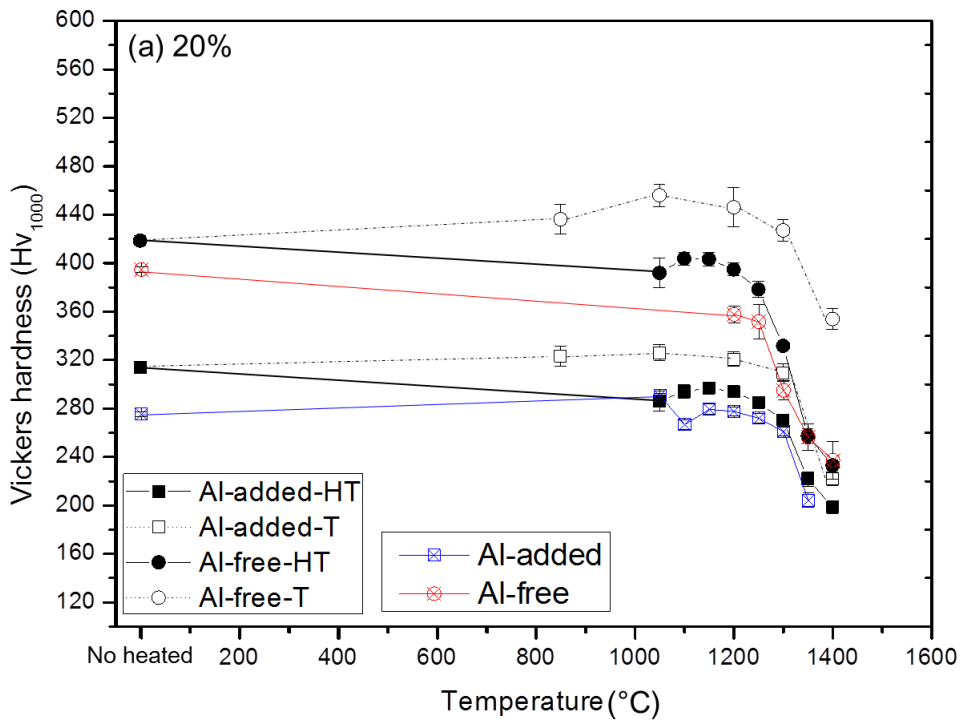
Since the as-received specimens were subjected to annealing at 1050 °C for 1 hour, the roll of residual dislocations can't be large. Meanwhile, many dislocations are generated in the cold rolled specimens. The dislocations with high density act as a source of driving force for recrystallization, and recrystallization becomes easy to occur at a low temperature. Therefore, the factors controlling strength of cold rolled specimens includes residual dislocation density, grain size and oxide particles. Therefore, the annealing is performed without isochronal remain time, which heating and just cooling down in furnace to the retard recrystallization and try to annihilation of dislocation. Fig. 4-8 is indicated the results.

It is indicated to (a) 20 %, (b) 40 %, (c) 80 % reduction ratio of cold rolling both Al-added and Al-free ODS steel. Vickers hardness of "T" is heating and just cooling without remaining time, also Vickers hardness of "HT" is annealed case for 1 hour at each temperature for recrystallization. Without cold rolled specimen is marked blue and red symbol for Al-added and Al-free ODS steel, respectively.

The hardness before annealing (without heated) was increased with increasing reduction ratio of cold rolling as explained Chapter 3. The different amount after annealing (HT) in each cold rolling level is similar between the steels with and without Al addition.

Difference between annealing (HT) and heating without remaining time (T) is reduced as recovery or recrystallization behavior occurred, which the dislocation density and grain size are changed. Since Vickers hardness, also strength of ODS steel is affected by multiple factors such as phase state, grain size and dispersed oxide particles.

The 80 % cold rolled specimen is easy example to roughly divide into each factor. (c) The difference of hardness between as-received and cold rolled specimen is due to high dislocation density (green arrow, ΔH_D). 80 % cold rolled specimen of Al-added ODS steel shows rapid reduction of hardness after annealing at 850 °C, which is revealed as recrystallization. As above research, the size and number density of oxide particles is not changed in this temperature, thus the strengthening amount from oxide particle is not changed both annealing and heating without remaining time. In case of annealing, the remaining time for recrystallization is not enough; the grain is still not recrystallized at same annealing temperature at 850 °C. As-received specimen without cold rolling (marked blue line)



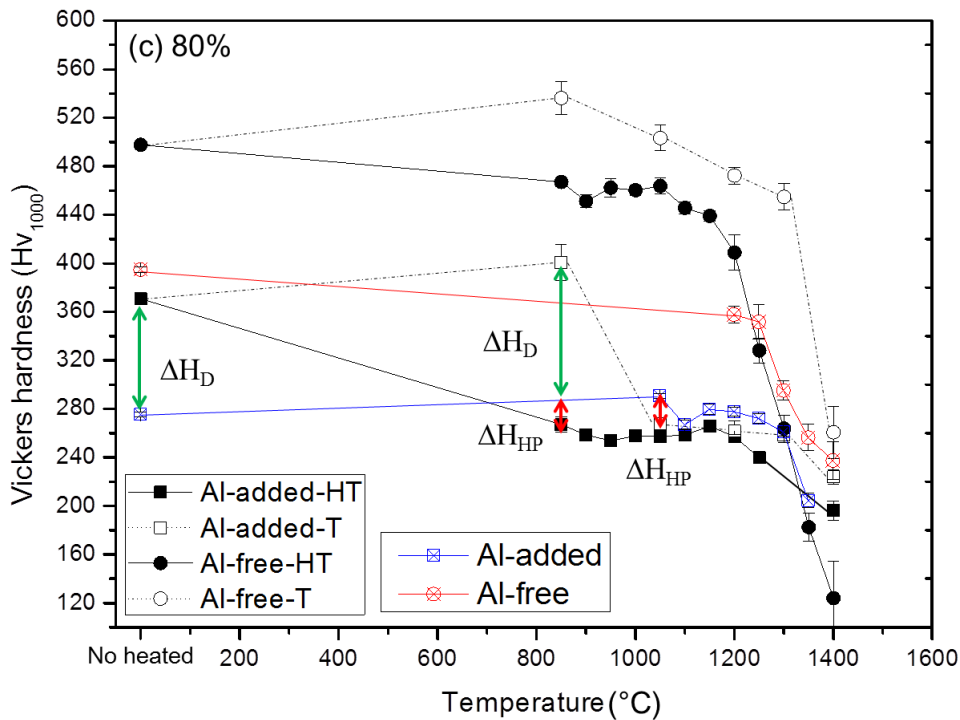


Figure 4-8 The Vickers hardness of Al-added and Al-free ODS steel with each cold rolling ratio at different annealing temperature; (a) 20 %, (b) 40 % and (c) 80 %

also not occurred recrystallization behavior at 850 °C, the difference between as-received and heating treatment specimen can be ΔH_D . The hardness difference between as-received and annealing specimen is from the grain size different, ΔH_{HP} (marked red arrow). After annealed at 1050 °C, the heating treatment specimen is reduced as similar with recrystallized specimen by annealing. At that time, the different hardness between as-received and heating treatment specimen is ΔH_{HP} . The annealing effect on Vickers hardness of Al-free ODS steel are similar with that of Al-added ODS steel, but the interaction between each strengthening factor are more complicated, because oxide particles are coarse at recrystallized temperature. It is assumed that the hardness of Al-free ODS steel is more dependent on oxide particles than that of Al-added ODS steel.

4.3.4 Factors controlling strengthening in ODS steels

As shown in the above results, the grain and dispersed oxide particles are the main factors controlling strengthening in the matrix of ODS steels, and the contribution of these factors to the strengthening is changed by annealing at elevated temperatures.

When the Orowan strengthening is much greater than the Hall–Petch strengthening, it is difficult to assess the contribution of the Hall–Petch strengthening experimentally [1]. Hazzledine [18] examined this issue by calculating the “direct strengthening” from the dispersoids, and the “indirect strengthening” from grains, i.e., the Hall–Petch strengthening. He found that in most realistic cases the maximum possible indirect strengthening by the Hall–Petch effect is greater than the direct strengthening due to the dispersoids. Therefore, dispersoid-strengthened polycrystals, with their exceedingly stable grain sizes, are useful for examining the temperature dependence of the strength of fine-grains materials [19, 20]. There is a thread of connections into Hall-Petch breaks down.

The contribution sources to the yield stress σ_y for pure metal at room temperature (which is a low homologous temperature for a ferritic steel) is simply estimated as [1, 18, 19, 21],

$$\sigma_y = \sigma_m + \sigma_{OR} + \sigma_{HP} \quad (4.3)$$

where σ_m is the matrix yield stress for an infinite grain size, σ_{OR} is the Orowan strengthening stress caused by dispersoids and σ_{HP} is the Hall-Petch strengthening stress caused by grain boundaries. And, σ_m is given by:

$$\sigma_m = \sigma_0 + \sigma_D \quad (4.4)$$

where σ_0 is Peierls stress and σ_D is work hardening by cold rolling. In cold rolled material, the dislocation hardening is significantly higher, then σ_D is increasing.

The relationship between yield stress and Vickers hardness can be assumed [23, 24],

$$\Delta\sigma_y = 3\Delta H_v \quad (4.5)$$

This relation is also confirmed in this study, in Chapter 2 (Fig. 2-17), where Vickers hardness is proportional to the tensile strength about 3 times.

The contribution from work hardening is expressed as,

$$\Delta H_D = \alpha \mu b \sqrt{\rho} \quad (4.6)$$

α is constant, μ is shear modulus, b is Burger's vector and ρ is dislocation density.

Table 4-1 shows the summary of characteristic features of microstructures in each specimen together with the results of Vickers hardness measurement. $\Delta\sigma_{OR}$ can be estimated by the size and number density of oxide particles observed by TEM following Orowan type strengthening mechanism. The dislocation density, ρ , is almost same in each material, because the as-received materials are annealed at 1050 °C in fabrication processing and cold rolled specimens are tested after recrystallization in Table 4-1. The dislocation density ΔH_{v_D} can be ignored. Therefore, ΔH_{v_m} can be obtained.

According to equation (4.3) and (4.4),

$$\Delta H_{v_{ex.}} - \Delta H_{v_{OR}} = \Delta H_{v_{HP}} + \Delta H_{v_0} \quad (\text{if, } \Delta H_{v_D} \approx 0) \quad (4.7)$$

$$\Delta H_{v_{ex.}} = \Delta H_{v_0} + \Delta H_{v_{HP}} + \Delta H_{v_{OR}} \quad (\text{if, } \Delta H_{v_D} \approx 0) \quad (4.8)$$

Table 4-1 Summary of characteristic features of microstructure in each specimen

Material	Material condition		Grain size (μm)	Hv (exp.)	Oxide particle observed by TEM	
	Cold rolling	Annealing			Number density (m ⁻³)	Size (nm)
Al-added ODSS	0 %	NOHT	1.6	275	8.4 x 10 ²¹	11
	0 %	1350 °C	230	204	1.9 x 10 ²¹	23
	20 %	1350 °C	24	222	1.1 x 10 ²¹	22
	80 %	850 °C	19	267	8.3 x 10 ²¹	11
Al-free ODSS	0 %	NOHT	0.96	395	5.4 x 10 ²²	4
	0 %	1400 °C	1.3	237	2.3 x 10 ²¹	19
	80 %	1250 °C	2.70	328	1.6 x 10 ²²	8

According to Orowan type strengthening mechanism proposed by several researchers, it can be considered that there are a few equations expressing Orowan stress. The basic Orowan type strengthening can be estimated as,

$$\sigma_{OR} = M\alpha\mu b/\lambda \quad (4.9)$$

λ is the spacing between impenetrable obstacles as shown Fig. 4-10. It can be expressed approximately by square-shaped array area as equation (4.2), which involves oxide particles distribution morphology (Fig. 4-11).

Orowan type strengthening expression can be modified to the following formula,

$$\sigma_{OR} = \frac{0.83 \cdot M\alpha\mu b}{2\pi \cdot (\lambda - d) \cdot (1 - \nu)^{0.5}} \cdot \ln\left(\frac{d}{2b}\right) \quad (4.10)$$

ν is Poisson's ratio of matrix, which is 0.334 in this study. Also, the dislocation morphologies in materials are considered, 0.83 is constant when dislocations types such as screw and edge dislocation are distributed randomly in matrix.

Fig. 4-12 shows the contributions to the strengthening with each equation a) 4.9, b) 4.2 and c) 4.10, respectively. The Orowan type strengthening of (a) and (b) are similar each other and it is almost a half of total strength of ODS steels. In contrast to this, (c) shows lower Orowan type strengthening and it is not remarkably changed with oxide particles distribution morphology. (d), (e) and (f) show the strengthening contribution to each mechanism. The matrix strength is assumed from σ_0 of Hall-Petch plot in SUS 430. It is about 60Hv.

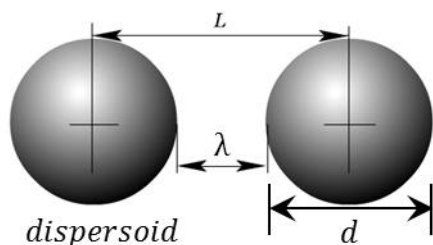


Figure 4-10 The schematic diagram of each factors between dispersoids

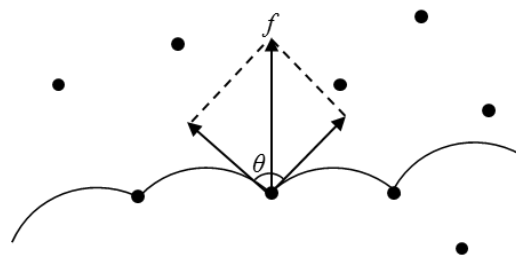


Figure 4-11 Orowan type strengthening with considering of the relationship between dispersed oxide particles and dislocation migrations

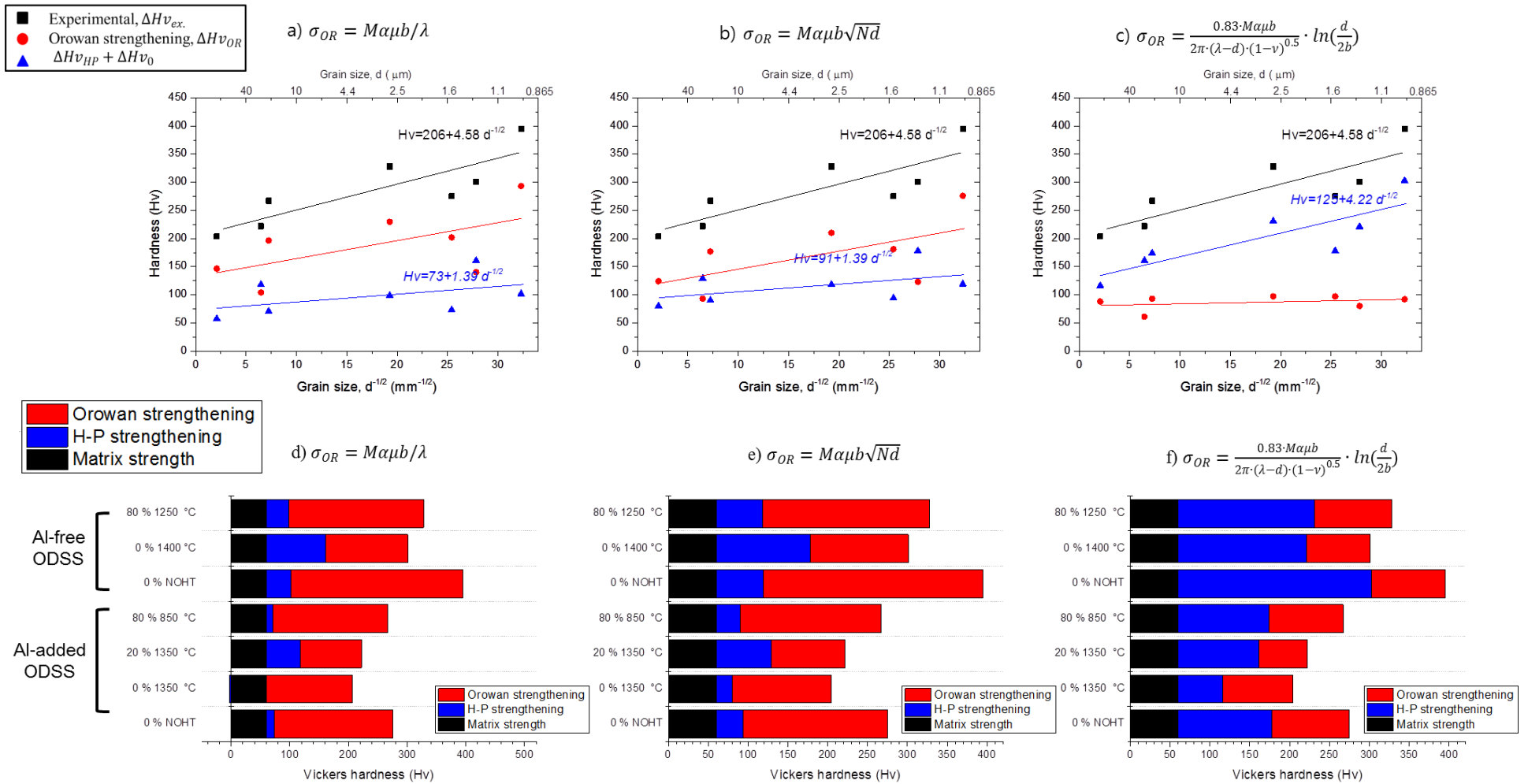


Figure 4-12 Factors controlling strengthening calculated Orowan type strengthening (a) $\sigma_{OR} = M\alpha\mu b/\lambda$, (b) $\sigma_{OR} = M\alpha\mu b\sqrt{Nd}$, (c) $\sigma_{OR} = \frac{0.83 \cdot M\alpha\mu b}{2\pi \cdot (\lambda-d) \cdot (1-\nu)^{0.5}} \cdot \ln\left(\frac{d}{2b}\right)$

The results of Orowan type strengthening from equation a) 4.9 and b) 4.2 are more reasonable than that of equation c) 4.10. Since the dispersed particles impact on matrix strength, the oxide particles distribution morphology is most important for controlling strengthening of ODS steels, and also the grain boundary strengthening is applied as the other strengthening.

Fig. 4-13 shows the Vickers hardness indentations on the specimen surface after annealing at 1350 °C in Al-added ODS steel. The hardness is not much different between internal grain and grain boundary. Therefore, it is suggested that the grain boundary strengthening is not significant any more after remarkable recrystallization, although it has still a strengthening effect on the matrix. It is considered that the hardness of ODS steels are mainly determined by not grain size but oxide particles dispersed in the matrix.

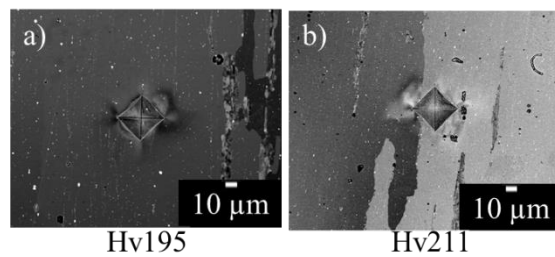


Figure 4-13 Vickers hardness and indentation on surface (a) inside grain and (b) grain boundary

4.4 Summary

The strengthening factors affecting on mechanical properties are investigated and discussed for ODS steels before and after annealing processing, that is, recrystallization treatment. The results obtained are summarized as follows;

- 1) The hardness of ODS steel is not fitted to a single Hall-Petch plot, indicating that grain boundary strengthening mechanism is not only the factor controlling strength of ODS steels. The slope of the fitting line depends on the steel compositions. There is a significant difference in the slope of the H-P relation between Al-free and Al-added ODS steels because the addition of Al causes the changes in the oxide particles distribution morphology such as the size and number density of oxide particles.
- 2) The data deviation from the H-P line of Vickers hardness measurement tends to be reduced by the subtraction of Orowan contribution. Since oxide particle dispersion morphology as well as grain size is changed by recrystallization treatment, it is considered that the data deviation is due to the contribution change of Orowan strengthening.
- 3) In ODS steels, the dispersion strengthening is dominant. Orowan type strengthening of Al-free ODS steel is larger than that of Al-added ODS steel, because the oxide particles are finer with higher number density in Al-free ODS steel and they are more stable at elevated temperatures. The large particles in both ODS steels play a role as obstacle to dislocation motion.
- 4) The evaluation results by several Orowan equations revealed that using the equation, $\sigma_{OR} = M\alpha ub\sqrt{Nd}$, the obtained value of Orowan type strengthening is most reasonable.
- 5) Finally, the Hall-Petch relationship is not unique for ODS steels, which is considered to be due to the difference in the oxide particle distribution morphology that changes the contribution to the strength of ODS steels.

References

1. J.H. Schneibel, M. Heilmaier, W. Blum, G. Hasemann, T. Shanmugasundaram, "Temperature dependence of the strength of fine- and ultrafine-grained materials", *Acta Mater.*, **59** (2011) 1300-1308
2. E.O. Hall, "The Deformation and Ageing of Mild Steel: III Discussion of Results", *Proc. Phys. Soc. London*, **B64** (1951) 747-753
3. N. J. Petch, "The Cleavage Strength of Polycrystals", *J. Iron Steel Inst.*, **174** (1953) 25-28
4. M.A. Muñoz-Morris, C. Garcia Oca, D.G. Morris, "An analysis of strengthening mechanisms in a mechanically alloyed, oxide dispersion strengthened iron aluminide intermetallic", *Acta Mater.*, **50** (2002) 2825-2836
5. G.E. Fougere, J.R. Weertman, R.W. Siegel, S. Kim, "GRAIN-SIZE DEPENDENT HARDENING AND SOFTENING OF NANOCRYSTALLINE Cu AND Pd", *Scripta Metall. Mater.*, **26** (1992) 1879-1883
6. J. R. Weertman, "Hall-Petch strengthening in nanocrystalline metals", *Mater. Sci. Eng. A*, **166** (1993) 161-167
7. P.K.C. Venkatsurya, Z.Jia, R.D.K.Misra, M.D.Mulholland, M.Manohar, J.E.HartmannJr., "Understanding mechanical property anisotropy in high strength niobium-microalloyed line pipe steels", *Mater. Sci. Eng. A*, **556** (2012) 194-210
8. P. Krautwasser, A. Czyrska-Filemonowicz, M. Widera, F. Carsughi, "Thermal stability of dispersoids in ferritic oxide-dispersion strengthened alloys", *Mater. Sci. Eng. A*, **177** (1994) 199-208
9. P. Dou, A. Kimura, T. Okuda, M. Inoue, S. Ukai, S. Ohnuki, T. Fujisawa, F. Abe, "Polymorphic and coherency transition of Y–Al complex oxide particles with extrusion temperature in an Al-alloyed high-Cr oxide dispersion strengthened ferritic steel", *Acta Mater.*, **59** (2011) 992-1002
10. Peng Dou, Akihiko Kimura, Takanari Okuda, Masaki Inoue, Shigeharu Ukai, Somei Ohnuki, Toshiharu Fujisawa, Fujio Abe, "Effects of extrusion temperature on the nano-mesoscopic structure and mechanical properties of an Al-alloyed high-Cr ODS ferritic steel", *J. Nucl. Mater.*, **417** (2011) 166-170

11. C. Garcia Oca, M.A. Muñoz-Morris, D.G. Morris, "High temperature structural coarsening of an ODS FeAl intermetallic", *Intermetallics*, **11** (2003) 425-434
12. A. Czyrska-Filemonowicz, K. Szot, A. Wasilkowska, A. Gil, W.J. Quadackers, "Microscopy (AFM, TEM, SEM) studies of oxide scale formation on FeCrAl based ODS alloys", *Solid state ionics*, **117** (1999) 13-20
13. Jerome Isselin, Ryuta Kasada, Akihiko Kimura, Takanari Okuda, Masaki Inoue, Shigeharu Ukai, Somei Ohnuki, Toshiharu Fujisawa, Fujio Abe, "Effects of Zr Addition on the Microstructure of 14%Cr4%Al ODS Ferritic Steels", *Mater. Trans.*, **51** (2010) 1011-1015
14. R. Gao, T. Zhang, X.P. Wang, Q.F. Fang, C.S. Liu, "Effect of zirconium addition on the microstructure and mechanical properties of ODS ferritic steels containing aluminum", *J. Nucl. Mater.*, **444** (2014) 462-468
15. Luke L. Hsiung, "HRTEM Study of Oxide Nanoparticles in Fe-16Cr ODS Ferritic Steel Developed for Fusion Energy", *Microscopy: Science, Technology, Applications and Education*, (2010) 1811-1819
16. R. Kasada, N. Toda, K. Yutani, H.S. Cho, H. Kishimoto, A. Kimura, "Pre- and post-deformation microstructures of oxide dispersion strengthened ferritic steels", *J. Nucl. Mater.*, **367-370** (2007) 222-228
17. A. Kimura, R. Kasada, N. Iwata, H. Kishimoto, C.H. Zhang, J. Isselin, P. Dou, J.H. Lee, N. Muthukumar, T. Okuda, M. Inoue, S. Ukai, S. Ohnuki, T. Fujisawa, T. F. Abe, "Super ODS Steels R&D for Fuel Cladding of Next Generation Nuclear Systems 1) Introduction and alloy design", *Proceedings of ICAPP'09*, **9220** (2009) 1-8
18. P.M. Hazzledine, "DIRECT VERSUS INDIRECT DISPERSION HARDENING", *Scripta Metall. Mater.*, **26** (1992) 57-58
19. Joachim H. Schneibel, Martin Heilmaier, "Hall-Petch Breakdown at Elevated Temperatures", *Mater. Trans.*, **55** (2014) 44-51
20. D.G. Morris, M.A. Muñoz-Morris, "Nanoprecipitation of oxide particles and related high strength in oxide-dispersion-strengthened iron–aluminium–chromium intermetallics", *Acta Mater.*, **61** (2013) 4636-4647
21. M. Klimiankou, R. Lindau, A Möslang, "TEM characterization of structure and composition of nanosized ODS particles in reduced activation ferritic–martensitic steels", *J. Nucl. Mater.*, **329-333** (2004) 347-351

22. Lev Ivanovich Ivanov, Yu M. Platov, "Radiation Physics of Metals and Its Applications", *Cambridge Int Science Publishing* (2004)
23. Jeremy T. Busby, Mark C. Hash, Gary S. Was, "The relationship between hardness and yield stress in irradiated austenitic and ferritic steels", *J. Nucl. Mater.*, **336** (2005) 267-278
24. E.J. Pavlina, C.J. Van Tyne, "Correlation of Yield Strength and Tensile Strength with Hardness for Steels", *J. Mater. Eng. Perform.*, **17** (2008) 888-893

Chapter 5

Ion-irradiation Effects on ODS Ferritic Steels

5.1 Introduction

The excellent irradiation tolerance of ODS steel is caused by not only oxide dispersion morphologies (size distribution, number density, volume fraction and inter-spacing) but also fine grains providing large grain boundary area. These fine microstructures in ODS steels effectively trap radiation defects and helium atoms at the interfaces of metal/oxide and grain boundaries, and intensively suppress defect clustering by enhancing self-interstitial atom-vacancy recombination mechanism.

Irradiation damage management of structural material is important for safety and economically competitive energy source of nuclear fusion and fission systems, and irradiation experiments of materials have been performed using reactor irradiation with neutron. However, neutron irradiation needs long period and high costs. International fusion materials irradiation facility (IFMIF) project is still on the way to the final engineering design, and fission neutron and charged particle irradiation facilities are just few available for advanced material experiment. Therefore, the ion-irradiation test, which can be irradiated by heavy ions or simultaneous heavy ions and helium ions is actively carried out for the advanced material analysis. So, the ion-irradiation experiment is performed in this research. The (n, α) nuclear reaction by 14 MeV fast neutron produces helium, while heavy-ion irradiation produces cascade damage similar to 14 MeV fast neutron irradiation [1]. The simultaneous irradiation of heavy and helium ions is able to investigate the synergistic effects of cascade damages and helium.

It is expected that recrystallization causes grain growth which results in a significant reduction of trapping site for irradiation damage structures. Unfortunately, however, the effect of recrystallization on irradiation performance was not investigated in detail, although many researches on the effect of oxide particle morphologies on irradiation behavior of ODS steels have been done. In this research, the effect of recrystallization on ion-irradiation effects in 15Cr-ODS ferritic steels is investigated to clear the role of not only oxide particles but also grain boundaries on the irradiation hardening and microstructure evolution.

5.2 Experimental procedure

5.2.1. The preparation of irradiated material

The materials used in this study were Al-added ODS steel and Al-free ODS steel in order to compare the irradiation effect between the steels with different recrystallization behavior. The chemical compositions of Al-added and free ODS steel is same as shown Table 2-1. There are three categories of specimen: (1) as received material (before annealing). To investigate the effect of annealing or grain size on irradiation effects, the materials are (2) annealed at 1350 °C and 1400 °C for Al-added and Al-free ODS steel for 1 hour, respectively. The annealing processing was carried out using hot press machine. Also, the specimens are (3) cold rolled to about 20 % reduction ratio after the above annealing. Table 5-1 shows the grain size and oxide particle information obtained in the above chapters.

As the damaged region is confined to the surface area induced by ion-beam (~2 μm) in ion-irradiation test, the surface condition is very important to acquire accurate irradiation area. After annealing (or annealing and cold rolling with 20 % reduction ratio), the specimens were mechanically grinded with #800, #1200, #2400 and #4000 emery SiC papers. And then they were buff-polished with diamond paste of 6, 3, 1, 0.25 μm diameter. Finally, the electrolytic polishing in a solution of 5 vol. % perchloric acid and 95 vol. % methanol was performed at 18 V for 2~3 seconds at -50 °C added with liquid nitrogen to remove the damaged surface layer resulting from mechanical polishing [1-3].

Table 5-1 Size and number density of each factor before and after annealing

Annealing condition	Al-added ODS steel		Al-free ODS steel	
	Before	After	Before	After
Grain diameter	1.6 μm	230 μm	1.0 μm	1.3 μm
Oxide particle (OP) diameter	11 nm	23 nm	4 nm	19 nm
Number density of OP	$8.4 \times 10^{21} \text{ m}^{-3}$	$1.9 \times 10^{21} \text{ m}^{-3}$	$5.4 \times 10^{22} \text{ m}^{-3}$	$1.6 \times 10^{22} \text{ m}^{-3}$

5.2.2. Ion irradiation experimental method

5.2.2.1 Ion-irradiation accelerator

Ion-irradiation experiment is performed with dual-beam irradiation experimental test facility (DuET) at Institute of Advanced Energy, Kyoto University [1~7]. DuET facility is designed to provide the irradiation conditions simulating fusion reactor environments, where high displacement damages and high concentration of transmutation helium atoms are produced (Fig. 5-1).

The facility consists of two accelerators [8], 1.7MeV tandem and 1MeV single-end accelerator, and three target chambers. Model 4117HC tandem accelerator, which is Cockcroft Walton type manufactured by High Voltage Engineering Europe, B. V. (HVEE) is used for heavy ion irradiation such as Si, Fe, Ni and so on. The vacuum condition is 5×10^{-5} Pa at tube inside and it can be holding by tow turbo molecular pumps. The tandem accelerator has an HVEE Model 860A cesium sputter-type heavy ion source and a model 358 duoplasmatron-type light ion source. The self-ion, Fe ion for steels, was selected to minimize the effects of heavy ion implantation. The induced negative ions from an ion source are changed into positive ions at the middle of the tube and accelerated.

The Singletron single-end accelerator, manufactured HVEE, has a Model SO-173 RF type light ion source. Single-charged helium ions are accelerated up to 1.0 MeV with current as large as 1 mA with these two accelerators, very high dose dual-beam irradiation to the material with self-ions becomes possible.



Figure 5-1 DuET facility in IAE, Kyoto University

The dual-ion beam irradiation target chamber is called DuMIS (Dual-beam materials irradiation station) as shown in Fig. 5-2. The chamber is connected to dual-beam line, which are designed to cross the surface of a specimen holder. The station consists of a target support assembly with specimen loading port, two faraday cup arrays, an infrared heating system, a beam energy degrader, three vacuum systems and so on. Other target chambers are called high-temperature materials analysis station (HiMAS) and single-beam tensile irradiation creep station (STICS), respectively. DuMIS is only used in this study.

The irradiation temperature is controlled by ultrahigh infrared ray radiation (IR) heating and water cooled system, GVH298 as heating system of DuMIS. Heating emitted infrared radiations on the atmosphere side is introduced into an ultrahigh vacuum and continuous irradiation experiments can be carried out without breaking the vacuum. Controlled irradiation temperature from this system is measured the specimen surface using a thermography, LAIRD3ASH (Nikon. Co.). The measured temperature data is transported to the computer in the control room and monitored during irradiation experiment. The temperature is controlled error range ± 10 °C from target temperature.

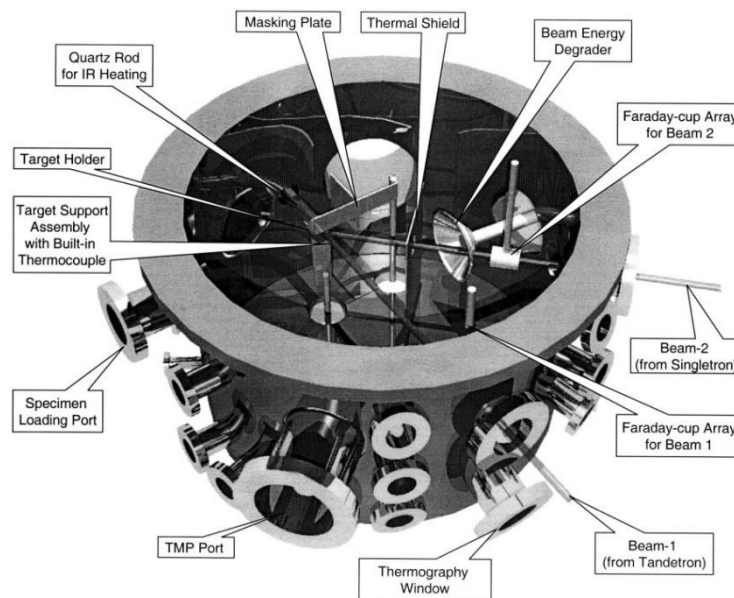


Figure 5-2 Dual-beam materials irradiation station [8]

5.2.2.2 Ion irradiation area

The depth profiles of the displacement damage and the implanted helium for ion irradiations can be calculated by TRIM code [9] which can be estimated the stopping and range of ions in matter. Fig. 5-3 shows the result from TRIM code which expresses the helium injection rate and displacement damage. The nominal displacement per atom (dpa) is defined as the displacement damage occurring at the depth of 600 nm from the irradiated surface. Because the surface area or near the surface performed strong surface sink. While, the peak area for damage displacement is contained the large dpa gradient, that is difficult to investigate the microstructure for irradiation effect. For this reason,

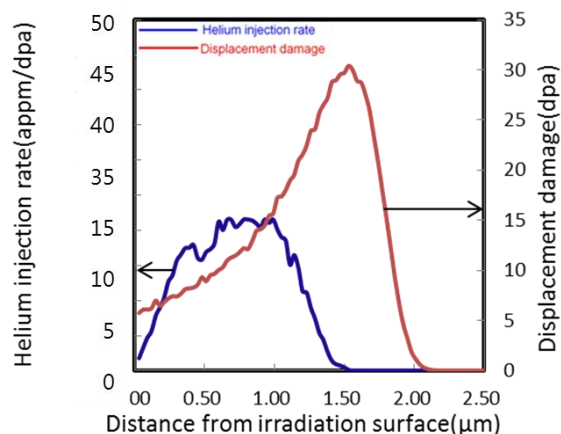


Figure 5-3 Depth profiles of the displacement damage and the implanted helium by TRIM code

the depth of 600 nm is selected for nominal dpa with small dpa gradient and reduced effect of the

surface sink. The implanted helium range was between 200 and 1500 nm depth from the specimen surface. The implanted and energy degraded helium ions were widely overlapped in the damaged range due to heavy-ion irradiation. The synergistic effects of displacement damages and helium can be investigated from the microstructural behaviors in the overlapped range [1].

Table 5-2 Irradiation condition

Damage at 600 nm	Ion type	Temperature	He injection
10 dpa	1.7MV, Fe ³⁺	300 °C	0 appm
10 dpa	1.7MV, Fe ³⁺ 1MV, He ⁺	300 °C	150 appm
30 dpa	1.7MV, Fe ³⁺	470 °C	0 appm
30 dpa	1.7MV, Fe ³⁺ 1MV, He ⁺	470 °C	450 appm

Table 5-2 shows the irradiation conditions, that is dose of nominal damage, type of ion from accelerator, irradiation temperature and nominal concentration of helium. Single-ion irradiations used 1.7MV Fe³⁺. Dual-ion irradiation is used 1.7MV Fe³⁺ ions for displacement damage simultaneously with energy-degraded 1.0 MV He⁺ ions. The value of nominal dose rate is 4×10^{-4} dpa/s.

5.2.3. Hardness measurement by Nano-indentation

5.2.3.1 Nano-indentation hardness

Irradiation hardening or the embrittlement in irradiated material is essential to evaluate after heavy ion irradiation techniques. Because the irradiation damage is quite limited in few micrometers from irradiated surface, the hardening is usually measured by nano-indentation equipment alternatively [10].

In this study, the nano-indentation test is carried out the irradiation surface of each specimen using G200 of Nano Indenter (Agilent Technologies Inc.) with Berkovich type indentation tip, which have 65 ° between the indentation direction and indented surface. The indentation schematic design is in Fig. 5-4 (a). The constant stiffness measurement (CSM) technique was used to obtain the hardness by the depth profile of material. The depth of nano-indentation is measured about 2000 nm. The CSM has a great advantage to obtain the depth profile only with a one indent compared with the loading-unloading method [5, 11]. The obtained results showed the depth-dependence of irradiation hardening. Thus, in spite of the importance of nano-indentation tests on the ion-irradiated materials for fusion reactors, little attention was given to the hardness depth-profile obtained from the ion irradiated surface. A clear understanding of the hardness depth profile of ion-irradiated material and its connection to the “bulk” mechanical properties is important for further application of the nano-indentation techniques.

R. Kasada et al. [10] proposed a modified nano-hardness measurement technique to measure ion irradiation hardening. The calibration of the bluntness of the indentation tip is based on the Oliver–Pharr method [4, 5, 7, 10, 12-15]. The effects of non-rigid indenters on the load-displacement behavior can be effectively accounted for by defining a reduced modulus, E_r , through the equation,

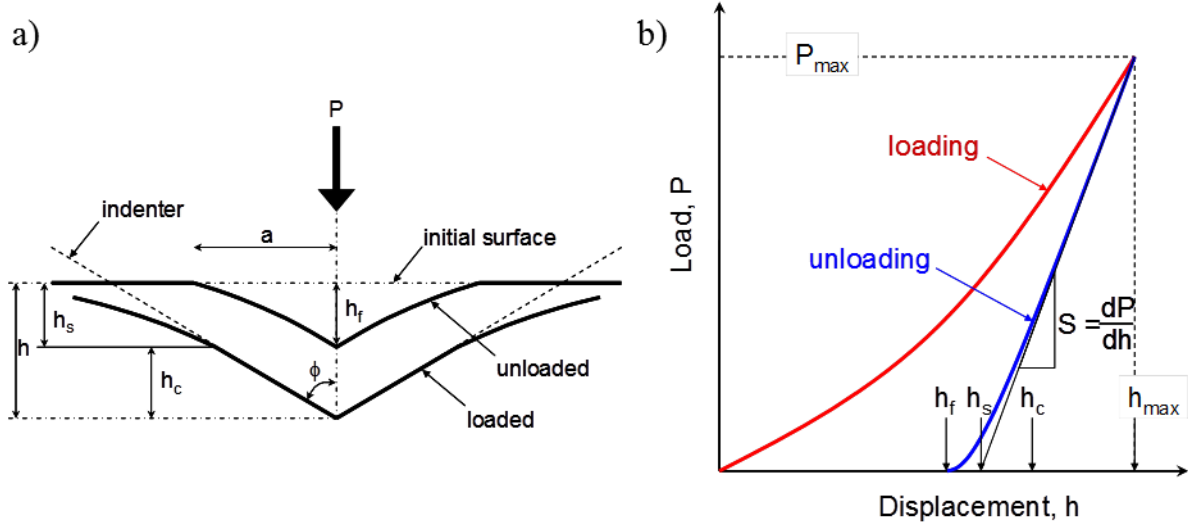


Figure 5-4 A schematic of (a) section of indentation, (b) load versus indenter displacement [14]

$$\frac{1}{E_r} = \frac{(1-\nu^2)}{E} + \frac{(1-\nu_i^2)}{E_i} \quad (5.1)$$

where E and ν are Young's modulus and Poisson's ratio for the specimen, respectively, and E_i and ν_i are the same parameters for the indenter. The hardness can be obtained indentation load-displacement data like that shown schematically in Fig. 5-4 (b), and analyzed according to the equation,

$$S = \frac{dP}{dh} = \frac{2}{\sqrt{\pi}} \cdot E_r \sqrt{A} \quad (5.2)$$

$S = dP/dh$ is the experimentally measured stiffness of the upper portion of the unloading data and A is the projected area of the elastic contact.

Meanwhile, the area of contact at peak load is determined by the geometry of indenter when the depth of contact, h_c . It is assumed that the indenter geometry can be described by an area function $F(h)$, which relates the cross-sectional area of the indenter to the distance from the tip, h . Hence, the projected contact area function at peak load, A and h_c can be expressed,

$$A(h_c) = 3\sqrt{3} \cdot \tan^2 65^\circ \times h_c^2 = 24.5h_c^2 \quad (5.3)$$

Also, h_c can be indicated the interaction formula between maximum depth, h_{max} and an intersection point of loading gradient, h_s as the equation,

$$h_c = h_{max} - \varepsilon \frac{P_{max}}{S} = h_{max} - 0.75(h_{max} - h_s) \quad (5.4)$$

ε is geometric constant of indenter condition, as $\varepsilon=0.75$ in case of Berkovich type.

It is defined that the hardness as the mean pressure for material will support under load. With this definition, the hardness is calculated as

$$H = \frac{P_{max}}{A} \quad (5.5)$$

The indentation measurement is performed at least 15 times for each specimen and loading rate is 0.05 S^{-1} in this research.

5.2.3.2 Nix-Gao Model analysis of hardness by nano-indenter

The increase in hardness with decreasing indent size or depth as called indentation size effect (ISE) was informed in several results of nano-indentation test [4, 5, 7, 10, 16]. Nix and Gao developed a model based on a concept of geometrically necessary dislocation (GNDs), that is dislocations that must be present near the indentation to accommodate the volume of material displaced by the indenter at the surface [16, 17]. Using the Nix-Gao model, the hardness depth profile is given as follows,

$$H = H_0 \sqrt{1 + \left(\frac{h^*}{h}\right)^2} \quad (5.6)$$

where H is the hardness for a given depth of indentation, h , H_0 is the hardness in the limit of infinite depth (the bulk hardness) and h^* is a characteristic length that depends on the shape of the indenter, the shear modulus and H_0 .

Fig. 5-5 shows the conceptual diagram of “geometrically necessary dislocations” during indentation. In the Nix-Gao model, the indenter is assumed to be a rigid cone whose self-similar geometry is defined by the angle, θ , between the indenter and the undeformed surface. It is defined that the contact radius to be a and the depth of indentation to be h . Suppose the individual dislocation loops as being spaced equally along the surface of the indentation, it can be expressed as follow,

$$\tan \theta = \frac{h}{a} = \frac{b}{s}, s = \frac{ba}{h} \quad (5.7)$$

where s is the spacing between individual slip steps on the indentation surface. If λ is the total length of the injected loops, and r is distance from center of indenter, then between r and $r + dr$ we have

$$d\lambda = 2\pi r \frac{dr}{s} = 2\pi r \frac{h}{ba} dr \quad (5.8)$$

which after integration gives,

$$\lambda = \int_0^a \frac{h}{ba} 2\pi r dr = \frac{\pi ha}{b} \quad (5.9)$$

If, all of the injected loops remain within the hemispherical volume V defined by the contact radius,

$$V = \frac{2}{3} \pi a^3 \quad (5.10)$$

so that the density of geometrically necessary dislocations, ρ_G becomes

$$\rho_G = \frac{\lambda}{V} = \frac{3h}{2ba^2} = \frac{3}{2bh} \tan^2 \theta \quad (5.11)$$

Taylor relation is used for shear strength to estimate the deformation resistance as follows,

$$\tau = \alpha \mu b \sqrt{\rho_T} = \alpha \mu b \sqrt{\rho_S + \rho_G} \quad (5.12)$$

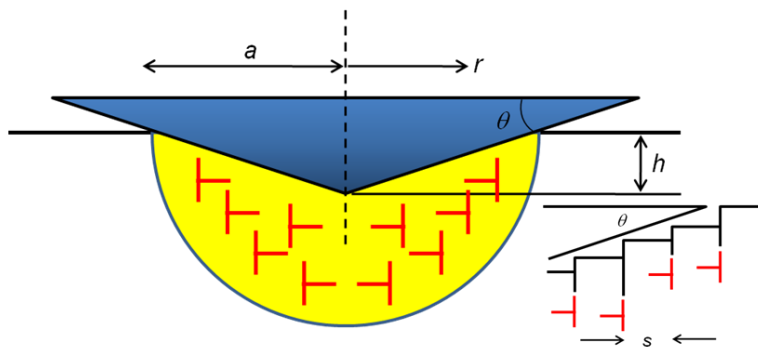


Figure 5-5 The conceptual diagram of geometrically necessary dislocations [18]

the total dislocation density is the simple mathematical sum of the geometrically necessary part, ρ_G , and the statistically stored dislocations (SSDs), ρ_S , which is not expected to depend on the depth of indentation, but depends on the average strain in the indentation as shape of the indenter. μ is the shear modulus, b is the Burgers vector and α is a constant to be taken as 0.5.

The von Mises flow rule applies and that Tabor's factor of 3 can be used to convert the equivalent flow stress to hardness,

$$\sigma = \sqrt{3}\tau, H = 3\sigma \quad (5.13)$$

Using the eqns. (11) ~ (13), eqns. (6) can be obtained. In here,

$$H_0 = 3\sqrt{3}\alpha\mu b\sqrt{\rho_S} \quad (5.14)$$

is the hardness that would arise from the statistically stored dislocations alone, in the absence of any geometrically necessary dislocations, and a characteristic length h^* can be obtained.

$$h^* = \frac{81}{2}b\alpha^2\tan^2\theta\left(\frac{\mu}{H_0}\right)^2 \quad (5.15)$$

5.2.4. Microstructure observation

Small specimens for TEM observation were sampled by Focus Ion Beam (FIB) system because the irradiated region is limited to the surface of 2 μm depth. Specimens were cut by the gallium (Ga) focused ion beam in high vacuum condition. Tungsten was deposited to prevent the specimen surface from damaging by focused ion beam. FB-2200, Hitachi is used as FIB instrument. After fabricating specimen by FIB system, the specimen was finally polished with Nano-mill system (Model 1040, Fischione Instruments, Inc.), which removed the damaged region by FIB treatment. The microstructure change by ion irradiation is observed by TEM (JEM-2010, JEOL Co.) with an acceleration voltage of 200 kV.

5.3 Results and discussions

5.3.1 Irradiation effect at 300 °C to 10 dpa

5.3.1.1 Al-added ODS steel

Fig. 5-6 shows the depth profile of hardness after single ion irradiation up to 10 dpa at 300 °C in Al-added ODS steel. Fig. 5-6 (a) is as-received, (b) is annealed at 1350 °C and (c) is 20 % cold rolled after annealing at 1350 °C. Among the hardness depth profiles of unirradiated specimens (black lines), the hardness of (b) annealed specimen at 1350 °C is lowest, which agrees with Vickers hardness test results in Chapter 2 and caused by recrystallization. The hardness of (c) 20 % cold rolled specimen after recrystallization is increased again.

The hardness after irradiation at 300 °C to 10 dpa, marked red line, is higher than that of before irradiation in all the cases. It seems that the hardening is remarkably larger in the range from 50 nm to 600 nm (enlarged for this range in the right side up). Also the irradiation hardening is smaller in the case of 20 % cold rolled specimen after recrystallization.

The increase in hardness with decreasing indent depth is observed in all specimens and also both unirradiated and irradiated area. Thus, as expected, ISE (indentation size effect) was observed in this experiment.

From the above results, the hardness data is converted into the plots of Nix-Gao model as shown as the H^2 versus $1/h$ plots in Fig. 5-7. The hardness data of unirradiated specimens have a line shape in the range above 100 nm (0.010 nm^{-1}) in all cases. However, the hardness data of irradiated specimens have a bi-linearity with a shoulder at around from 200 nm to 400 nm. As reported in the previous study [5, 10], the bi-linear behavior is due to the softer substrate effect (SSE) of the duplication of the hardness of irradiated region and unirradiated one just beneath the irradiated region. Such behavior was also found in the hardness measurement of unirradiated tungsten by the CSM [19]. However, it is clear that the bilinear behavior in the ion-irradiated ODS steels is due to SSE and not artificial effect in the CSM.

The hardness is the highest in (a) as-received specimen, meanwhile the irradiation hardening is higher in case of (a) as-received and (b) recrystallized specimen.

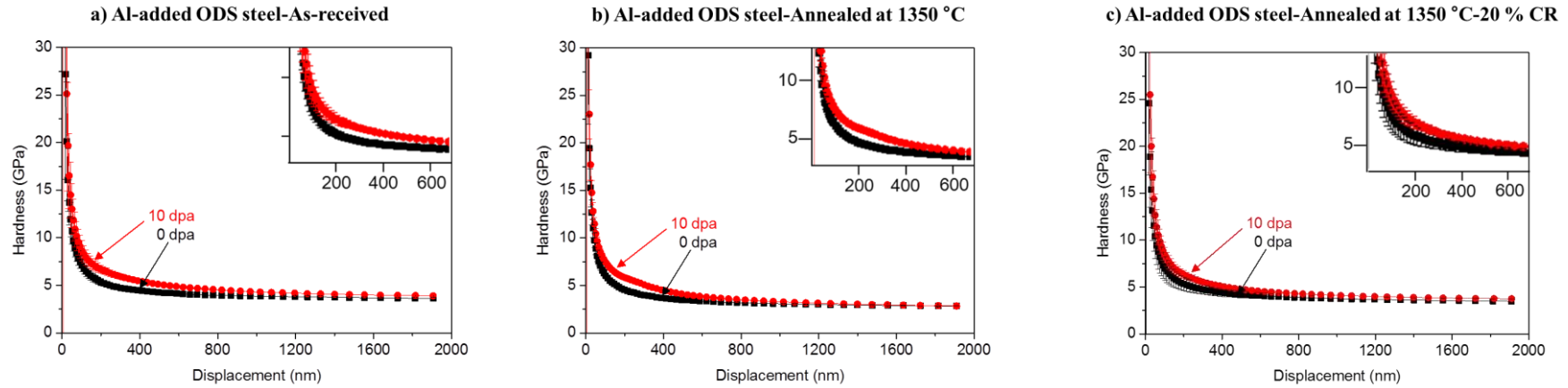


Figure 5-6 The depth profile of hardness after single ion irradiation up to 10 dpa at 300 °C in Al-added ODS steel

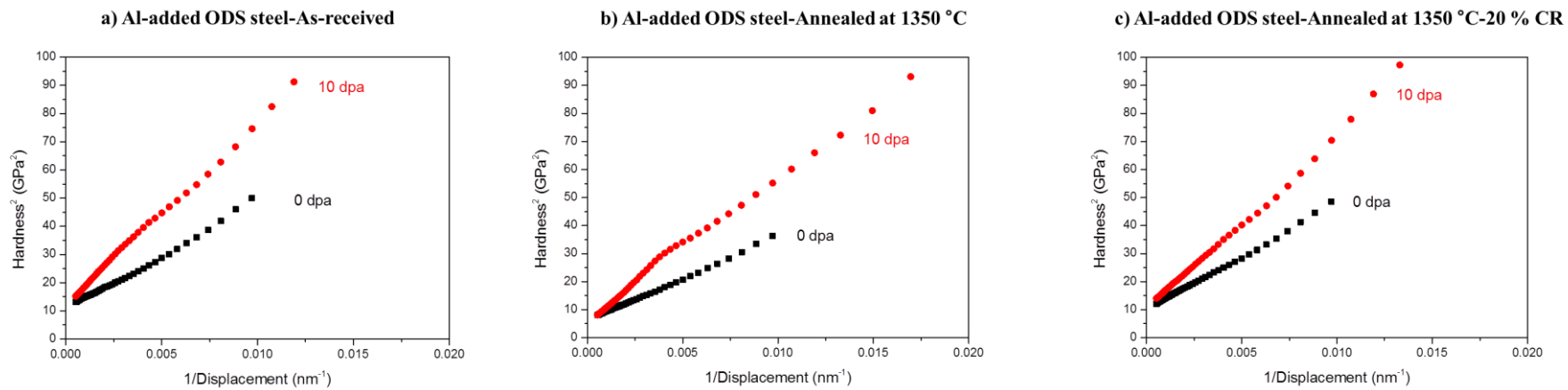


Figure 5-7 Nix-Gao plotted H^2 versus $1/h$ after single ion irradiation up to 10 dpa at 300 °C in Al-added ODS steels

Fig. 5-8 shows the depth profile of irradiation hardening after irradiation up to 10 dpa at 300 °C in Al-added ODS steels. The hardening is gradually reduced with indentation depth. H_{irr} and H_{unirr} were the hardness of each specimen before and after ion irradiation, respectively. The hardening appears to be reduced a little after recrystallized specimen (red column) compared with as-received specimen (black column). It seems that the effect of annealing on the irradiation hardening at 10 dpa at 300 °C is not significant, even the microstructure changes such as grain boundary area, dislocation density and oxide particle size and number density were observed. The hardness change is lowest in 20 % cold rolled specimen after recrystallization.

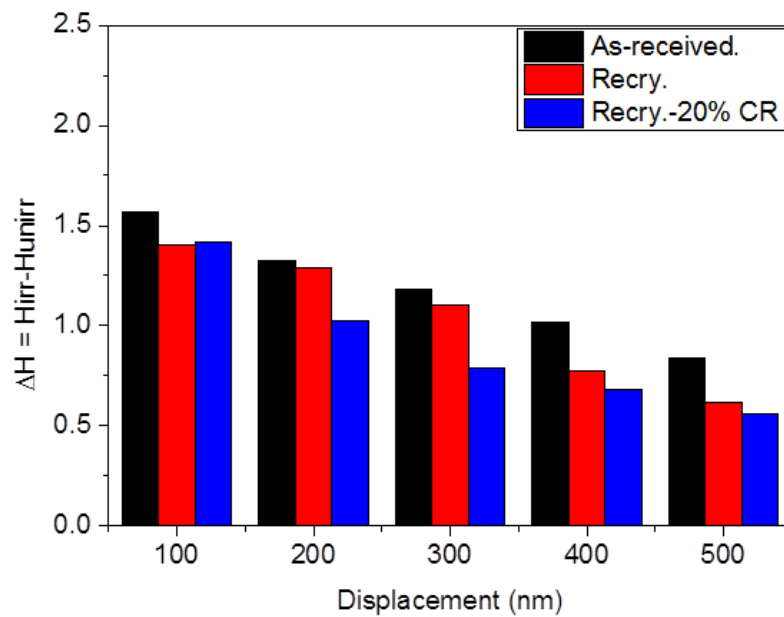


Figure 5-8 The depth profile of irradiation hardening after irradiation up to 10 dpa at 300 °C in Al-added ODS steels

5.3.1.2 Al-free ODS steel

Fig. 5-9 shows the depth profile of hardness after single and dual ion irradiation up to 10 dpa at 300 °C in Al-free ODS steel. The hardness of irradiated area is higher than that of unirradiated one. In addition, the hardness after dual-ion irradiation is higher than that of single-ion irradiation in all cases. The hardness is lowest in the annealed specimen at 1400 °C. It is suggested that dislocations were annealed out by the heat treatment. Fig. 5-10 shows the Nix-Gao plots of H^2 versus $1/h$ after single and dual ion irradiation up to 10 dpa at 300 °C in Al-free ODS steels. It can be seen that a significant increase in the hardening was observed for the case of the dual-ion irradiation.

Fig. 5-11 shows the hardening by (a) single-ion and (b) dual-ion. In single-ion irradiation, the hardening is the highest in case of 20 % cold rolled specimen after cold rolling. The annealed specimen shows the smallest hardening.

The hardening by dual-ion irradiation is remarkably higher than the hardening by single-ion irradiation. It is noticed that the scale bar of Y axis is different from the result of the hardening by single-ion irradiation. At each depth the trend of the hardening is same although the amount of hardening depends on the depth. Another difference is that the hardening of annealed specimen is highest after dual-ion irradiation.

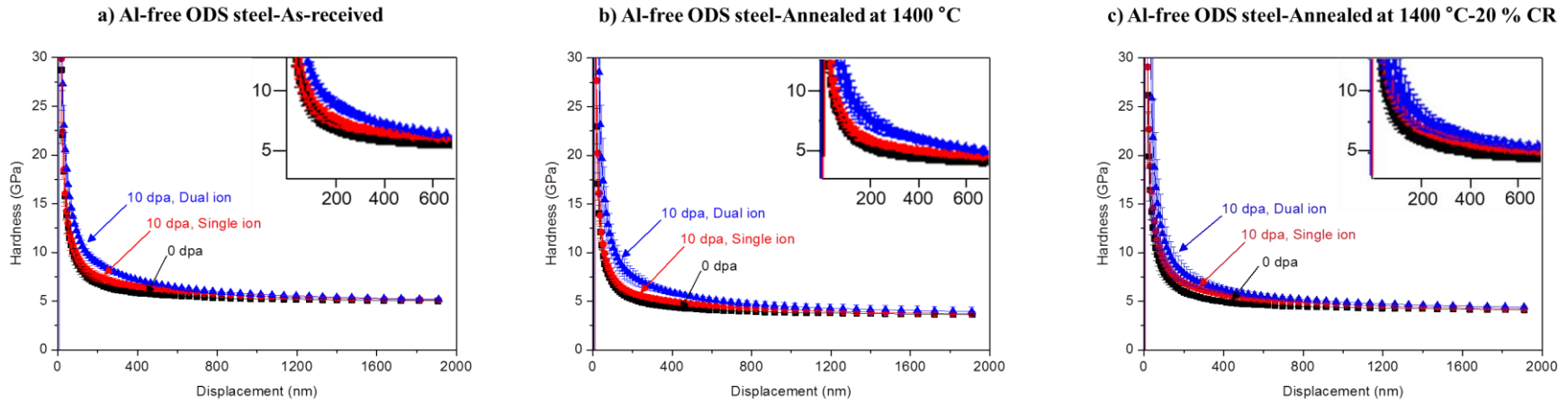


Figure 5-9 The depth profile of hardness after single and dual ion irradiation up to 10 dpa at 300 °C in Al-free ODS steel

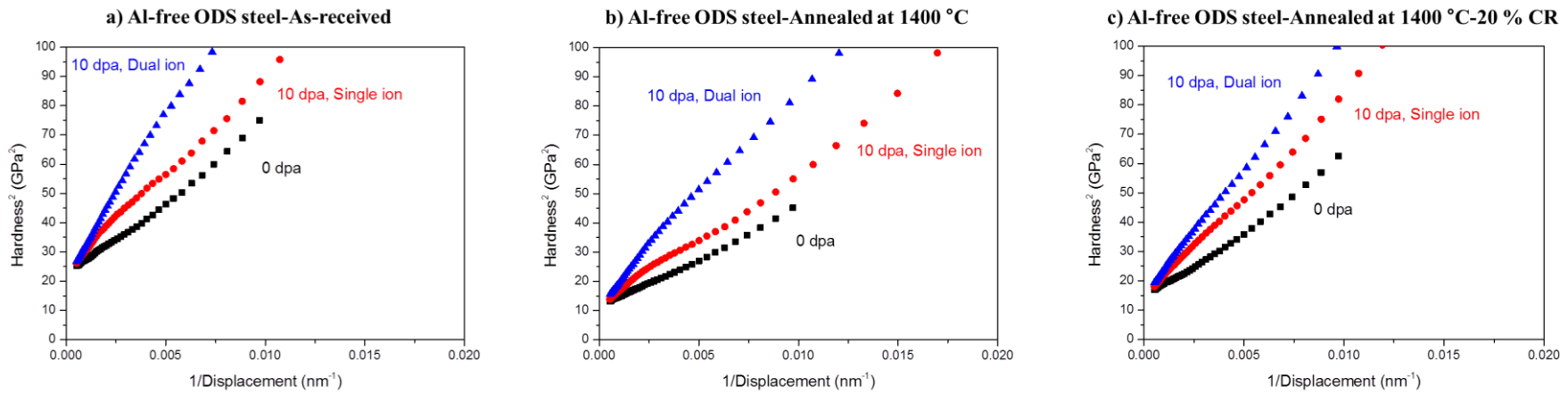
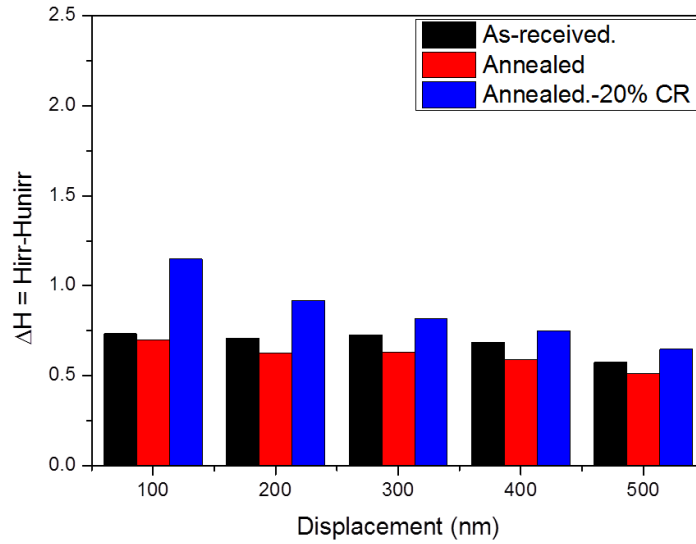


Figure 5-10 Nix-Gao plotted H^2 versus $1/h$ after single and dual ion irradiation up to 10 dpa at 300 °C in Al-free ODS steels

a) Single ion irradiation



b) Dual ion irradiation

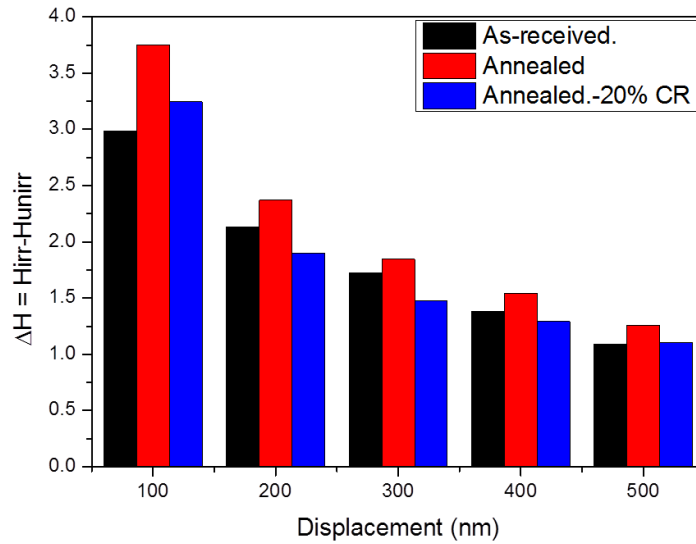


Figure 5-11 The depth profile of hardening by (a) single, (b) dual-ion irradiated up to 10 dpa at 300 °C in Al-free ODS steels

5.3.2 Irradiation effect at 470 °C to 30 dpa

5.3.2.1 Al-added ODS steel

Fig. 5-12 shows the profile of hardness after single and dual ion irradiation up to 30 dpa at 470 °C in Al-added ODS steel. In both the cases of single and dual-ion irradiation, irradiation hardening was observed, although the irradiation temperature was 470 °C at which temperature irradiation hardening was not observed in the conventional steels. This is considered to be due to trapping effect in the ODS steels where the interfaces of metal/oxide particle play a role as trapping sites for vacancies at 470 °C, consequently the mutual annihilation of dislocation loops and vacancies and/or vacancy clusters was suppressed at this temperature. The hardness after single-ion irradiation appears to be higher than that of dual-ion irradiation as shown in Fig. 5-13 which is Nix-Gao plots and Y axis is the square of hardness.

Fig. 5-14 is the depth profiles of irradiation hardening of each case (a) single and (b) dual-ion irradiation. The trend of irradiation hardening among 3 sorts of specimens is similar between (a) single and (b) dual-ion irradiation: it is largest in the annealed specimen. Namely, annealing causes enhancement of hardening irrespective of existence of helium, although irradiation hardening is smaller in dual ion irradiation than in single ion irradiation. It is again noticed that the irradiation hardening is observed in the ODS steels even after irradiation at 470 °C, that is different from the results obtained for reduced activation ferritic steels that showed no-hardening by the irradiation at 470 °C [20].

Fig. 5-15 and Fig. 5-16 show the dislocation microstructure and He bubbles, respectively, in the Al-added ODS steel after dual-ion irradiation at 470 °C to 30 dpa. The oxide particles are fine in as-received specimen, and the interfaces of metal/oxide particles are trapping sites for He bubble formation. The line-shaped dislocation in unirradiated area (deeper than 2 μm) is pre-existed dislocations, while large dislocation loops and unfold dislocations are observed in the irradiated region.

The grain boundaries also play a role as trapping sites for irradiation damage structures. In case of recrystallized specimen, the grain size is increased, and resultantly grain boundary area, that is, the number of trapping sites is reduced. A number of bubbles are observed around oxide particles. Furthermore, some of the large cavities show spherical as well as faceted shapes as shown Fig. 5-16.

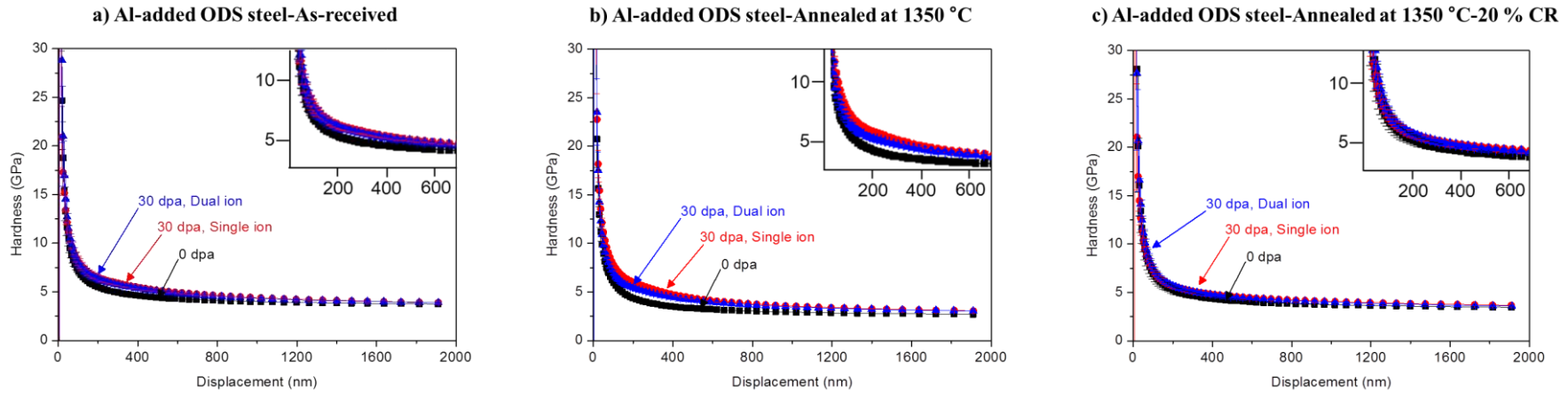


Figure 5-12 The profile of hardness after single and dual ion irradiation up to 30 dpa at 470 °C in Al-added ODS steel

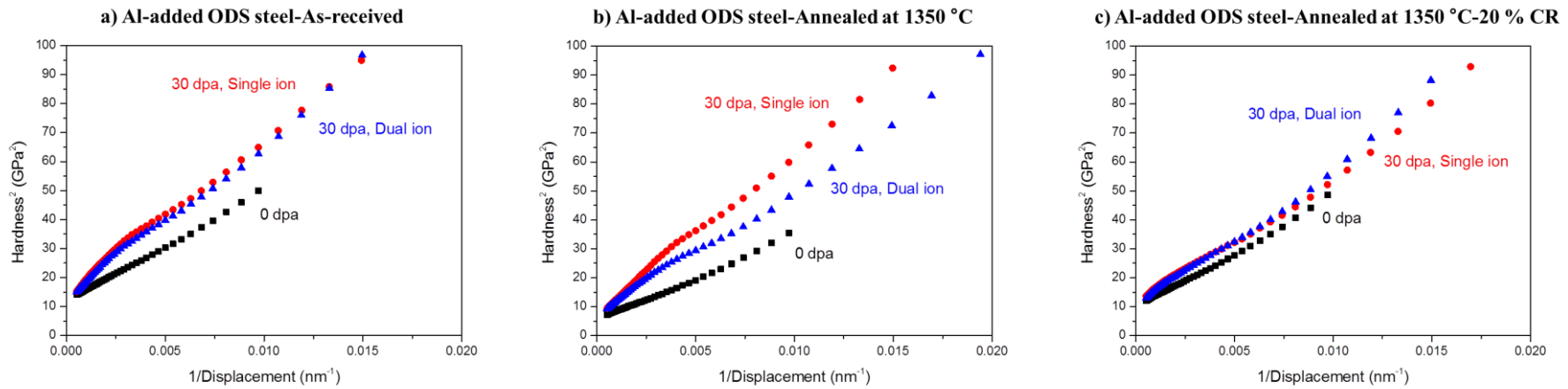
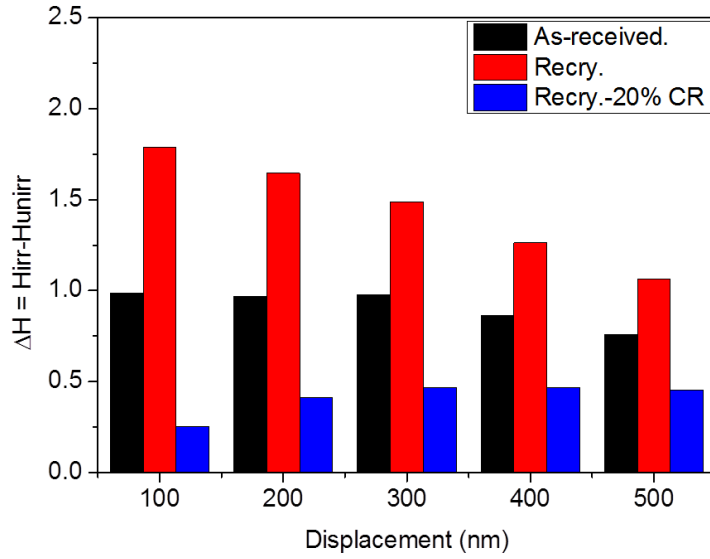


Figure 5-13 Nix-Gao plotted H^2 versus $1/h$ after single and dual ion irradiation up to 30 dpa at 470 °C in Al-added ODS steels

a) Single ion irradiation



b) Dual ion irradiation

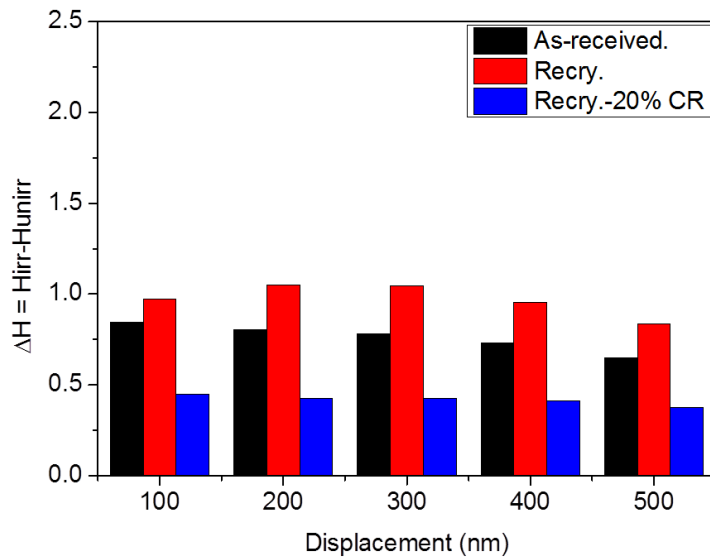


Figure 5-14 The irradiation hardening of (a) single, (b) dual-ion irradiated specimens up to 30 dpa at 470 °C in Al-added ODS steels

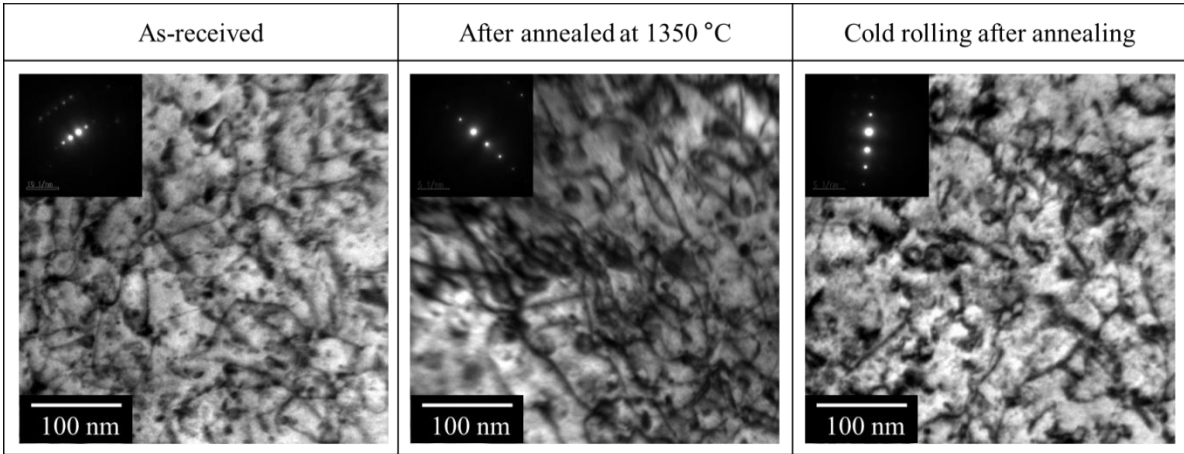


Figure 5-15 Dislocation distribution after dual-ion irradiation up to 30 dpa at 470 °C in Al-added ODS steel

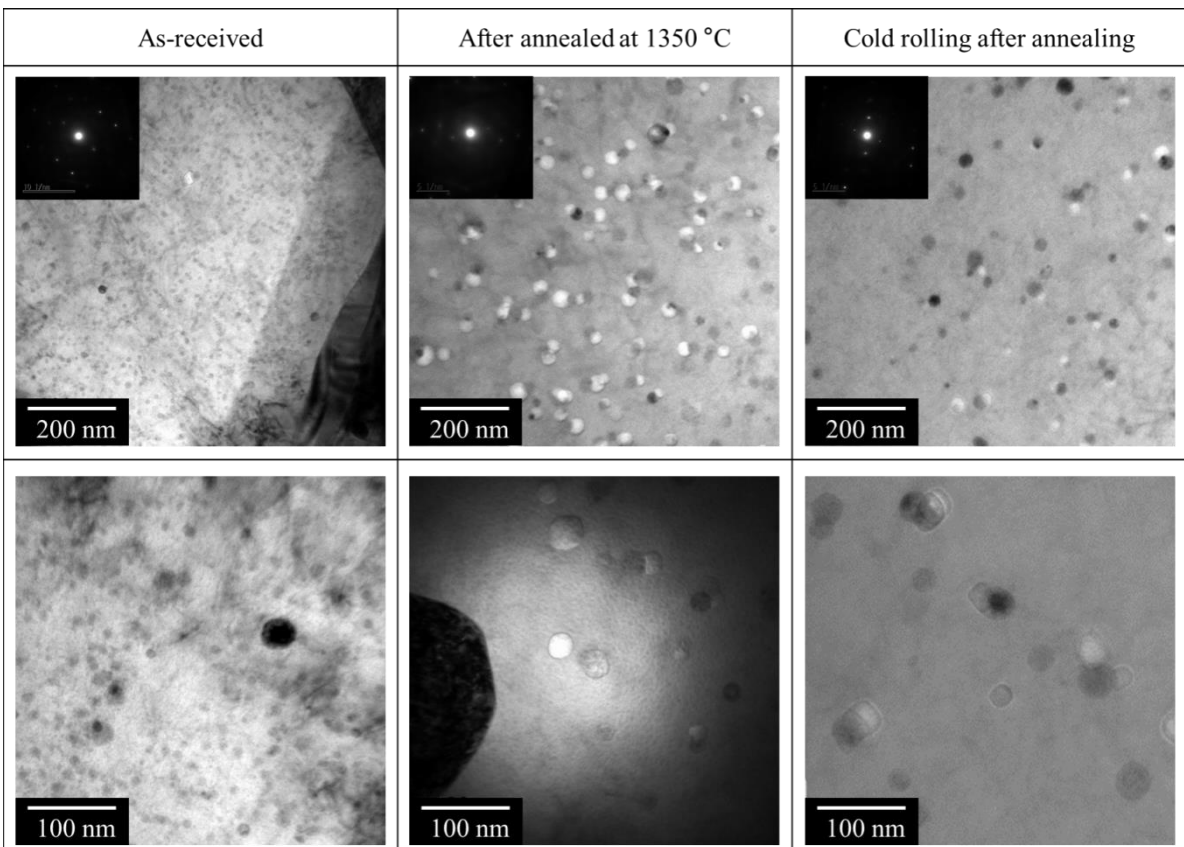


Figure 5-16 Bubbles and oxide particles after dual-ion irradiation up to 30 dpa at 470 °C in Al-added ODS steel

The reduced trapping site caused by reduction of grain boundary area and oxide particles surface area resulted in the formation of bubbles consisted of vacancies and helium atoms. The vacancy clusters are easy to be formed in the grains under the condition that grain boundaries are scarce. The oxide particles and bubbles distribution in the 20 % cold rolled specimen after recrystallization is similar with that of recrystallized specimen. The dislocations are difficult to distinguish from irradiation and from cold rolling.

Fig. 5-17 shows the depth profiles of dislocations and bubbles. Both the depth profiles of dislocations and bubbles in the irradiated region are similar to that of displacement damage.

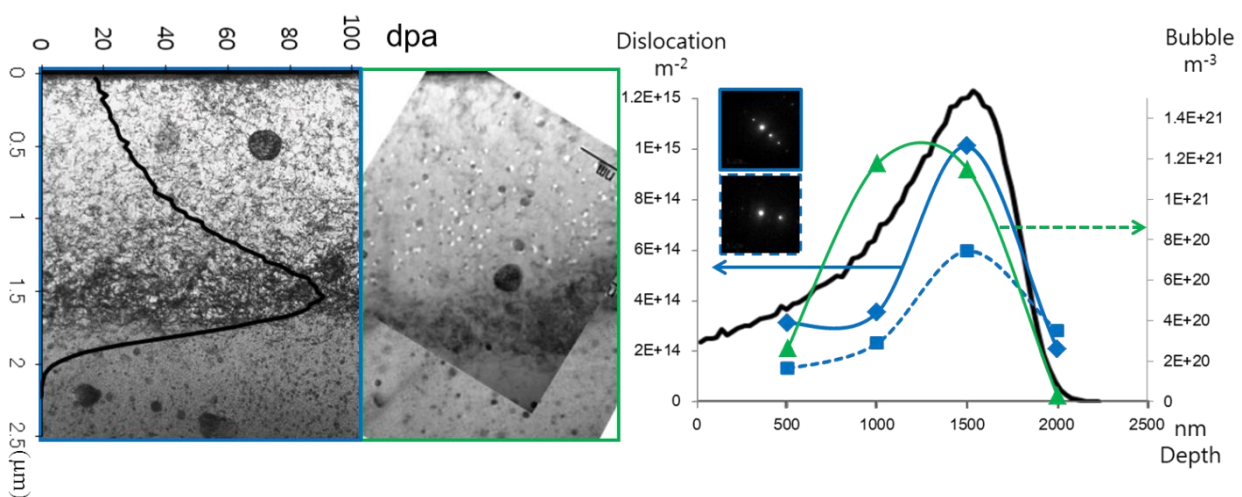


Figure 5-17 Depth profiles of dislocations and bubbles with that of displacement damage.

Fig. 5-18 (a) shows the microstructure after single-ion irradiation at 470 °C to 30 dpa in recrystallized Al-added ODS steel. The bubble was scarcely observed in the specimen. The many dislocation loops are distributed nearby surface after single-ion irradiation as shown Fig. 5-18 (b). It is clear that the bubble formation observed in the specimen irradiated with dual ions is due to the presence of helium atoms.

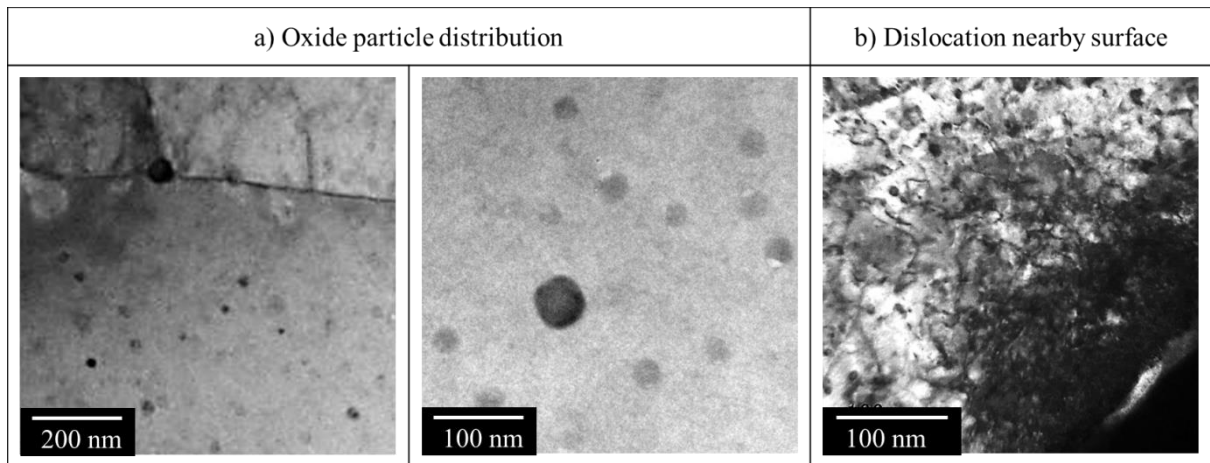


Figure 5-18 Oxide particles and dislocation distribution in recrystallized Al-added ODS steel after single-ion irradiation up to 30 dpa at 470 °C

5.3.2.2 Effect of recrystallization on irradiation hardening

Since both the grain size and the oxide particles dispersion morphology, which have a great effect on mechanical properties of ODS steels, are simultaneously changed by recrystallization, it is difficult to identify precisely the grain boundary effect. Fig. 5-19 is the hardness after irradiation and irradiation hardening at the depth of 300 nm in all the case after single and dual-ion irradiation, together with the results obtained by the analytical method following Nix-Gao model. It is clear that the annealing, that is, recrystallization causes the increase in the ion-irradiation hardening. This is interpreted in terms of the reduction of trapping sites by recrystallization which enhances grain growth and oxide particles growth that results in the reduction of grain boundary area and interface area of metal/oxide particles.

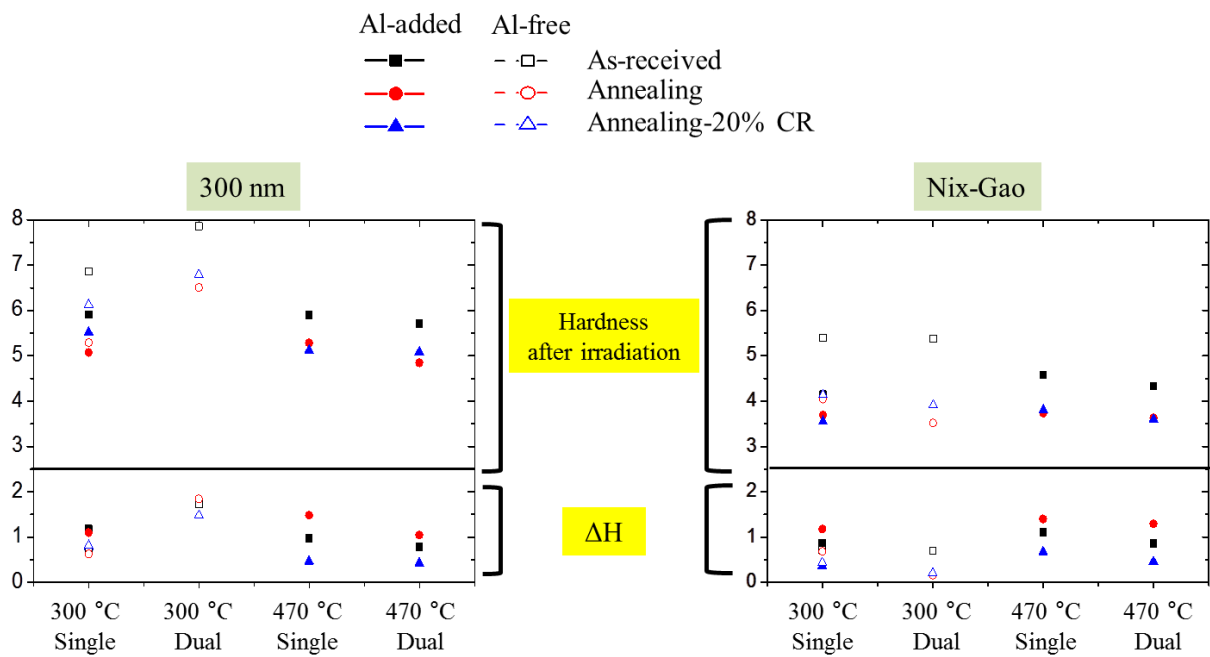


Figure 5-19 The hardness and hardening at 300 nm of indentation depth into surface and H_0 of Nix-Gao plot in different irradiation conditions

5.4 Summary

The effect of recrystallization annealing on the irradiation hardening of Al-added and Al-free ODS steels are investigated under the different irradiation conditions, such as temperature, dose and He implantation.

- 1) In Al-free ODS steel, fine grains and oxide particles are remained after annealing at 1400 °C, while in Al-added ODS steel, recrystallization occurred and oxide particles becomes larger after annealing at 1350 °C.
- 2) After the irradiation at 300 °C to 10 dpa, irradiation hardening of Al-added ODS steel is larger than that of Al-free ODS steel. The effect of annealing on the irradiation hardening is not significant. According to the Nix-Gao analysis result, the effect of cold rolling after annealing appears to reduce the irradiation hardening.
- 3) After irradiation at 470 °C to 30 dpa, irradiation hardening is observed in the ODS steel, which is a contrast to that of conventional steels showing no hardening after irradiation at temperatures above 425 °C. Recrystallization annealing causes enhancement of hardening irrespective of helium. The irradiation hardening appears to be smaller in the dual ion irradiation than in single ion irradiation.
- 4) Large voids are formed in high density after dual ion irradiation at 470 °C to 30 dpa in recrystallized Al-added ODS steel but no voids are formed in the same steel before recrystallization. It is considered that the trapping sites are reduced by coarsening of grains and oxide particles which reduces the grain boundary area and interface area of metal/oxide particles after recrystallization.

References

1. H. Kishimoto, K. Yutani, R. Kasada, A. Kimura, "Helium cavity formation research on oxide dispersed strengthening (ODS) ferritic steels utilizing dual-ion irradiation facility", *Fusion Eng. Des.*, **81** (2006) 1045-1049
2. K. Yutani, H. Kishimoto, R. Kasada, A. Kimura, "Evaluation of Helium effects on swelling behavior of oxide dispersion strengthened ferritic steels under ion irradiation", *J. Nucl. Mater.*, **367-370** (2007) 423-427
3. Peng Dou, Akihiko Kimura, Ryuta Kasada, Takanari Okuda, Masaki Inoue, Shigeharu Ukai, Somei Ohnuki, Toshiharu Fujisawa, Fujio Abe, "TEM and HRTEM study of oxide particles in an Al-alloyed high-Cr oxide dispersion strengthened steel with Zr addition", *J. Nucl. Mater.*, **444** (2014) 441-453
4. Kiyohiro Yabuuchi, Ryuta Kasada, Akihiko Kimura, "Effect of alloying elements on irradiation hardening behavior and microstructure evolution in BCC Fe", *J. Nucl. Mater.* **442** (2013) 790-795
5. Y. Takayama, R. Kasada, Y. Sakamoto, K. Yabuuchi, A. Kimura, M. Ando, D. Hamaguchi, H. Tanigawa, "Nanoindentation hardness and its extrapolation to bulk-equivalent hardness of F82H steels after single- and dual-ion beam irradiation", *J. Nucl. Mater.*, **442** (2013) 23-27
6. Akihiko Kimura, R. Sugano, Y. Matsushita, S. Ukai, "Thermal helium desorption behavior in advanced ferritic steels", *J. Phys. Chem. Solids*, **66** (2005) 504-508
7. Kiyohiro Yabuuchi, Ryuta Kasada, Akihiko Kimura, "Effect of Mn addition on one-dimensional migration of dislocation loops in body-centered cubic Fe", *Acta Mater.*, **61** (2013) 6517-6523
8. A. Kohyama, Y. Katoh, M. Ando, K. Jimbo, "A new Multiple Beams–Material Interaction Research Facility for radiation damage studies in fusion materials", *Fusion Eng. Des.*, **51-52** (2009) 789-795
9. www.srim.org
10. Ryuta Kasada, Yoshiyuki Takayama, Kiyohiro Yabuuchi, Akihiko Kimura, "A new approach to evaluate irradiation hardening of ion-irradiated ferritic alloys by nano-indentation techniques", *Fusion Eng. Des.*, **86** (2011) 2658-2661

11. Y. Takayama, R. Kasada, K. Yabuuchi, A. Kimura, D. Hamaguchi, M. Ando, H. Tanigawa, "Evaluation of Irradiation Hardening of Fe-Ion Irradiated F82H by Nano-Indentation Techniques", *Mater. Sci. For.*, **654-656** (2010) 2915-2918
12. Anthony C. Fischer-Cripps, *Nanoindentation*, Springer
13. W. C. Oliver, G. M. Pharr, "Nanoindentation An improved technique for determining hardness and elastic modulus using load and displacement sensing indentation experiments", *J. Mater. Res.*, **7** (1992) 1564-1583
14. Y. Takayama, Master's thesis, Kyoto University, 2011
15. Y. Katoh, M. Ando, A. Kohyama, "Radiation and helium effects on microstructures, nano-indentation properties and deformation behavior in ferrous alloys", *J. Nucl. Mater.*, **323**, (2003) 251-262
16. George M. Pharr, Erik G. Herbert, Yanfei Gao, "The Indentation Size Effect: A Critical Examination of Experimental Observations and Mechanistic Interpretations", *Annu. Rev. Mater. Res.*, **40** (2010) 271-292
17. WILLIAM D. NIX, HUAJIAN GAO, "INDENTATION SIZE EFFECTS IN CRYSTALLINE MATERIALS : A LAW FOR STRAIN GRADIENT PLASTICITY", *J. Mech. Phys. Solids*, **46**, (1998) 411-425
18. H. Kubo, Master's thesis, Kyoto University, 2014
19. Y. Himei, K. Yabuuchi, R. Kasada, S. Noh, H. Noto, T. Nagasaka, S. Nogami, A. Kimura, "Ion-Irradiation Hardening of Brazed Joints of Tungsten and Oxide Dispersion Strengthened (ODS) Ferritic Steel", *Mater. Trans.*, **54** (2013) 446-450
20. Akihiko Kimura, Ryuta Kasada, Akira Kohyama, Hiroyasu Tanigawa, Takanori Hirose, Kiyoyuki Shiba, Shiro Jitsukawa, Satoshi Ohtsuka, Shigeharu Ukai, M.A. Sokolov, R.L. Klueh, Takuya Yamamoto, G.R. Odette, "Recent progress in US–Japan collaborative research on ferritic steels R&D", *J. Nucl. Mater.*, **367-370** (2007) 60-67

Chapter 6

Summary and Conclusions

Oxide dispersion strengthened (ODS) steels have been developed for applications to advanced power systems, such as cladding material of GEN-IV fission reactors and first wall structural material for fusion DEMO reactors because of their high performance under severe radiation environment. The excellent performance of ODS steels stems from finely dispersed oxide particles as well as refined grains of sub-micron diameter, which are formed during hot-extrusion process that produces elongated grains and a texture. Elongated grains often cause the anisotropy in the mechanical properties, which is one of critical issues for practical fabrication process, such as tubing of this steels.

Recrystallization is a key for better formability in the fabrication of cladding tube of ODS steel, which reduces anisotropy in the mechanical properties caused by elongated grains. However, from the view of radiation tolerance, recrystallization is undesirable because it makes both oxide particles and grains be enlarged and degrades the mechanical properties.

In this research, the effect of recrystallization on ODS ferritic steel is investigated to understand the recrystallization behavior of ODS ferritic steel with focusing on the hardness and microstructural changes as well as irradiation response.

This paper consists of six chapters. In Chapter 1, the backgrounds of this research were described at the view point of nuclear energy and ODS materials science.

In Chapter 2, the recrystallization behavior of 15Cr-ODS ferritic steels with and without Al addition is investigated with focusing on the correlation between microstructure and mechanical properties in comparison to SUS430 which contains 16 wt.% Cr. The effect of recrystallization on the anisotropy and the specimen size effect on mechanical properties are also investigated for these two ODS steels

- 1) In both Al-added and Al-free ODS steels, the different recrystallization behavior is observed in comparison to conventional ferritic steel, SUS 430. Al-added ODS steel is recrystallized at above 1350 °C, while Al-free ODS steel is not fully recrystallized even at 1400 °C.
- 2) In the recrystallized Al-added ODS steel, the grains are significantly coarse and a deformation texture was formed to have Goss orientation of $\{110\}\langle 100\rangle$.
- 3) The hardness and tensile strength are reduced by recrystallization through the morphology

changes of oxide dispersion and grain shape and size to be coarser. The recrystallization behavior depends on the sort of oxide particles, for example, Al-Y-O complex oxides in Al-added ODS steel and Ti-Y-O complex oxides in Al-free ODS steel.

- 4) Anisotropy is still observed in the tensile properties at 700 °C and becomes more obvious with decreasing specimen thickness.

In Chapter 3, the effect of cold rolling on recrystallization behavior of ODS steels was investigated.

- 1) The recrystallization temperature is decreased with increasing cold rolling ratio, which is considered to be due to acceleration of microstructure change by strain induced stored energy. The Al-free ODS steel is still hard to recrystallize caused by fine oxide particles, although the effect of cold roll is evident.
- 2) The cold rolling direction also influences on grain morphology and recrystallization behavior of Al-added ODS steel, and the rolling to the perpendicular direction to extrude direction induces the rotation of the RD from $\langle 110 \rangle$ to $\langle 112 \rangle$. The recrystallization temperature is not significantly changed by cold rolling direction.
- 3) The ODS ferritic steel fabricated by hot isostatic processing has equiaxed grains, and cold rolling has no influence on the grain shape after recrystallization. It is suggested that the fabrication processing is more effective on grain morphologies than that of cold rolling processing.

In Chapter 4, the factor controlling strengthening of Al-added and Al-free ODS steels is investigated by changing microstructures through recrystallization or annealing treatment.

- 1) The hardness of ODS steel is not fitted to a single Hall-Petch plot, indicating that grain boundary strengthening mechanism is not only the factor controlling strength of ODS steels. The slope of the fitting line depends on the steel compositions. There is a significant difference in the slope of the H-P relation between Al-free and Al-added ODS steels because the addition of Al causes the changes in the oxide particles distribution morphology such as the size and number density of oxide particles.
- 2) The data deviation from the H-P line of Vickers hardness measurement tends to be reduced by

the subtraction of Orowan contribution. Since oxide particle dispersion morphology as well as grain size is changed by recrystallization treatment, it is considered that the data deviation is due to the contribution change of Orowan strengthening.

- 3) In ODS steels, the dispersion strengthening is dominant. Orowan type strengthening of Al-free ODS steel is larger than that of Al-added ODS steel, because the oxide particles are finer with higher number density in Al-free ODS steel and they are more stable at elevated temperatures. The large particles in both ODS steels play a role as obstacle to dislocation motion.
- 4) The evaluation results by several Orowan equations revealed that using the equation, $\sigma_{OR} = M\alpha\mu b\sqrt{Nd}$, the obtained value of Orowan type strengthening is most reasonable.
- 5) Finally, the Hall-Petch relationship is not unique for ODS steels, which is considered to be due to the difference in the oxide particle distribution morphology that changes the contribution to the strength of ODS steels.

In Chapter 5, the effect of recrystallization annealing on the irradiation hardening of Al-added and Al-free ODS steels under the different irradiation conditions, such as temperature, dose and He implantation.

- 1) In Al-free ODS steel, fine grains and oxide particles are remained after annealing at 1400 °C, while in Al-added ODS steel, recrystallization occurred and oxide particles becomes larger after annealing at 1350 °C.
- 2) After the irradiation at 300 °C to 10 dpa, irradiation hardening of Al-added ODS steel is larger than that of Al-free ODS steel. The effect of annealing on the irradiation hardening is not significant. According to the Nix-Gao analysis result, the effect of cold rolling after annealing appears to reduce the irradiation hardening.
- 3) After irradiation at 470 °C to 30 dpa, irradiation hardening is observed in the ODS steel, which is a contrast to that of conventional steels showing no hardening after irradiation at temperatures above 425 °C. Recrystallization annealing causes enhancement of hardening irrespective of helium. The irradiation hardening appears to be smaller in the dual ion irradiation than in single ion irradiation.
- 4) Large voids are formed in high density after dual ion irradiation at 470 °C to 30 dpa in recrystallized Al-added ODS steel but no voids are formed in the same steel

before recrystallization. It is considered that the trapping sites are reduced by coarsening of grains and oxide particles which reduces the grain boundary area and interface area of metal/oxide particles after recrystallization.

The recrystallization behavior of 15Cr ODS steels is considerably different from that of a conventional ferritic steel which recrystallizes at around 800 °C, meanwhile the ODS steels have very high recrystallization temperature (1350 °C) due to the fine dispersed oxide particles. Oxide particles play a role as obstacles to migration not only for dislocations but also grain boundaries. Recrystallization of Al-added ODS steel with mainly dispersed with rather large Al-Y-O oxide particles is easy to occur than Al-free ODS steel dispersed with very fine Ti-Y-O oxide particles. It is concluded that the matrix microstructure with ultra-fine oxide particles in Al-free ODS steel is surprisingly stable with high number density at elevated temperatures. The recrystallization or annealing effect on irradiation properties indicates that extreme reduction of trapping sites leads to the formation of tremendous amount of bubbles and dislocations compared with non-recrystallization material.

It is concluded that recrystallization treatment influences on the materials performance of ODS steel by changing microstructures, such as, oxide particles and grain morphologies as well as dislocation density. An adequate recrystallization is necessary to fabricate ODS steel tubes with controlled nano-scaled microstructures. Fine grains and ultra-fine oxide particles are necessary for radiation tolerance of material.

List of Publications

1. Yoosung Ha, Noriyuki Iwata, Akihiko Kimura, “Effect of Al on the recrystallization behavior of 15-Cr Oxide dispersion strengthened ferritic steel”, *Proceedings of the 10th International Congress on Advances in Nuclear Power Plants, ICAPP FA017* (2013)
2. Yoosung Ha, Chonghong Zhang, Akihiko Kimura, “Correlation of Microstructures with mechanical properties in recrystallized 15Cr-ODS steels”, *Pacific Rim International Congress on Advanced Materials and Processing, PRICM-8 0501* (2013)
3. Wentuo Han, Akihiko Kimura, Naoto Tsuda, Hisashi Serizawa, Dongsheng Chen, Hwanil Je, Hidetoshi Fujii, Yoosung Ha, Yoshiaki Morisada, Hiroyuki Noto, “Effects of mechanical force on grain structures of friction stir welded oxide dispersion strengthened ferritic steel”, *Journal of Nuclear Materials*, 455 **46-50** (2014)
4. Yoosung Ha, Akihiko Kimura, “The effect of cold working on recrystallization behavior of ODS steels”, *Journal of Nuclear Materials* (2014) (to be submitted)
5. Yoosung Ha, Akihiko Kimura, “Effect of recrystallization on irradiation hardening of 15Cr-ODS steels”, *Journal of Nuclear Materials* (2014) (to be submitted)
6. Yoosung Ha, Akihiko Kimura, “Effect of recrystallization on the ion-irradiation hardening and microstructural changes in 15Cr-ODS ferritic steel”, *Nuclear Instruments and Methods B: Beam Interactions with Materials and Atoms* (2014) (to be submitted)

List of Presentations (International conference and symposium)

1. Yoosung Ha, Akihiko Kimura, "Effect of heat treatment condition on recrystallization of ODS steels", The 4th G-COE International Symposium in collaboration with JGSEE - "ZERO-CARBON ENERGY 2012, Bangkok, Thailand, 2012.05.23-23.
2. Yoosung Ha, Akihiko Kimura, "The effect of cold working on recrystallization behavior of ODS steels", The 27th Symposium on Fusion Technology (SOFT 2012), Liege, Belgium, 2012.09.25.
3. Yoosung Ha, Noriyuki Iwata, Akihiko Kimura, "Effect of Al on the recrystallization behavior of 15Cr-oxide dispersion strengthened ferritic steel", 2013 International Congress on Advances in Nuclear Power Plants (ICAPP2013), Jeju, Korea, 2013. 04.15.
4. Yoosung Ha, Akihiko Kimura, "Recrystallization behavior of cold-rolled ODS ferritic steels", 2nd Japanese-German Workshop on Energy Materials Science, Karlsruhe, Germany 2012.12.13.
5. Yoosung Ha, Chonghong Zhang, Akihiko Kimura, "Correlation of microstructures with mechanical properties in recrystallized 15Cr-ODS steels", 8th Pacific Rim International Congress on Advanced Materials and Processing (PRICM-8), Hawaii, USA, 20130806.
6. Yoosung Ha, Sanghoon Noh, Akihiko Kimura, "Effect of recrystallization behavior with cold rolling on hardness in oxide dispersion strengthened ferritic steels", 16th International Conference on Fusion Reactor Materials (ICFRM-16), Beijing, China, 2013.10.22.
7. Yoosung Ha, Akihiko Kimura, "Effect of cold rolling process on recrystallization behavior in ODS ferritic steels", Kyoto-Ajou Joint symposium on Energy science, Uji, Kyoto, 2014.02.25.
8. Yoosung Ha, Hiroshi Kubo, Akihiko Kimura, "Effect of recrystallization on irradiation hardening of 15Cr-ODS steels", 3rd Japanese-German Workshop on Energy Materials Science, Uji, Kyoto, 2014.03.17.
9. Yoosung Ha, Akihiko Kimura, "Effect of recrystallization on the ion-irradiation hardening and microstructural changes in 15Cr-ODS ferritic steel", The 19th International Conference on Ion Beam Modification of Materials (IBMM 2014), Leuven, Belgium, 2014.09. 18.

Acknowledgement

Above all, I would like to declare my great appreciation to Professor Kimura for the support of my research, invaluable advice and guidance as well as the enjoyable atmosphere at the institute he served. His patience, passion and the spirit of inquiry encouraged me to go forward bravely with confidence.

I also greatly appreciate to Professor Hoshide and Professor Imatani for their support and helpful comments.

I am deeply grateful to Professor Konishi and Professor Kasada for suggestions and advice.

I would like to thank to Professor Moon Chang-gwon, who is my advisor in Korea.

Special thanks to:

-Members in Kimura Laboratory:

Ms. Wada (I thank you for your kindness), Dr. Noh, Dr. Kim (B. J.), Professor Yabuuchi, , Dr. Je, Dr. Han, Dr. Yamamoto, Mr. Chen, Mr. Zhang, Ms. Eva, Mr. Sugino, Mr. Tsuda, Mr. Maekawa, Mr. Kubo, Mr. Taniguchi, Mr. Murai, Mr. Yamaguchi, Mr. Okunishi, Mr. Nakasuji, Mr. Takayama, Mr. Kawakita, Mr. Kobayashi.

-Researchers in IAE:

Professor Iwata, Professor Kondo, Mr. Hashitomi, Mr. Hayashi, Ms. Kitamura, Ms. Hasegawa, Ms. Sakamoto.

-Researchers in Kyoto University:

Dr. Lee (Y. J), Dr. Park (C.H), Dr. Park (S.W.), Dr. Seo, Dr. Kwon, Dr. Gwon, Mr. Kim (S. H.), Dr. Lee (M. H.).

Finally, I want to thank my family, Ha Seung-wan, Jeong Mu-sun, Ha Yoo-jin and Ha Yang-won. I have to say I love you.

It is beyond all description how thankful I am that I have experienced so much help, advice and support during my doctoral work at Kyoto University. I appreciate to everyone once again.

2014.09. Ha Yoosung